Department of Physics and Astronomy

Evaluation of Recurrent Glioma and Alzheimer's Disease Using Novel Multimodal Brain Image Processing and Analysis

Christopher Leatherday

This thesis is presented for the Degree of
Doctor of Philosophy
of
Curtin University

March 2016

To the best of my knowledge and belief this thesis contains no material previously published by any other person except where due acknowledgement has been made. This thesis contains no material which has been accepted for the award of any other degree or diploma in any university.

Signed _____ on _11_ / _03_ / _2016_

Christopher Leatherday

Abstract

Several techniques utilizing multimodal brain image processing and analysis as a potential means of improving diagnostic outcomes in recurrent glioma and Alzheimer's disease (AD) have been investigated.

Treatment for late stage glioma involves surgery and chemo-radiotherapy which causes necrosis and oedema that can be mistaken for, or mask, cancer recurrence. Two positron emission tomography (PET) imaging isotopes (^{11}Carbon-Methionine (CMET) and 3'-deoxy-3'-^{18}Fluorine-fluorothymidine (FLT)) were investigated with regards to the ideal length of time that should elapse between isotope administration and imaging in a cohort of post-treatment late stage glioma patients in order to maximise tumour-healthy tissue contrast. It was found that the ideal times to commence post-administration imaging using CMET and FLT were less than 40 and 75 minutes respectively. The same patient cohort was then used to test the capacity of CMET and FLT-PET as well as Gadolinium enhanced T1 weighted magnetic resonance imaging (Gd-MRI) to act as a survival predictor, based on the volume of tissue that demonstrated substantially elevated uptake/enhancement. CMET was the only significant predictor of survival ($p<0.05$, Log-Rank test).

Inter-subject variability and the nonlinear fashion in which AD symptoms develop make definitive early diagnosis very difficult. In vivo brain image analysis could increase diagnostic accuracy by identifying characteristic patterns of AD physiology. A study was conducted to compare an optimised automated volumetric hippocampal mask with one that was manually defined and assessed their utility in separating groups of healthy control (HC), mildly cognitively impaired (MCI), and AD brains based on hippocampal metabolism as seen on 2-Deoxy-2-[^{18}F]fluoroglucose (FDG)-PET. Both masks were able to find significant differences between the AD and MCI ($p < 0.005$) and AD and HC ($p < 0.0005$) groups, but not the MCI and HC groups using Tukey's HSD test. The automated mask was then evaluated with regards to its potential utility as a clinical diagnostic tool; it was found that it would likely find greatest value as a means of screening patients in order to flag those with very low hippocampal metabolism as having an increased risk of AD.

Acknowledgments

List of Figures

List of Tables

List of Frequently used Abbreviations

AD – Alzheimer's Disease

ADNI – Alzheimer's Disease Neuroimaging Initiative

AIBL – Australian Imaging Biomarkers and Lifestyle study

AUC – Area Under the Curve

BBB – Blood Brain Barrier

CDR – Clinical Dementia Rating

CMET – ^{11}Carbon-Methionine

CNS – Central Nervous System

CSF – Cerebrospinal Fluid

FDG – Deoxy-2-[^{18}F]Fluoroglucose

FLT – 3'-Deoxy-3'-^{18}Fluorine-Fluorothymidine

Gd-MRI – Gadolinium enhanced Magnetic Resonance Image

GDS – Global Deterioration Scale

HC – Healthy Control

MCI – Mild Cognitive Impairment

MMSE – Mini Mental State Examination

MNI – Montreal Neurological Institute

MRglc – Glucose Metabolic Rate

MRI – Magnetic Resonance Imaging

PET – Positron Emission Tomography

ROC – Receiver Operating Characteristic

SUV – Standardised Uptake Value

VBA – Voxel Based Analysis

Conference Presentations Arising from this Thesis

'Detecting Alzheimer's Disease Using Automated Volumetric Hippocampal Masking', C. Leatherday, A. Campbell (poster) (*EPSM 2013, Nov 3-7, Perth WA)*

'Uptake of ^{11}C-Methionine on Glioma at Various Post-Injection Time Points', C. Leatherday, A. Campbell, R. Francis (*CSM 2014, Sep 4-7, Melbourne VIC)*

'Predicting Survival Outcomes of Post-Treatment Glioma Patients by Quantification of Viable Tumour Volume on CMET/FLT PET and MRI', C. Leatherday, A. Campbell, R. Francis (*IUPESM 2015*, *Jun 7-12, Toronto ON)*

1   Introduction and Literature Review

1.1   Overview

Disease pathology of the brain was historically difficult to observe in vivo, due to the requirement to penetrate the skull in order to expose the brain, and the extremely high stakes involved in any attempt at physical intervention in the cranial region. The advent of x-ray, magnetic resonance imaging (MRI), and various nuclear medicine imaging methods have completely changed the manner in which diseases of the brain can be observed and treated. This thesis presents image analysis techniques to aid in the identification and treatment of two brain conditions: glioma and Alzheimer's disease (AD).

Glioma, and in particular glioblastoma multiforme, is a tumour type that is notorious for its low rates of long term treatment efficacy. Treatment is almost always followed by recurrence due to the aggressive radial growth patterns of the disease and the difficulty associated with complete lesion removal (Fortin 2011). Novel brain imaging methodologies and image processing techniques are avenues of research that aim to increase spatial accuracy of lesion identification and deliver higher sensitivity and specificity with respect to the detection of recurrent cancer growth. In this thesis, the optimal post-injection delay time for imaging of post-treatment glioma patients is investigated for two positron emission tomography (PET) tracers: ^{11}Carbon-Methionine (CMET), and 3'-deoxy-3'-^{18}Fluorine-fluorothymidine (FLT). These two PET tracers, as well as gadolinium enhanced T1 weighted MRI (Gd-MRI) were then assessed for their utility in survival prediction based on the volume of brain tissue demonstrating elevated uptake/enhancement in each modality. This research has two main aims with regards to brain imaging in glioma: to identify an ideal post-injection waiting period for glioma PET imaging with CMET, and with FLT (addressed in Chapter 2); and to quantify the degree to which CMET, FLT, and Gd-MRI can be used to predict survival in a cohort of post-treatment glioma patients (addressed in Chapter 3).

The prevalence of AD, and the costs associated with it, has risen inextricably with life expectancy in the Western world. The medial temporal lobe of the cerebrum is a brain region that shows significant early physical atrophy in AD (Jack et al. 1997). Atrophy of the hippocampus in particular is known to be an early indicator of AD (Morra et al. 2009). Such severe atrophy can result in a decrease in localised glucose metabolic rate (MRglc). The small size of the atrophied hippocampus can result in the quantification of a reduction in MRglc to be hampered by partial volume effects. Attempts to observe the expected reduction in MRglc in the hippocampus using functional brain imaging have often failed in studies that have used voxel based analysis (VBA) methods of image spatial normalisation to register images to a standard space; this was likely due to registration errors causing inconsistencies in hippocampal location between subjects (Mosconi et al. 2005). An optimised volumetric mask based on manually outlined subject hippocampal regions has shown utility in detecting reductions in localised MRglc in AD and mildly cognitively impaired (MCI) brains (Mosconi et al. 2005). In this thesis, a manually outlined mask is compared with one that was based on automatically defined hippocampal volumes by the program *FSL* (Smith et al. 2004) with regards to their utility in reduced hippocampal MRglc detection in groups of mildly cognitively impaired (MCI) and AD brains. The *FSL* subject hippocampal volume based mask was then further tested for its potential utility in the diagnosis of an individual, both when a subject MRI is present to guide spatial normalisation, and when it is absent. The aims of this research in AD brain image analysis are: to quantify the efficacy of two different hippocampal masking techniques in detecting group level differences in MRglc between cohorts of Healthy Control (HC), MCI, and AD brains using deoxy-2-[^{18}F]fluoroglucose (FDG)-PET (addressed in Chapter 4); and to assess the potential clinical utility of an automated hippocampal masking algorithm in MCI and AD diagnosis (addressed in Chapter 5).

This chapter introduces important background concepts for the thesis, and reviews relevant literature in the field.

1.2 Brain Anatomy and Function

The average adult human brain weighs approximately 1400 grams and has a volume of 1200 cm^3 (Carpenter and Sutin 1983). It has approximate symmetry along the central sagittal plane, and as such can be divided into left and right hemispheres. The total brain volume can be divided into three regions: the brainstem, the cerebellum, and the cerebrum. These three regions are shown in Figure 1.
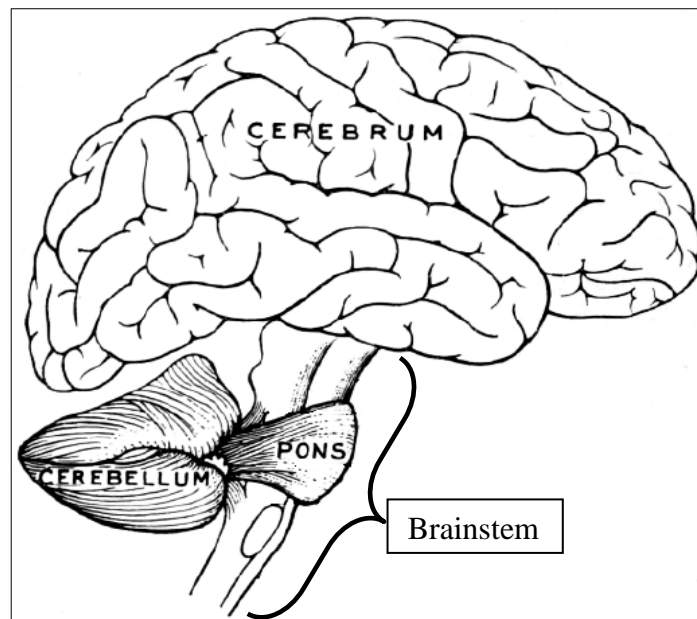
Figure 1, The cerebellum, cerebrum and brainstem (Gray and Lewis 1918, p 766)

The bone structure of the skull, as well as three distinct membranes between the brain and the skull, protect the brain from impact trauma. The extremely tough, outermost membrane is the dura mater. Inside this is the intermediate membrane, the arachnoid. The innermost membrane is the pia mater, which is extremely delicate and adheres very closely to the brain's surface. The brain is suspended in a colourless liquid called cerebrospinal fluid (CSF), situated inside the arachnoid membrane. CSF also flows down through the spinal column, and acts as an impact-dampening mechanism for the brain. CSF forms an important component of the system of barriers that allow for "… maintenance of the cerebral environment and protection of the brain from the systemic circulation" (Deisenhammer et al. 2015, p 18).

1.2.1 Vascularisation, the Blood-Brain Barrier, and Energy Metabolism

1.2.1.1 Vascularisation

The human brain receives an extremely large proportion of cardiac and metabolic output relative to its size. Roughly 15% of blood flow is directed to the brain, and around 20% of the body's resting metabolic rate is required to maintain brain function (Siegel and Agranoff 1999). Despite the fact that normal brain tissue accounts for about 2% of the body's mass, it has the highest rate of glucose metabolism of any healthy tissue in the body (Gulyas and Halldin 2012). Blood is delivered to the cerebrum via the internal carotid arteries, and to the cerebellum and brain stem via the vertebral arteries, both of which are bilateral (Cipolla 2009), Figure 2 shows the location of these arteries on the right hand side of the neck.
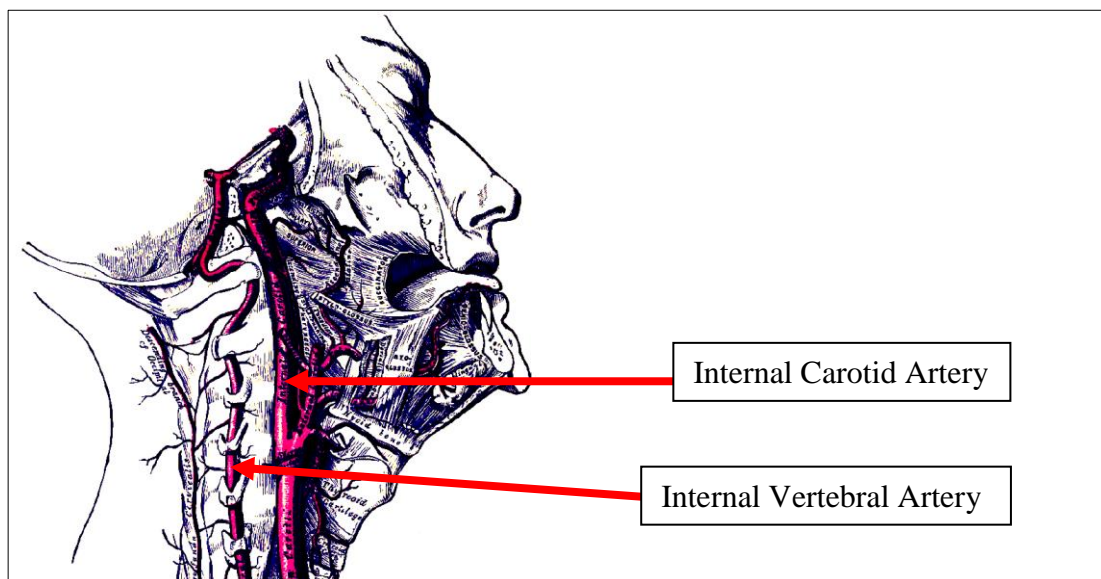
Figure 2, The locations of the right Internal Carotid and Vertebral Arteries (Gray and Lewis 1918, p 567).

1.2.1.2 The Blood-Brain Barrier

The blood-brain barrier (BBB) is a term that describes the biological system controlling the flow of material between the brain and the rest of the body. This barrier is vital for optimal cerebral performance, as it allows the brain to maintain the

correct concentration of ions needed for proper function, and protects it from blood-borne pathogens (Saunders et al. 2008). The BBB is "… a fundamental physical barrier at the level of intercellular junctions between cells" (Saunders et al. 2008, p 279), and is present across a large number of blood vessels in contact with the brain. Part of the overall BBB system is the blood-cerebrospinal fluid barrier (BCSFB), located in the choroid plexus, found in each of the brain's ventricles. Figure 3 depicts the location of blood vessels on the inferior surface on the brain, displaying the extent of vascularisation that is present. Figure 4 is an illustration of the location of the ventricles of the brain.
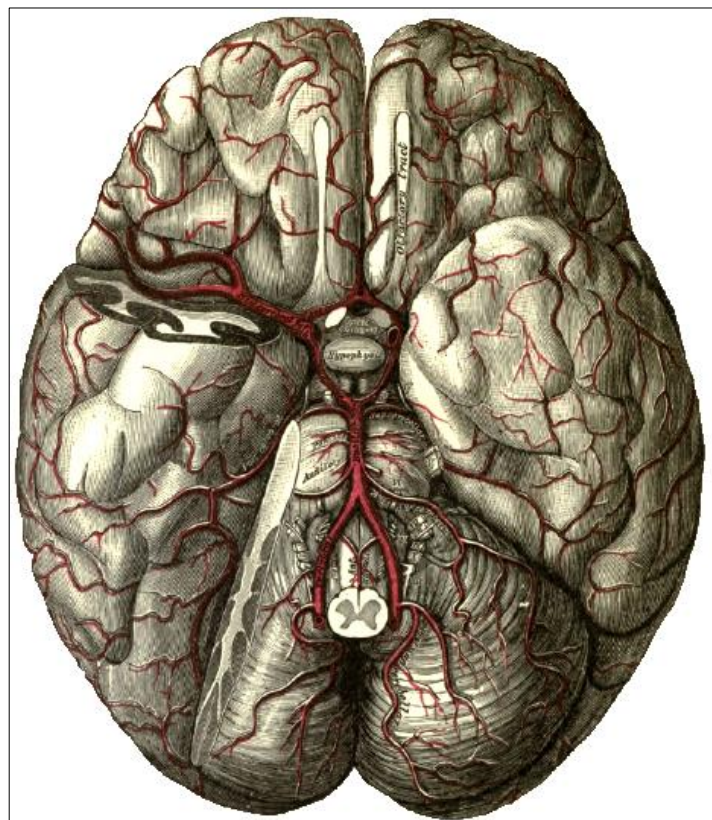
Figure 3, The network of blood vessels on the inferior brain surface (Gray and Lewis 1918, p 572).
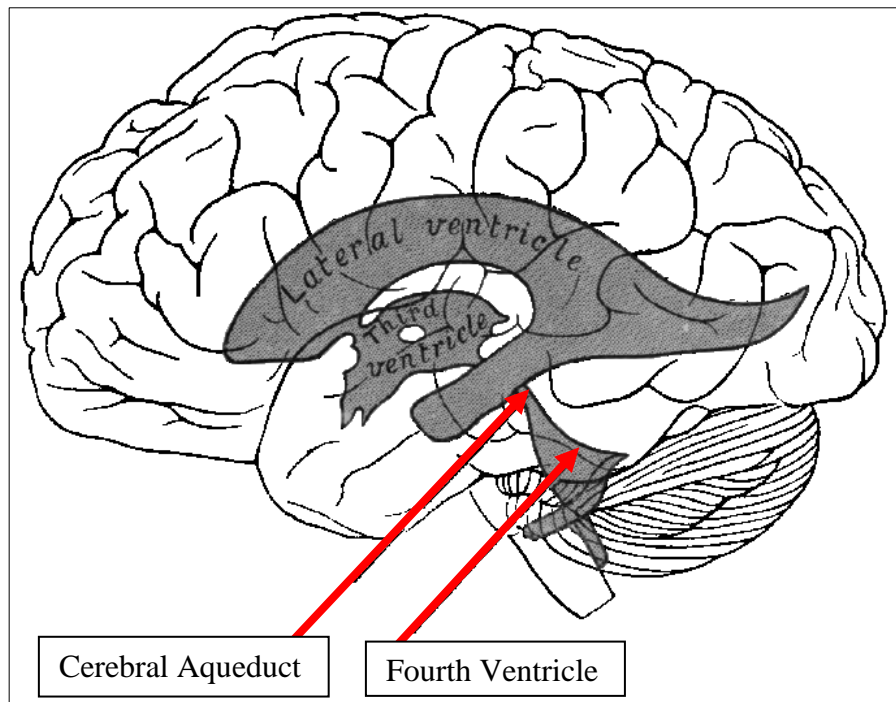
Figure 4, The location of the ventricles of the brain (Gray and Lewis 1918, p 829).

Figure 5 shows the location of the choroid plexus in a lateral ventricle. The choroid plexus "… regulates the exchange of fluid and solutes between blood and CSF in part by acting as a passive, paracellular barrier to solutes" (Zheng and Chodobski 2005, p 26). As well as forming a vital component of the overall BBB, the choroid plexus continually produces 'fresh' CSF, controls the flow of CSF between the ventricles and pia mater-arachnoid cavity, and fulfils a similar role within the brain as the kidneys do for the overall blood stream, that is, the filtration and removal of waste products and metabolites.
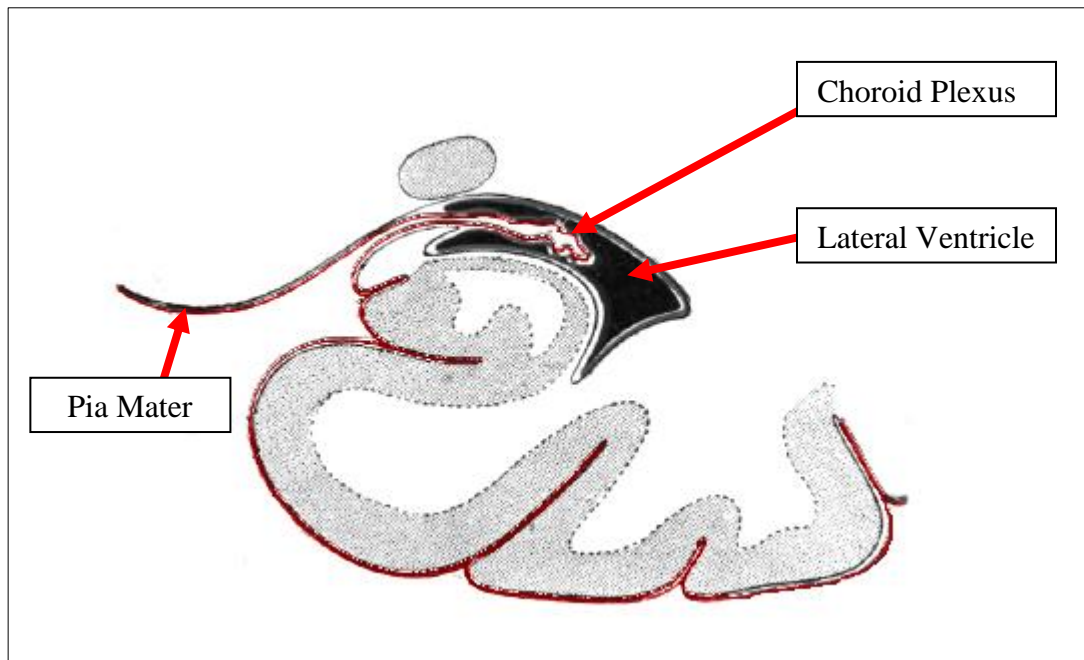
Figure 5, A coronal cross-section of the inferior horn of the lateral ventricle (Gray and Lewis 1918, p 841).

The BBB is highly effective at allowing the brain to operate in a healthy manner, but can prove a significant obstacle in drug delivery and imaging. In-vivo imaging agents are often limited to molecules that can freely traverse the BBB. However, pathology that includes disruption of the BBB can be highlighted by use of an imaging agent that is only able to enter the brain in specific regions of disruption. Clinically, disruption of the BBB can be shown using Gd-MRI, as the gadolinium will pool in, and therefore highlight, areas of BBB disruption.

1.2.1.3 Energy Metabolism

The majority of cellular work within the body is powered by Adenosine Triphosphate (ATP), which is produced by the oxidation of glucose during cellular respiration. Some cells, such as those found in muscle, are capable of storing significant amounts of glycogen (enough to power them for up to a day without replenishment from food). Glycogen can then be converted to glucose via hydrolysis. These cells can also store oxygen through the usage of myoglobin (Campbell and Reece 2002). The brain stores some glycogen, but in very low concentrations compared to the aforementioned tissues, and does not have intracellular oxygen storage capacity. The brain therefore requires a constant supply of both glucose and

oxygen for survival, which is delivered through the vascular system. Oxygen is able to diffuse across cell membranes and so is able to freely traverse the BBB in accordance with the concentration gradient. Specific transporters exist within the endothelial cells of the BBB for the uptake of glucose, so that it may be absorbed from the brain's arterial blood supply through facilitated diffusion (Siegel and Agranoff 1999).

Since glucose is absorbed from the blood as required, the total cerebral uptake of glucose is proportional to the amount of neuronal activity taking place in the brain at a given moment in time. This principle is also applicable to smaller volumes within the brain itself; that is, the localised instantaneous rate of glucose uptake and/or blood perfusion in a given volume is proportional to the amount of neuronal activity within that volume. Therefore, imaging the rate of glucose metabolism within the brain serves as a surrogate means to visualise neuronal activity.

1.2.2   The Cerebrum

The outermost layer of the cerebrum is called the cerebral cortex, and is divided anatomically into four lobes: frontal, parietal, temporal and occipital. The lobes of the cerebral cortex are shown in Figure 6.
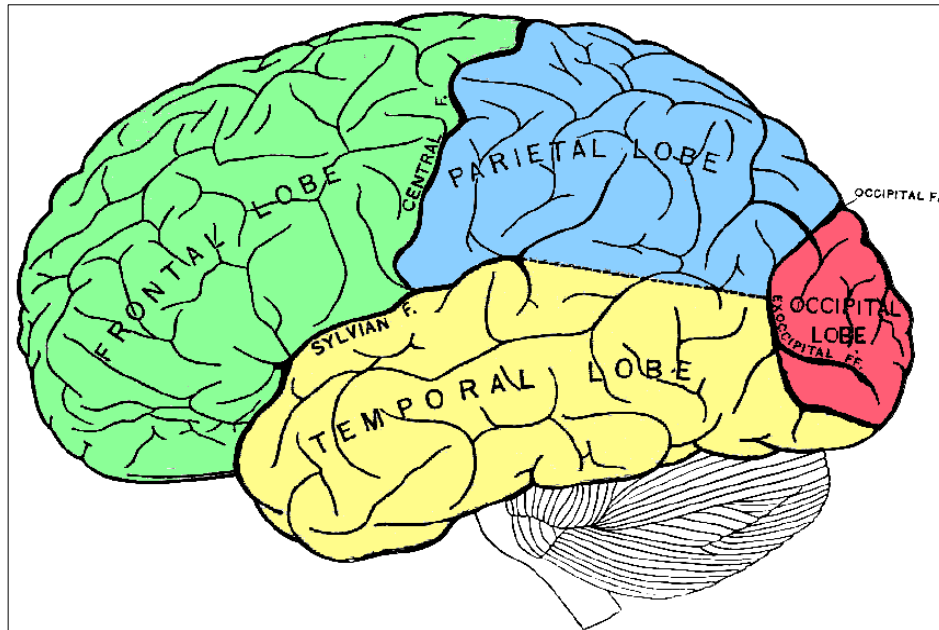
Figure 6, The four lobes of the cerebral cortex (Gray and Lewis 1918, p 821).

Different regions of the cerebral cortex perform different neurological functions. As the brain develops during childhood, the hemispheres specialise in a distinct manner. The left hemisphere specialises towards "… language, math, logic operations, and the processing of serial sequences of information" (Campbell and Reece 2002, p 1049), whereas the right hemisphere is "… stronger at pattern recognition, face recognition, spatial relations, nonverbal ideation, emotional processing in general, and parallel processing of many kinds of information" (Campbell and Reece 2002, p 1049). As can be seen in the coronal slice depicted in Figure 7, the cerebral cortex is arranged in a pattern of ridges (gyri) and furrows (sulci). Major gyri and sulci form the borders of the lobes of the cerebrum. Many of the major gyri and sulci and some of the functional areas of the cerebrum are highlighted in Figure 8.
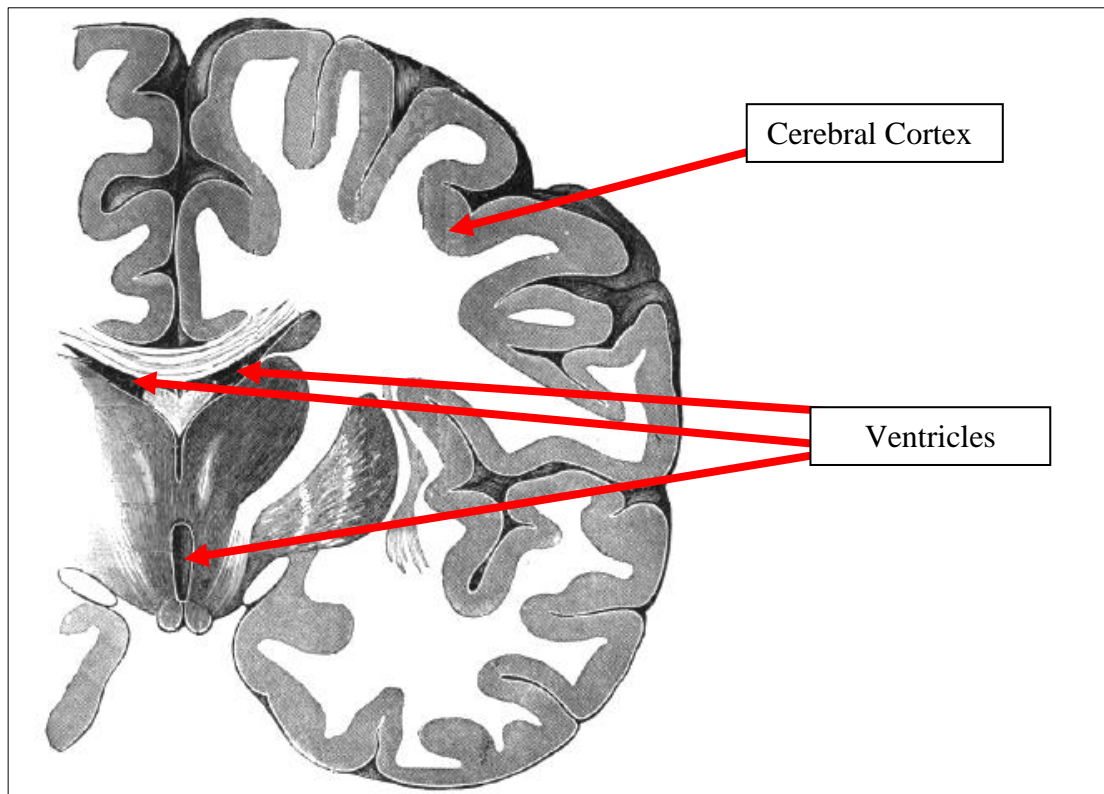
Figure 7, A coronal slice through the cerebrum showing the location and folds of the cerebral cortex (Gray and Lewis 1918, p 810).
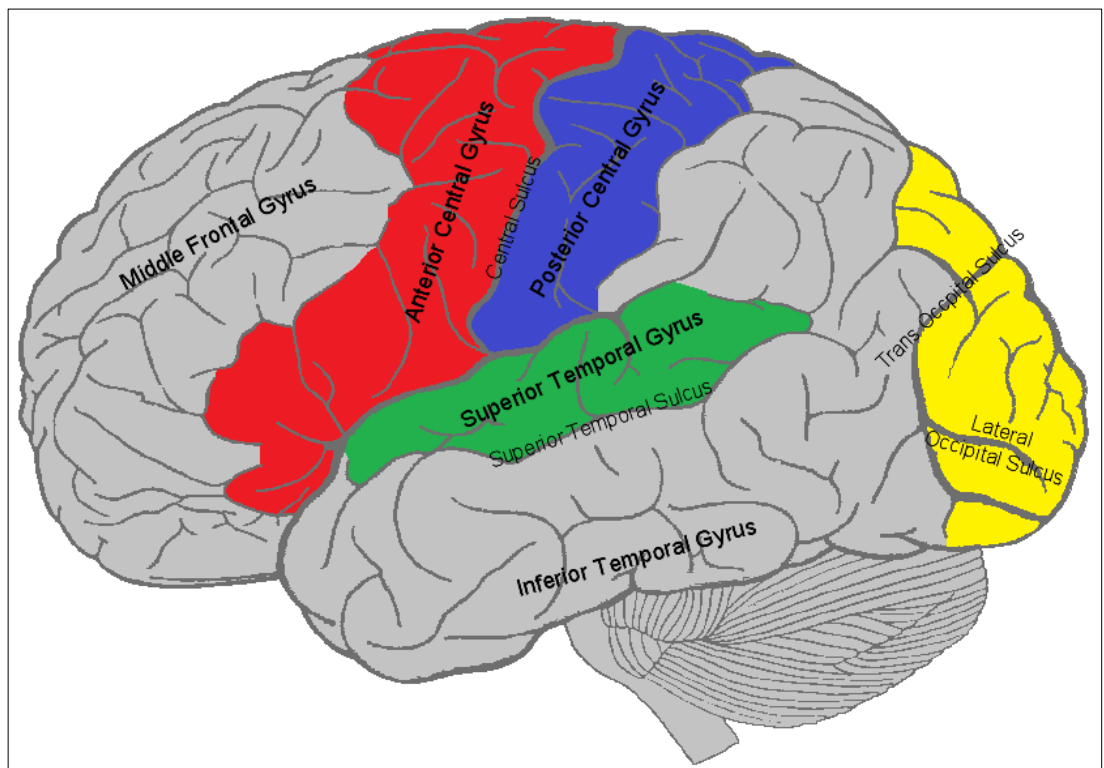
Figure 8, Some of the major gyri and sulci, and functional areas on the lateral surface of the cerebrum. Red denotes the motor areas, general sensation areas in blue, auditory areas in green and visual areas in yellow. Modified from Gray and Lewis (1918), p 821.

Located inside the cerebrum is the sub-cortex, which contains multitudinal individual subcortical structures. Some of these are highlighted in Figure 9.
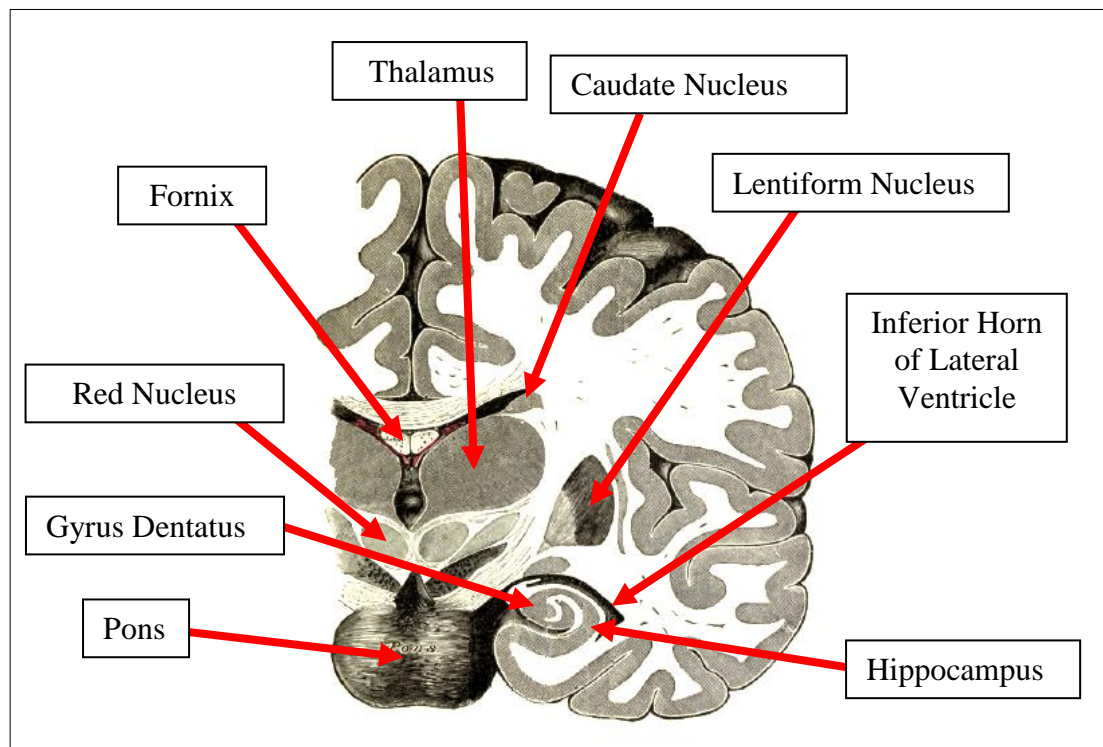
Figure 9, A coronal slice of the cerebrum showing several subcortical structures (Gray and Lewis 1918, p 809).

Of particular importance to AD is the hippocampus, a bilateral structure situated within the temporal lobe of each hemisphere. The inferior horn of the lateral ventricle lies around the edge of the hippocampus, and is bordered by the lateral ventricle on the superior and lateral sides (refer Figure 10). At the medial edge of the hippocampus is the dentate gyrus, and the inferior borders the subiculum and parahippocampal gyrus (Gardner et al. 1975). The location of the hippocampus from a sagittal viewpoint is shown in Figure 11.
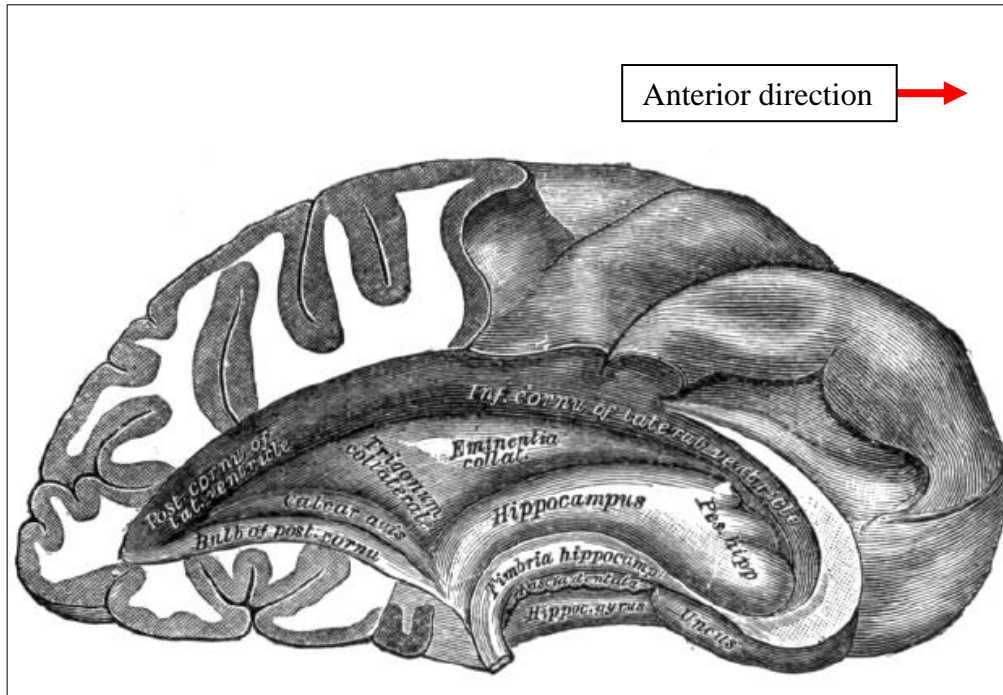
Figure 10, An axial cutaway through the cerebrum showing the location of the hippocampus and pes hippocampus (Gray and Lewis 1918, p 833).
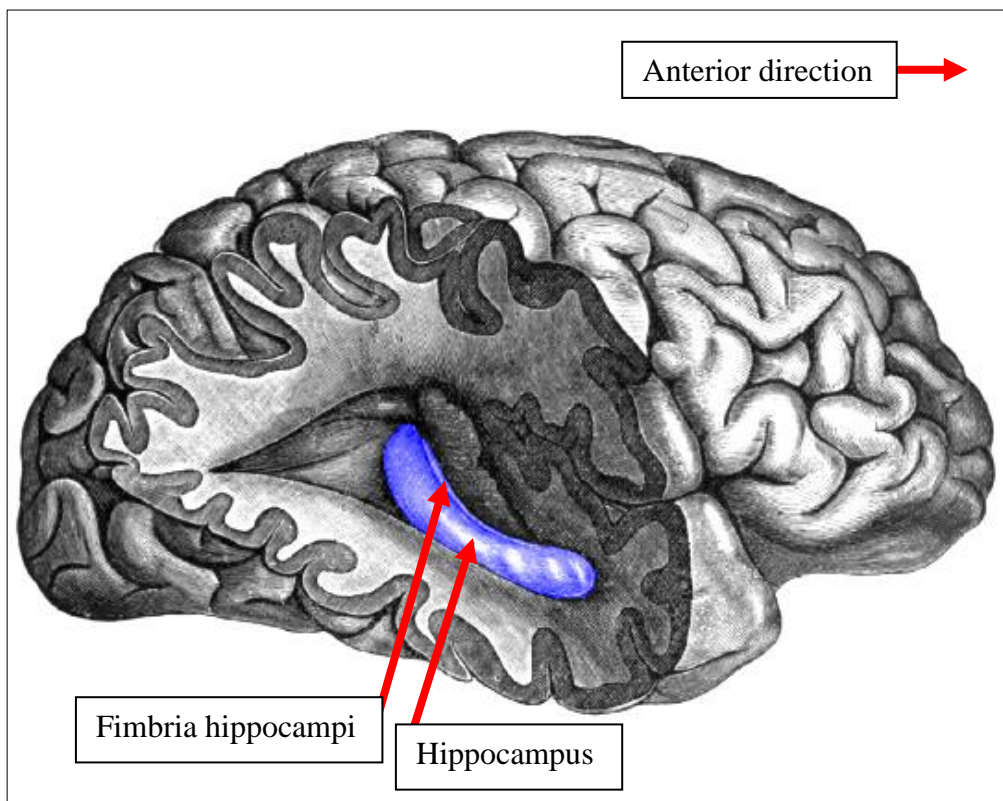
Figure 11, A cutaway sagittal view showing the location of the hippocampus (Gray and Lewis 1918, p 832).

1.2.3 The Cerebellum and the Brainstem

The cerebellum lies inferior to the occipital and posterior portion of the temporal lobes of the cerebrum. The cerebellum is not as 'advanced' in an evolutionary sense as the cerebrum, and does not play a role in sensory perception or the formation of thoughts or memories. Its functions include the coordination of muscle movement and balance, which is achieves with the aid of collateral input from the sensory system (Waxman 2013).

Attaching the brain to the spinal cord is the brainstem. It lies inferior to the cerebrum and to the anterior of the cerebellum. Including such structures as the pons and medulla, the brainstem is responsible for the regulation of several essential automated functions, such as breathing, heartbeat, and blood pressure (Waxman 2013). The pons can be of particular interest in AD research. One of the symptoms of AD is a reduced metabolic rate across several key areas of the cerebrum (McKhann et al. (2011); Minoshima et al. (1997)). The pons, however, has been shown to maintain pre-AD levels of glucose metabolism throughout the duration of the disease (Minoshima et al. 1995). Consequently, the localised metabolic rate seen in parts of the cerebrum of AD patients can be normalised to the metabolic rate in the pons in order to provide an estimate of degree of localised cerebral metabolic degradation. The brainstem and cerebellum can be seen in sagittal view in Figure 12.
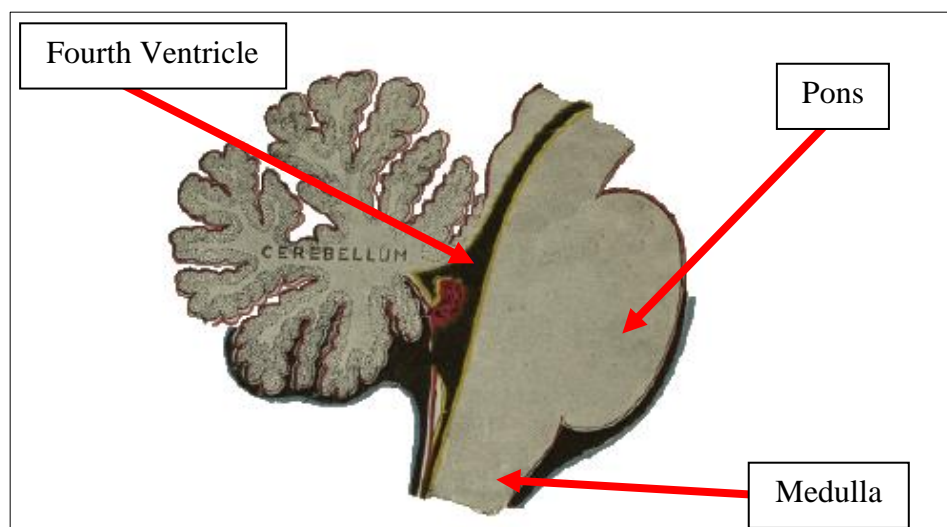
Figure 12, The brainstem and the cerebellum, shown in sagittal view (Gray and Lewis 1918, p 798).

1.3   Glioma

Glioma is the term given to a range of tumours of the central nervous system (CNS) that originate from glial cells. Gliomas are the most common tumour of the brain and are responsible for 49% of all primary brain tumours and approximately 2% of new cancer cases in the USA; life expectancy following a glioma diagnosis is poor, most patients die within 12 months (Hayat 2011). The treatment method of surgical debulking, followed by chemoradiotherapy, can increase median life expectancy to over a year, and the two year survival rate from 10% to 26% (Stupp et al. 2005).

1.3.1   Symptoms and Diagnosis

Symptoms of glioma can vary depending on their location in the CNS, type and severity. Symptoms can include nausea and/or vomiting, headaches, trouble balancing or asymmetrical physical weakness, memory and speech difficulty, fainting, seizures, incontinence, back and neck pain, as well as depression, irritability and other personality changes. Mental symptoms of glioma can also affect the patients' decision-making ability and judgement process, and cause further delays in the formation of a proper diagnosis due to sufferers' lack of willingness to see a physician. Symptoms may develop slowly and are often ignored or mistaken for other ailments (Salander et al. 1999).

Once symptoms have been assessed and glioma is considered a possibility, a preliminary diagnosis can be made using radiologic imaging. Gd-MRI is effective in showing increased intensity in a tumour region, provided there is disruption of the BBB. The best procedure is to perform two MRIs, one with and one without gadolinium enhancement (Behin et al. 2003). If MRI is not available, CT can be used to assess a lesion quickly; however, it is much less sensitive than MRI. Due to the lack of specificity of imaging methods, histological assessment of a biopsy sample is also required for a definitive diagnosis (Behin et al. 2003). Once a diagnosis is made, the tumour is staged and graded from 'I' to 'IV', where IV is the highest grade given, corresponding to the worst prognosis.

1.3.2 Pathology

Several different types of gliomas exist, variations are dependent on the type of glial cell from which they originated. The vast majority of glioma patients included in this research were adults with glioblastoma multiforme. The specific pathology of this malignancy is discussed below.

More than 50% of malignant gliomas are glioblastoma multiforme, making it the most common primary brain tumour among adults. It is a rapid-growing malignancy that exhibits resistance to both radio- and chemotherapy; however, even with aggressive management, recurrence is almost always inevitable. Glioblastomas "… consist mainly of undifferentiated anaplastic cells of astrocytic origin, which exhibit marked nuclear pleomorphism, necrosis and vascular endothelial proliferation" (Hayat 2011, p 4). Glioblastoma occurs mostly in the cerebrum of adults, and the tumour cells are usually arranged radially with respect to the necrotic region. Surgical resection, although often performed, is rarely curative due to the highly invasive and irregular growth of this type of tumour (Wirth et al. 2011).

1.3.3 Treatment

Treatment options for Glioma patients can vary depending on the location and mass of the tumour, as well as the age of the patient. Surgical removal or debulking (if possible) followed by chemoradiotherapy, is currently considered the standard strategy for treatment. Increased median life expectancy has been reported by using fractionated focal irradiation in daily fractions of two Gy given five days per week for six weeks, along with continuous temozolomide (75 mg per square metre of body-surface area per day), followed by six cycles of temozolomide (150-200 mg square metre of body-surface area per day for five days during each 28 day cycle) (Stupp et al. 2005).

1.3.4 Imaging

As stated in Section 1.3.1, radiologic imaging is used as part of the initial diagnostic procedure for glioma. Once a positive diagnosis is made, further imaging is performed to aid in surgical guiding and to monitor patient recovery and post-surgery condition. CT and MRI are both useful for the formation of an initial diagnosis. MRI in glioma imaging is usually enhanced with the intravenously-administered MRI contrast agent, gadolinium diethylenetriaminepentaacetate (Gd-DTPA). Once administered, Gd-DTPA is distributed throughout the vascular system. If there is a breakdown of the BBB, the extravascular leakage leads to pooling of Gd-DTPA in the affected region, increasing its intensity on MRI (Carr et al. 1984). Both CT and MRI are of limited use for monitoring treatment outcomes as they "… cannot reliably differentiate viable tumour tissue from treatment-induced non neoplastic changes, such as oedema, postoperative changes or radiation necrosis" (Vander Borght et al. 2010, p 10). Several different nuclear medicine radioisotopes have been investigated for use in glioma imaging. FDG is the most widely used PET tracer, and has been used extensively in glioma studies. The two tracers used in this research are [11]Carbon-Methionine (CMET) and 3'-deoxy-3'-[18]Fluorine-fluorothymidine (FLT).

1.3.4.1 2-Deoxy-2-[18F]Fluoroglucose

Neoplasmic cancer cells are known to metabolise glucose at a rate that is much higher than that of most healthy tissue, a phenomenon known as the Warburg Effect (Warburg 1956). FDG is a glucose analogue that is used to image the relative localised cellular metabolic rate (MRglc). As a result, FDG imaging is able to take advantage of the Warburg Effect, and is extensively used to stage and re-stage various pathologically proven cancers throughout the body, monitor treatment progression, and identify distant metastases (Kelloff et al. 2005).

Imaging cancers within the brain with FDG can be more problematic than other parts of the body, as healthy brain tissue also has a very high metabolic rate (see Section 1.2.1). It is therefore more difficult to see a distinction between normal tissue uptake and tumour uptake. FDG uptake is more likely to be noticeably elevated in high

grade (III and IV) than in low grade (I and II) glioma, with high hazard ratios (4.6 and 11 for right and left hemisphere tumours respectively) found for patients showing high FDG tumour uptake (Padma et al. 2003). However, up to 14% of high grade gliomas have been shown to exhibit lower FDG uptake than the surrounding tissue (Padma et al. 2003). FDG has shown limited utility in distinguishing tumour recurrence from radiation necrosis. Using contralateral white matter uptake as a normalisation standard, radiation necrosis has been successfully distinguished from tumour progression with a sensitivity of 86 ± 14 %, specificity of $22 \pm 6\%$, positive predictive value of $73 \pm 20\%$, and negative predictive value of $50 \pm 49\%$. These results were shown in a study by Ricci and colleagues (1998) where histopathologic confirmation of tumour progression was available.

1.3.4.2 [11]Carbon-Methionine

Methionine is one of 20 standard amino acids used in the production of proteins and generation of metabolic energy. It is one of 10 essential amino acids, meaning that it cannot be synthesised inside the human body and must be ingested directly. Methionine is required by the body for the processes of protein synthesis and the methylation of DNA, guanidoacetate, norepinephrine, and RNA (Fromm and Hargrove 2012). The BBB shows selective permeability to amino acids; methionine is one of a group of large neutral amino acids that are able to traverse the BBB via the L-Type amino acid transporter system (Betz and Goldstein (1978); Okubo et al. (2010); Oldendorf (1971)). Capillaries inside glioma tissue have been shown to have up-regulated amino acid transporter expression compared with healthy brain tissue (Miyagawa et al. 1998); this factor, combined with increased micro vessel density, leads to elevated CMET uptake (Kracht et al. 2003).

CMET-PET has been used as a means of imaging the rate of amino acid metabolism in glioma (Okubo et al. 2010). It has been found that CMET can provide superior tumour-healthy tissue contrast when compared with FDG (Bergstrom et al. 1983). Elevated uptake of CMET is also present in low grade tumours (Herholz et al. 1998). CMET has shown high utility in tumour detection and delineation, as well as differentiation between benign and malignant lesions (Kawai et al. 2011).

1.3.4.3   3'-deoxy-3'-[18]Fluorine-Fluorothymidine

The nucleoside thymidine is an essential component in the production and replication of DNA and RNA (Fromm and Hargrove 2012). FLT is phosphorylated within cells by thymidine kinase-1 (TK1) (Rasey et al. 2002), the increased concentration of which is an effective proxy for neoplasmic cellular proliferation. As stated by Munch-Peterson and colleagues (1995, p 70) "TK1 activity is known to fluctuate with cellular DNA synthesis, the activity being high in proliferating and malignant cells and low or absent in quiescent cells".

FLT cannot cross an intact BBB, resulting in very low uptake in healthy brain tissue (Chen et al. 2005). High FLT uptake in brain imaging only occurs when there is disruption of the BBB, which is often seen in glioma. Any measure that does not take into account transport methods (such as the Standardised Uptake Value (SUV)) can be misleading in FLT imaging, as it is likely that most FLT uptake is due to transport through the broken down BBB, and not due to trapping of FLT after phosphorylation by TK1 (Jacobs et al. 2005). This can result in high uptake in regions of BBB breakdown that are not highly proliferating, and low uptake in instances of glioma that involve minimal BBB disruption, which is possible even in highly proliferative tumours (Muzi et al. 2006).

In spite of the potentially confounding factors surrounding the nature of its uptake in the brain, FLT has shown promise as a diagnostic tool for the staging and evaluation of glioma. FLT may have greatest utility when used in conjunction with other modalities such as Gd-MRI and CMET when evaluating treatment effects and tumour recurrence (Jacobs et al. 2005).

1.4 Alzheimer's Disease and Mild Cognitive Impairment

As life expectancy increases, so too does the significance of diseases that primarily affect the elderly, such as dementia. It is estimated that there were over 266,000 Australians with dementia in 2011; that figure is expected to rise to over 942,000 by 2050 (Deloitte Access Economics 2011). AD is the most common form of dementia, accounting for 50-70% of all diagnosed dementia cases. The cost associated with dementia in Australia in 2009-10 has been estimated at $4.9bn (Australian Institute of Health and Welfare 2012).

Early clinical diagnosis of AD can be extremely difficult due to the gradual onset of symptoms and variation of symptomatic experience between individuals. The use of in-vivo cerebrospinal fluid (CSF) assays and brain imaging have led to identification of AD-related pathophysiological processes occurring as early as decades before the onset of clinically evident symptoms (Sperling et al. 2011). There are three main phases in the development of AD. The first stage is a pre-clinical, asymptomatic phase during which AD pathophysiology may start to present. The second stage is known as Mild Cognitive Impairment (MCI) (Albert et al. 2011). During this stage, the onset of some clinical signs of AD are observed, although not enough to cause significant impairment. Stage three is clinically diagnosable AD. There is a fluid continuum of progression between normal cognitive health and AD, and as such it can be difficult to establish a definitive diagnostic timeline of disease progression. Furthermore, MCI syndrome can occur independent of AD, with other causes such as brain trauma and other medical reasons such as Parkinson's disease being possible causes (Albert et al. 2011).

There is currently no cure for AD, and the only treatments available involve methods to lessen the severity of symptoms, rather than treat the disease itself. On average, life expectancy following diagnosis is seven years; less than three per cent of patients live for fourteen years after diagnosis (Shelton 2012).

1.4.1 Symptoms

The earliest symptoms of AD are often mistaken for cognitive decline as a normal part of aging, or as symptoms of stress or depression. The most commonly seen initial symptom is loss of episodic memory (the ability to form and keep new memories) (Shelton 2012). AD can remain undiagnosed for years, and the timing of the onset of symptoms and progression of the disease can vary greatly between patients.

Observable symptoms of MCI are similar to AD, but less severe. MCI symptoms include a decline in one or more areas of cognition that has either been noticed by a patient themselves or by a carer/family member, or has become evident in longitudinal cognitive testing. Symptomatic cognitive decline due to MCI should not be so severe as to significantly obstruct the patient's social or occupational life; such catastrophic decline is part of fully developed AD. In MCI due to AD, episodic memory is usually the most heavily affected area of cognition (Albert et al. 2011). In AD, the initial loss of memory and onset of confusion is followed by a range of other symptoms which varies between patients. These symptoms can include increased irritability, mood swings and aggression, loss of long-term memory, language breakdown, and gradual withdrawal of the patient as their cognitive decline progresses. Eventually the patient's bodily functions start to fail. Death results, although the specific cause can be a coexisting chronic condition or complications from other diseases such as pneumonia.

1.4.2 Diagnosis

Ante-mortem AD diagnosis cannot yet be undertaken with 100% certainty (Lu and Bludau 2011). The gold standard for AD diagnosis is obtained through post-mortem histopathological examination of brain tissue. Neuropathologic change is assessed according to three parameters: Amyloid Beta (Aβ) plaque score, neuritic plaque score, and neurofibrillary tangle stage (Hyman et al. 2012).

The first step in an attempt to make an ante-mortem MCI or AD diagnosis is clinical cognitive assessment. Standard criteria exist for clinical diagnosis of MCI due to AD (Albert et al. 2011). Cognitive assessment is typically performed by having the patient complete a series of assessments that test their cognitive abilities across a range of disciplines. The first such test proposed was the Mini Mental State Examination (MMSE) (Folstein et al. 1975). An improved, modernised version of the MMSE is now available, called the Standardized Mini Mental State Examination (Molloy and Standish 1997), which can be used as part of a clinical AD assessment. Other clinical cognitive assessment tools include the Clinical Dementia Rating (CDR) (Morris 1993) and the Global Deterioration Scale (GDS) (Reisberg et al. 1982). Assessment ideally occurs over a series of visits to enable some tracking of cognitive decline, although it is possible to make a diagnosis in a single visit if an informant is available to provide information on the patient's cognitive history. Clinically, MCI is defined as decline in one or more areas of cognition that result in the patient scoring significantly lower (1 to 1.5 standard deviations) in a cognitive assessment than would typically be expected for a patient of their age and level of education (Albert et al. 2011).

Clinical standards also exist for a diagnosis of AD through cognitive assessment (McKhann et al. 2011). The most important part of an AD diagnosis (as with an MCI due to AD diagnosis) is to attempt to establish episodic memory impairment. Generally, a patient is also required to show a decline in at least two other cognitive areas (aphasia, agnosia, apraxia, or disturbance in executive function) for a positive diagnosis of AD (McKhann et al. 2011).

In-vivo structural brain imaging is used clinically (if available) to help rule out other causes for the patient's symptoms such as stroke, subdural haemorrhage, or a tumour. The use of structural and functional brain imaging to detect AD pathology has been the subject of a large (and growing) field of research for several decades, and is further discussed in Section 1.4.5.

1.4.3 Pathology

There are three main pathological characteristics of AD; these are the accumulation of amyloid plaques, the formation of neurofibrillary tangles within the cellular matrix, and destruction of synapses and neurons (Kadir et al. 2012). Additionally, significant loss of white matter and reduction of cholinergic neurons has been observed in AD patients (Lombardo and Maskos 2015). An associated reduction in nicotine binding sites can be seen in-vivo by uitilising the PET tracers ^{11}C-nicotine and ^{18}F-A85380 (Herholz et al. 2007).

The presence of βA (also called senile) plaques in the brain has long been associated with AD, both as a component of intracellular neurofibrillary tangles, and as depositions in the extracellular vascular system (Hyman et al. 1989). The presence of βA plaques is considered to be a crucial element in the formation of a post-mortem AD diagnosis (The National Institute on Aging 1997).

Neurofibrillary tangles were one of the earliest pathological observations made in the study of AD, and are also considered a requirement for a positive post-mortem AD diagnosis (Perl 2010). There are several different proteins that comprise AD neurofibrillary tangles, including ubiquitin (Perry et al. 1987), cholinesterases (Mesulam and Asuncion Moran 1987), βA (Hyman et al. 1989), and tau (Lee et al. 1991). Tangles are observed in several different diseases (Wisniewski et al. 1979), which is why it is important that βA plaques are also observed to make a definitive diagnosis. Neurofibrillary tangles and amyloid plaques within the brain can only be directly observed in-vitro during a histological examination. Indirect observation of βA plaques in-vivo is possible using several PET tracers, including Pittsburgh compound B (PiB) and 2-(1-{6-[(2-[fluorine-18]fluoroethyl)(methyl)amino]-2-naphthyl}-ethylidene)malononitrile (FDDNP) (Vlassenko et al. 2012). Numerous ^{18}F PET tracers have been utilised to observe tau protein aggregates within neurofibrillary tangles, including THK523, T807, and T808 (Chien et al. 2013).

Neuronal and synaptic loss from AD can be seen in vivo using volumetric MRI. Sufferers of advanced AD will usually exhibit severe cerebral atrophy, which is

particularly evident in the widening of the lateral ventricles (Apostolova et al. 2012) and reduction of overall brain volume (Fox and Freeborough 1997). Accelerated atrophy of the medial temporal lobe is one of the well-established hallmarks of AD (Jack et al. 1997). In particular, increased atrophy of the hippocampus due to AD has been the subject of many studies (Morra et al. (2009); Ridha et al. (2006); Schott et al. (2005); Villain et al. (2008)). Severe atrophy of the hippocampus is considered to be one of the few reliable macroscopic indications of AD. A lack of significant hippocampal atrophy in a post-mortem brain examination is considered to be strongly suggestive that other causes of dementia need to be sought (Perl 2010).

1.4.4 Treatment

Current FDA-approved drugs for the treatment of AD include several different cholinesterase inhibitors and Memantine, which is an N-Methyl-D-asparate (NMDA) receptor antagonist. These drugs can provide temporary symptomatic relief, but have little to no effect on the progression of the disease. Research aimed at producing pharmacological treatments for AD is primarily focussed on development of 'disease modifying drugs' that may actually slow, halt, or even reverse the progression of the disease itself. An early start to treatment is likely to be vital to maximise the efficacy of such drugs (Salomone et al. 2012).

Non-pharmacological treatments for AD include cognitive training and stimulation, reminiscence, use of music, transcutaneous electrical stimulation, use of light, massage and touch, and physical exercise. Also beneficial is education for patients and carers, including strategies on how to deal with AD symptoms and episodes. Various combinations of these therapies have been shown to temporarily improve cognitive function, delay the need for institutionalisation, and improve the mood and behaviour of the patient (Olazaran et al. 2010).

1.4.5 Imaging

In-vivo brain imaging has been used extensively for AD research. The two modalities most relevant in this research are volumetric structural MRI and FDG-PET.

Volumetric structural MRI has been used to find quantitative differences between AD and HC brains in-vivo. Factors such as increased overall brain atrophy (Schott et al. 2005), enlargement of the lateral ventricles (Apostolova et al. 2012), and severe hippocampal atrophy (Ringman et al. 2010) are observed in AD brains.

Although there are many isotopes that have been developed for PET imaging, by far the most commonly used is FDG. As noted in Section 1.2.1, the brain requires a constant vascular supply of glucose. FDG in brain imaging is used as a means to indirectly observe MRglc. FDG "… is actively transported across the blood-brain barrier (BBB) into the cells where it is phosphorylated by hexokinase, then effectively 'trapped' " (Vander Borght et al. 2010, p 9). PET brain imaging with FDG has been used to detect depressed cellular metabolism in the temporo-parietal cortex (and specifically in the hippocampus) as a result of AD (McKhann et al. 2011). FDG-PET has also been used to detect the depression of cerebral metabolism in the posterior cingulate cortex of AD patients that are yet to develop clinically observable symptoms (Minoshima et al. 1997). In clinical trials, FDG-PET has been shown to be beneficial for diagnostic sensitivity when used in conjunction with other diagnostic methods (Silverman and Small 2002).

1.5 Brain Image Analysis

As high resolution structural brain images and a greater variety of functional imaging techniques become more widely available, the automated analysis of brain images continues to develop as a crucial tool for both research and clinical applications. A method that allows for voxel-by-voxel comparison of brain images to be made is to transform them to the same co-ordinate space. This is achieved through implementation of spatial transformations. Intra-subject image alignment can be

achieved using a rigid body transform, as no change to the overall shape or size of the images is desired. Inter-subject alignment is generally achieved utilising a two-stage process. Computationally simple linear transforms can be used to bring the images into approximate alignment, this serves as a starting point for the next stage. Nonlinear transforms can then be implemented to provide a much closer anatomical alignment, which is crucial for the study of small tissue volumes such as the hippocampus.

1.5.1 Linear Transforms

A rigid body transform involves up to two different types of transformation: translation and rotation. In a three dimensional volume, this provides up to six degrees of freedom. A rigid body transformation in the context of brain imaging is most useful for intra-subject registration, as no overall changes to brain shape or size are required to achieve a precise registration between multiple images of the same brain, provided a negligible amount of time has passed between images. Rigid body transformations are a subset of affine transformations, which involve up to 12 degrees of freedom. Affine transformations, as well as translations and rotations, can include zooms and shears.

An automated algorithm that attempts to find the optimal set of transformation parameters between two volumes will usually do so through an iterative process that has the goal of minimising a cost function. A popular cost function to use for within-modality registration is the sum of squared differences in voxel numbers between the two images. It is the minimisation of this parameter that should give the best registration (Friston 2007). However, the sum of squared differences is not of great use when it comes to inter-modality registrations, since there is not necessarily any correlation between anatomy and voxel number between imaging modalities. This is particularly relevant when attempting to create a functional-structural registration.

Inter-modality registration requires a more sophisticated approach. Early techniques for inter-modality registration involved manually marking corresponding features on each image that could then be aligned with one another (Pelizzari et al. 1989). This

approach can provide a high level of accuracy; however, it is cumbersome (particularly for batch processing of many images) and subject to operator error and inter-operator variability. Since then, techniques have been developed that can be used for fully automated inter-modality registration such as Mutual Information (Viola and Wells Iii 1997) and the Correlation Ratio (Roche et al. 1998), both of which rely on the use of joint probability density functions derived from a series of two dimensional intensity histograms to maximise the degree of likelihood between two image volumes.

1.5.2 Nonlinear Transformations

Natural variations in overall size and shape, as well as the effects of aging and pathology, can create large discrepancies between brains, which may render linear transforms useless for all but the most approximate alignment. In order to create a close registration that enables the overlay and comparison of small structures within the subcortex, higher order nonlinear transforms are required. Nonlinear transforms are usually applied after a linear transform has been used to gain an approximate alignment. Use of a linear transform to provide a starting estimate is very important, as nonlinear transforms for brain alignment usually conduct deformations over a small spatial scale (Andersson et al. 2007).

As is the case with linear transforms, nonlinear transforms generally operate by minimising a cost function. The assumption is that values of a set of parameters that minimise the cost function will correspond to the 'correct' alignment of the two images. Nonlinear warping is much more complicated and computationally intensive than the linear equivalent, involving potentially millions of degrees of freedom.

There are two general types of nonlinear transforms, label-based and intensity-based (Friston 2007). Label-based techniques work by identifying points or surfaces within the brain material that are common between brains. These elements are then aligned with each other, before fitting a series of splines and minimising 'bending' (Bookstein 1989) or 'membrane' energy (Andersson et al. 2007), or using a fluid model (Thompson and Toga 1996) to interpolate between the labelled points. The

use of this technique has limited application in brain registration. There can be significant variations in physical characteristics between healthy brains, such as disparities in the number of sulci. Changes resulting from aging and pathology can further reduce the number of physical features that are common between two brains (Andersson et al. 2007).

Intensity-based techniques operate by treating brains as unlabelled, continuous volumes and applying warping methods to optimise a cost function used to quantify the differences between the images. Nonlinear warping in the software package *FSL* (Smith et al. 2004) for intra-modality alignment uses a weighted combination of both label-based and intensity based-techniques (Andersson et al. 2007).

1.5.3 Segmentation

The resolution that can be achieved in cerebral imaging allows for clear definition of sub-structures within the brain. Segmentation of cerebral sub-structures allows for quantitative analysis of sub-structure volume in a structural image, and uptake/activity quantification within a substructure on functional images that are in precise alignment with a segmented structural image. This segmentation can be achieved manually through the marking of a structure boundary over its volume; this process is tedious and cumbersome. It requires significant expertise in cerebral anatomy and imaging characteristics, and is vulnerable to inter-operator variability and human error. Automated brain image segmentation provides a faster, mathematically consistent replacement to the manual option.

The automated segmentation of brain tissue can be performed through several different methods. Segmentation can be performed based on generalised tissue classification (grey matter, white matter, CSF) on MRI by creating an intensity-based separation model (Friston 2007). Some structures and tissue types are indistinguishable from one another based solely on signal intensity; models that incorporate segmentation of the structures of the subcortex do so through utilization of manually labelled data sets to assist in estimation of spatial location of the included structures. Since there is often little change in MRI signal intensity between

structures of the subcortex, methodologies that include their segmentation must also incorporate some means of boundary identification. This can be achieved by including the computation of tissue class probability statistics on a voxel-by-voxel basis, and estimating boundaries based on a statistical threshold (Fischl et al. 2002), and through use of deformable virtual surface meshes for each structure (Patenaude et al. 2011).

1.5.4   The Standardised Uptake Value, SUV_{MAX} and SUV_{PEAK}

The intensity of each voxel in a correctly reconstructed nuclear medicine image is directly proportional to the amount of radioactivity detected within the volume. While this can be useful in a clinical setting (e.g. qualitative visual comparisons of regional FDG uptake between brain structures for clinical assessment of AD), the ideal scenario is one in which regional volumetric activity concentration can be quantified. Such quantification of regional tracer activity allows for comparisons between subjects, study protocols and scanners, all of which are crucial for researching new imaging modalities and tracer types. Absolute quantification of tracer uptake concentration can only be achieved through arterial blood sampling to obtain the tracer time-activity curve. This requires insertion of arterial lines so that multiple blood samples can be analysed during scanning (Gjedde 2001). SUV was developed as a means to achieve semi-quantitation in PET imaging. By correcting for isotope decay time, patient weight (or body surface area) and injected dose, an activity concentration can be calculated.

PET imaging with FDG is often used in the assessment of treatment response to cancer therapy. Changes in SUV within the tumour over time are used as an indicator of treatment response. The SUV_{MAX} is often utilised, which is defined as the hottest voxel within the tumour volume (Vanderhoek et al. 2012). The SUV_{MAX} has gained popularity in clinical settings, largely due to the ease with which it can be identified and the simplicity in the way in which it is defined. However, high variance is a concern, owing to the fact that the measurement is only taken in a single voxel.

The SUV$_{PEAK}$ was proposed to attempt to reduce this degree of variability by taking the average uptake of a number of voxels (Wahl et al. 2009). SUV$_{PEAK}$ can be broadly defined as an ROI that is considered to be indicative of the highest uptake part of the tumour. The SUV$_{PEAK}$ is usually normalised to background uptake, the method of which varies depending on the tumour type and location within the body. The shape and size of the ROI can also vary depending on the imaging modality and tumour site. The PERCIST guidelines (Wahl et al. 2009) were developed to increase the degree of uniformity in the way in which SUV$_{PEAK}$ is defined and calculated, these guidelines were used for this body of work. According to the PERCIST guidelines, the SUV$_{PEAK}$ is the $1cm^3$ sphere of highest average activity inside the tumour mass, normalised to background (healthy tissue) uptake, which results in a value that quantifies how different the uptake in the tumour volume is from that which is seen in healthy tissue.

1.6   Outline of Thesis

This research is comprised of work performed on two different sets of patient data. Each Chapter is its own self-contained body of work, and is laid out as such, containing chapter-specific sections from literature review to conclusion.

Chapters Two and Three are based on a data set acquired at the Western Australian PET centre at Sir Charles Gairdner Hospital, Perth. As part of a study into treatment method optimisation in recurrent glioma, 34 patients were subjected to a range of structural and functional brain imaging. The PET tracers used for the work, although not new, are seldom seen in a clinical setting. Chapter Two focusses on the differences in retained activity measured at different post-injection time points for each of the tracers. Information of this type will become crucial for the development of standardised imaging procedures should these compounds become more commonly used in clinical settings.

Chapter Three assesses the survival prediction utility of each of the PET tracers, as well as Gd- MRI. The assessment was made using a novel semi-automated process that quantifies the volume of elevated tracer uptake/gadolinium enhancement in the

tumour affected brain region. Optimisation of treatment planning and survival outcomes in recurrent glioma is heavily dependent upon reliable imaging of tumour tissue. Novel uptake quantification methods such as the ones used in Chapter Three aid in the assessment of various imaging modalities, and can increase their value in the post-treatment glioma setting.

Chapters Four and Five utilise data from the Australian Imaging Biomarkers and Lifestyle (AIBL) and Alzheimer's Disease Neuroimaging Initiative (ADNI) archives. In Chapter Four, two different methods of volumetric hippocampal masking are compared with regards to their ability to find uptake differences between 30-subject groups of healthy control (HC), mildly cognitively impaired (MCI), and AD subjects, based on FDG-PET uptake in the masked volume. Automated brain image assessment has the potential to build upon established clinical AD detection methods, with computationally efficient and reliable analysis techniques offering the potential to provide earlier and more accurate diagnoses.

Chapter Five examines the utility of an optimised volumetric hippocampal mask as a stand-alone diagnostic tool for AD. The scenario in which a brain PET image is acquired without an accompanying volumetric MRI is included, as this is often the case in a clinical setting. Volumetric hippocampal masking may become a significant component of AD diagnosis if a future shift towards imaging and biomarker assessment eventuates in clinical practice.

Chapter Six contains a summary and overview of the thesis content, and recommendations for expansion and continuation of this research in the future.

2 Optimisation of CMET-PET and FLT-PET Acquisition Time in Glioma patients

2.1 Introduction and Literature Review

Nuclear medicine studies require the implementation of a waiting period between the administration of an isotope and the commencement of imaging. The length of time between administration and imaging varies with modality, radionuclide and disease pathology. The reason for the waiting period is to allow sufficient time for the distribution of the radionuclide within the patient, so that the contrast between target and other/background tissue is maximised.

FDG is the most commonly used PET tracer, with ^{18}F having a half-life of 110 minutes. Despite the widespread use of FDG, there is no gold standard consensus on the optimal post-injection waiting period for brain imaging, partially due to differences in uptake times between patients with varying age and BMI. Due to its relatively long half-life, the decay of the nuclide itself need not be of significant concern when considering post-injection time differences in the order of an hour. Imaging methodology can be altered to adjust the way in which volumes of interest are visualised, two such adjustments are dual time point imaging (Matthies et al. 2002) and delayed imaging (Kubota et al. 2001). The European Association of Nuclear Medicine recommends a minimum post-injection wait time for FDG brain imaging of 30 minutes (Varrone et al. 2009), but times of 60-90 minutes are common (Delbeke et al. 2006).

The 20 minute half-life of ^{11}C means that ideal post-injection waiting times are likely to be much shorter for CMET than those used for FDG. A study by Herholz and colleagues (1998) used 31 subjects with various gliomas with a mixture of images taken pre- and post-treatment, and acquired PET data continuously for 60 minutes immediately after injection. Data were then reconstructed to produce two sets of images, one containing data from 0-30 minutes post-injection and another from 20-60 minutes. SUV$_{PEAK}$ was utilised to quantify tumour-background contrast, which was defined as the average SUV of an 8mm diameter circle in the transaxial plane, in

the highest uptake area of the tumour. To account for inter-subject differences in healthy brain tissue uptake, the ratio of tumour SUV_{PEAK} to the average SUV within a contralateral circle, mirrored about the mid-sagittal plane was taken (scaling processes of this nature are referred to as background normalisation from this point on). No significant differences in tumour-contralateral tissue uptake were found between the image frames. However, the researchers favoured the longer imaging delay time due to "… the possibility that a very early measurement could be biased by significant intravascular activity" (Herholz et al. 1998, p 1322).

A study by Aki and colleagues (2012) that included 24 pre-treatment Glioblastoma Multiforme patients found that the normalised tumour SUV was significantly higher at an imaging time of 25-35 minutes than it was at 5-15, and 15-25 minutes. The background normalisation method employed was to use the mean SUV from a manually drawn ROI in the contralateral frontal cortex. The maximum voxel number within the tumour volume (SUV_{MAX}) was used for the tumour SUV, a method which is often used due to the ease with which the maximum voxel can be identified. It is, however, prone to increased variability and lower reproducibility than the use of a volumetric SUV_{PEAK} region centred over the area of highest uptake within the tumour volume (Wahl et al. 2009).

A study by Chen and colleagues (2005) comparing FDG and FLT for PET brain tumour imaging acquired FLT data using a 75-minute dynamic acquisition protocol starting immediately post-injection, to produce 5 x 1, 4 x 5, 2 x 10, and 6 x 5 minute frames. These images were acquired for 11 post-treatment patients with a range of gliomas. SUV_{PEAK} was defined as the mean SUV within the highest uptake 20% of voxels in the tumour region; background normalisation was performed by taking the ratio of the SUV_{PEAK} to the uptake in the contralateral cerebellar tissue. The tumour-background contrast "… peaked slightly after 5-10 min following injection and remained constant through the 75-min scan" (Chen et al. 2005, p 948). The conclusion drawn was that "… imaging can commence shortly after tracer injection and 35 min of imaging is sufficient to obtain excellent image quality" (Chen et al. 2005, p 950). No quantitative analysis aimed at distinguishing between time points was presented.

Another study by Jacobs and colleagues (2005) also imaged glioma patients using FLT at multiple time points on a mixture of pre and post-treatment gliomas. The frames were: 6 x 10s, 3 x 20s, 2 x 30s, 2x 60s, 2 x 150s and 16 x 300s. A circular 8mm diameter ROI in the axial plane was placed in the area of highest uptake and background normalisation was performed by taking the ratio to the contralateral 8mm circle. Reported findings in regards to tumour-background contrast were in accordance with (Chen et al. 2005).

2.2   Materials and Methods

2.2.1   Subjects and Imaging

CMET-PET images from 12 (mean age 60, age range 39-73, eight males and four females) and FLT-PET images from 18 (mean age 60, age range 36-77, 13 males and 5 females) stage III-IV glioblastoma multiforme patients from Sir Charles Gairdner Hospital (SCGH) were included in this research, after consulting with their oncologist and giving written informed consent. Patients were excluded from the research if they were pregnant, had a medical contraindication to MRI or PET imaging, or if their clinician considered them too cognitively impaired to give informed consent. Each subject was given standard treatment at SCGH, in accordance with the Stupp schedule (Stupp et al. 2005). This schedule involves surgical debulking/biopsy, followed by radiotherapy and three cycles of temozolomide chemotherapy, and Gd enhanced T1 and T2 weighted MRI around the time of the final chemotherapy cycle.

PET tracers were synthesised at the R.A.P.I.D laboratories, Medical Technology and Physics, in SCGH. FLT "… was produced using the Tracerlab MX Synthesis module (GE) with commercially obtained disposable cartridge hardware kits ("ABX-FLT Hardware Kit for GE TracerLab MX Synthesizer (Cartridge version) for the Synthesis of [18F]-FLT," #K662TM) and reagents ("ABX-FLT Reagents Kit for GE TracerLab MX Synthesizer (Cartridge version) for the Synthesis of [18F]-FLT," #K-653TM) purchased from ABX. 25mg BOC-FLT vials were also obtained commercially from ABX ("ABX-FLT Reagents Kit for GE TracerLab MX

Synthesizer (Cartridge version) Boc-FLT, Precursor for [18F]-FLT," #K-653TM-P)" (P. Gibbons, SCGH Radiochemist, *Personal Communication*, 30/09/2014). CMET "was produced using the C11 Pro Synthesiser (iPhase Technologies) with commercially obtained disposable cartridge hardware kits (iPhase-11C Pro Disposable Hardware Kit) and reagents obtained from ABX including 1mg L-homocysteine precursor" (P. Gibbons, SCGH Radiochemist, *Personal Communication*, 30/09/2014).

Subjects fasted for a minimum of four hours prior to the intravenous CMET administration, which was performed through a cannula inserted into a peripheral vein; the administered dose was adjusted for patient weight [300 MBq x body surface area (m^2)]. No subject preparation was required for FLT imaging. FLT administration was identical to CMET, with the exception of dose, which was 100 MBq x body surface area (m^2). CMET and FLT PET studies were performed within seven days of each other and within two weeks of the MRI.

Volumetric MRIs were acquired on a Phillips Acheiva 3T scanner at SCGH. Images were acquired at 3T field strength in the sagittal plane, pixel size 1x1 mm^2, slice thickness 1 mm, matrix size 256x256 pixels.

PET/CT images were acquired on a Siemens Biograph/Sensation 16 slice PET/CT scanner at the WA PET Centre, at SCGH. Patients were positioned in the head first, supine position. CMET imaging was performed using four consecutive 10 minute acquisitions, beginning between five and 15 minutes post-injection. PET images were acquired in the axial plane, matrix size 168 x 168, pixel size 2.03 x 2.03 mm, slice thickness 2 mm, 82 slices, and Gaussian conv kernel 5 mm FWHM. For attenuation correction, an axial CT was performed immediately prior to the first PET acquisition with the following specifications: 120 kVp, 150 mAs, 512 x 512 matrix, pixel size 0.59 x 0.59 mm, slice thickness 3 mm, slice separation 2 mm, collection diameter 500 mm, reconstruction diameter 300 mm. The FLT protocol differed from that used for CMET in that there were two separate 15 minute PET acquisitions, beginning between 10-20 and 70-80 minutes post-injection. Each FLT acquisition was attenuation corrected using a CT taken immediately prior to the acquisition; the same CT acquisition parameters used for the CMET scan were employed.

2.2.2 Image Processing

Raw PET image voxels were converted to standardised uptake values (SUV) (Bq/mL) in accordance with the vendor neutral pseudocode (20120928) developed by the Quantitative Imaging Biomarkers Alliance SUV Technical Subcommittee (QIBA) (Kinahan et al. 2012).

The series acquisition time, injection time, injected dose (D_{inj}), and patient weight (w) were acquired from the DICOM header. The decay time (Δt) is the difference between the series acquisition time and the injection time. The decay factor (DF) at the start of the acquisition was calculated using:

$$DF = \exp^{\frac{\ln(2)*\Delta t}{t_{\frac{1}{2}}}} \qquad (1)$$

Where $t_{\frac{1}{2}}$ is the radionuclide's physical half-life. An SUV factor (SF) can then be found by:

$$SF = DF\left(\frac{w}{D_{inj}}\right) \qquad (2)$$

SUV conversion factors were calculated using a Matlab script, which can be found in Appendix 1.

Several stages of spatial registration were performed to align all of the PET and MR images to a standard space. The FreeSurfer (Martinos Centre for Biomedical Imaging, http://surfer.nmr.mgh.harvard.edu/) routine *mri_convert* was used to convert the image DICOMs into *FSL* (Smith et al. 2004) Nifti format.

CMET Inter-acquisition patient movement correction was performed using the *FSL* (Smith et al. 2004) routine *MCFLIRT* (Jenkinson et al. 2002). This involved the calculation of rigid body transforms (six degrees of freedom) to co-register the 20,

30, and 40 minute acquisition to the 10 minute acquisition. Information in the Nifti headers was used to translate the origin of the 10 minute acquisition to co-register it with the attenuation correction CT.

All CTs were co-registered with each of their intra-subject MRIs using a six degrees of freedom rigid body transformation with the *FSL* (Smith et al. 2004) routine *FLIRT* (Jenkinson et al. 2002).

The T2 MRIs were co-registered to the McConnell Brain Imaging Centre (Montreal Neurological Institute (MNI), McGill University Montreal) 152 nonlinear 6th generation T1 1mm resolution brain template using a 12 degree of freedom affine transformation with *FLIRT* (Jenkinson et al. 2002). The co-registration between the T2 subject MRIs and the T1 MNI template was superior to that for the T1 subject MRI-MNI. Co-registration of the T1 subject MRI to the MNI template was achieved through a six degree of freedom rigid body registration to the T2 image. This process is illustrated in Figure 13.
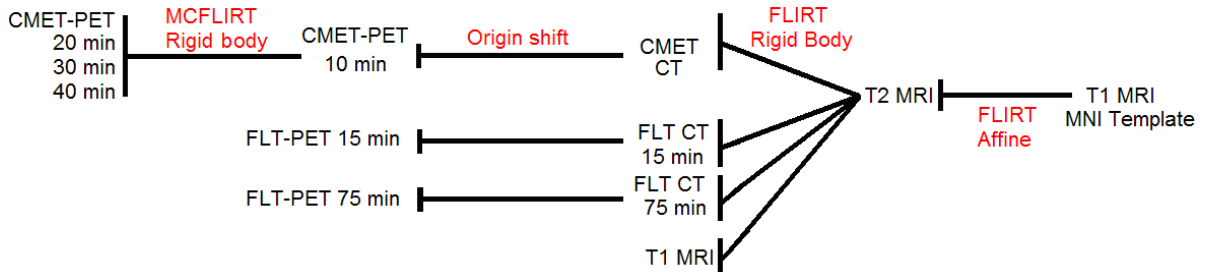
Figure 13, A schematic representation of the image co-registration process for the glioma study cohort.

The transformation matrices that led to a PET-MNI or T1-MNI registration were concatenated so that a single transform could be used for each image. This resulted in image volumes only being resampled once to minimise resampling errors.

2.2.3 Defining the SUV$_{PEAK}$ and Performing Background Normalisation

SUV$_{PEAK}$ was defined as the $1cm^3$ sphere of highest average activity inside the tumour mass, in accordance with the PERCIST criteria (Wahl et al. 2009). This was

found by manually defining a tumour VOI using the MNI co-registered MRIs and relevant PET image, then employing a python (Python Software Foundation, version 2.7) script (Appendix 2) to search the VOI for the central voxel of a 1cm^3 sphere in which the average SUV is maximised.

A contralateral 1cm^3 sphere was used for the background healthy tissue normalisation. The contralateral sphere was found by employing a reflection about the mid-sagittal plane, which is parallel with the Y-Z plane in MNI template space. The CMET SUV_{PEAK} was normalised to background uptake by taking the ratio of the SUV_{PEAK} to the average uptake in the contralateral sphere. Due to the very low uptake of FLT in healthy brain tissue, FLT background normalisation was performed by subtracting the mean of the contralateral sphere from the SUV_{PEAK}. This was performed as the SUV_{PEAK}/background ratio is greatly affected by a small change in a very small denominator. Figure 14 illustrates the background normalisation procedure: the green rectangles represent the search VOI for this subject. This is overlaid onto the T1 MRI and 10 minute CMET PET image, which has been thresholded to indicate the location of the uptake peaks (which are well contained within the green VOI to ensure the global tumour maximum is found). The light blue circle indicates the SUV_{PEAK} volume, and the dark blue circle is the region used for background normalisation.
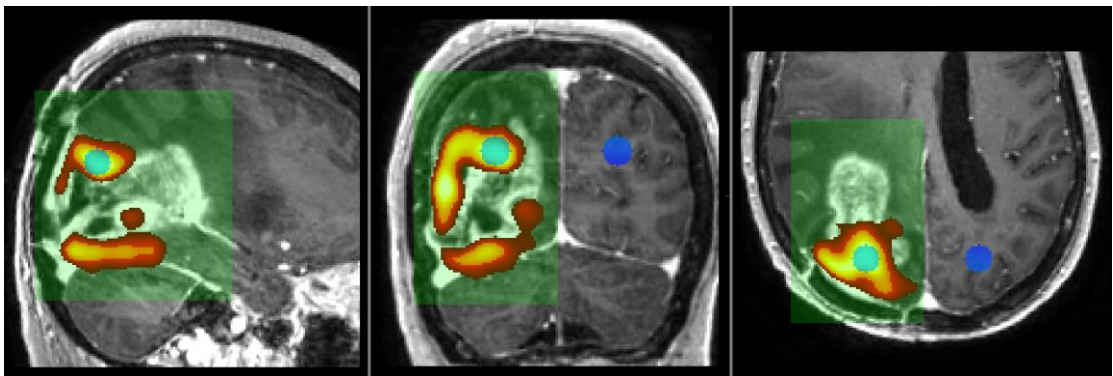
Figure 14, An illustration of the SUV $_{PEAK}$ normalisation process. A subject T1 MRI is overlaid with the areas of highest CMET uptake (red-yellow). The green rectangle is the SUV_{PEAK} search VOI, inside of which the SUV_{PEAK} volume is seen (light blue circle). The contralateral background normalisation volume is the dark blue circle.

2.3 Results

Figure 15 presents a line plot overlaid with a box and whisker plot showing the Normalised SUV$_{PEAK}$ at each post-injection CMET time point, each subject is represented by a single coloured line.
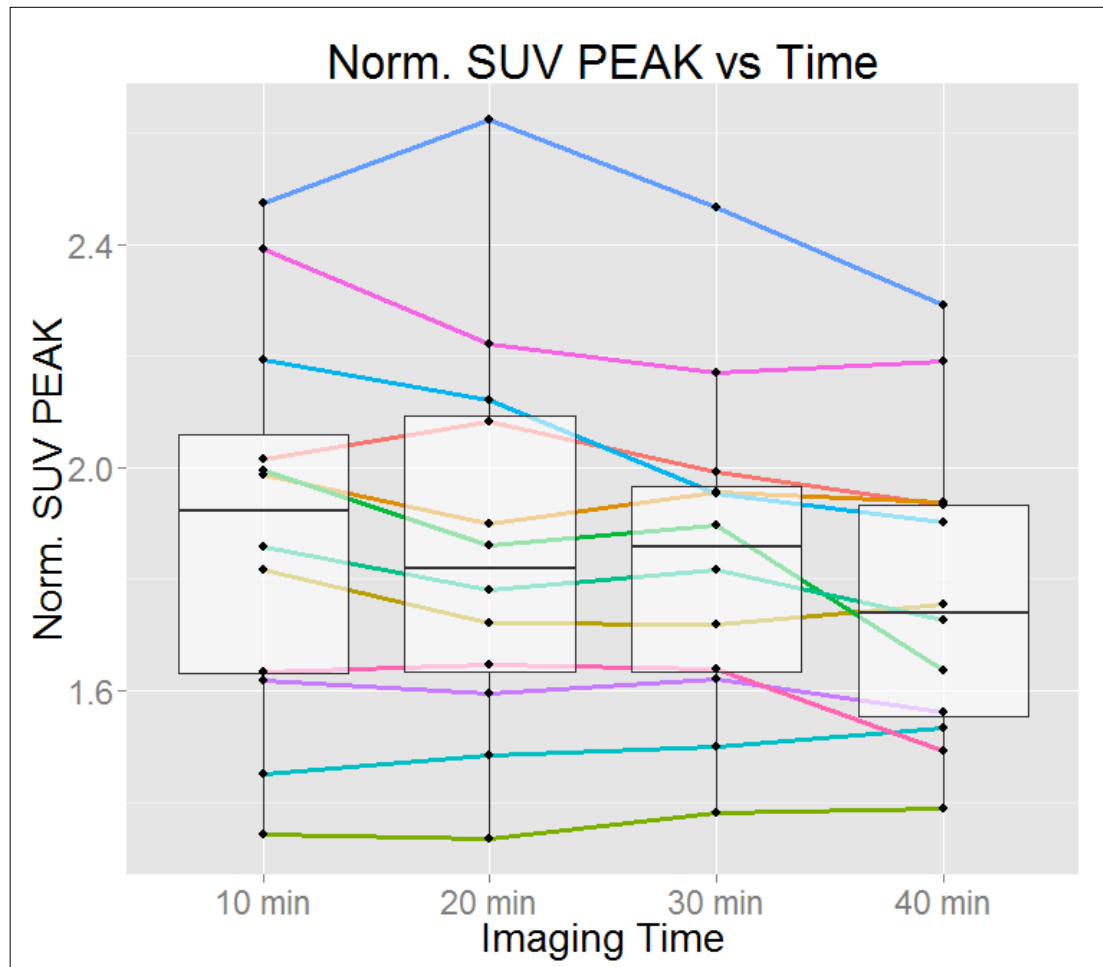
Figure 15, A boxplot of the raw normalised CMET SUV$_{PEAK}$ data, overlaid with line plots representing each subject.

In order to more easily identify the time point differences at group level, inter-subject normalisation was performed by subtracting each subject's mean uptake across all time points from their uptake at each time point. The results are presented in Figure 16.
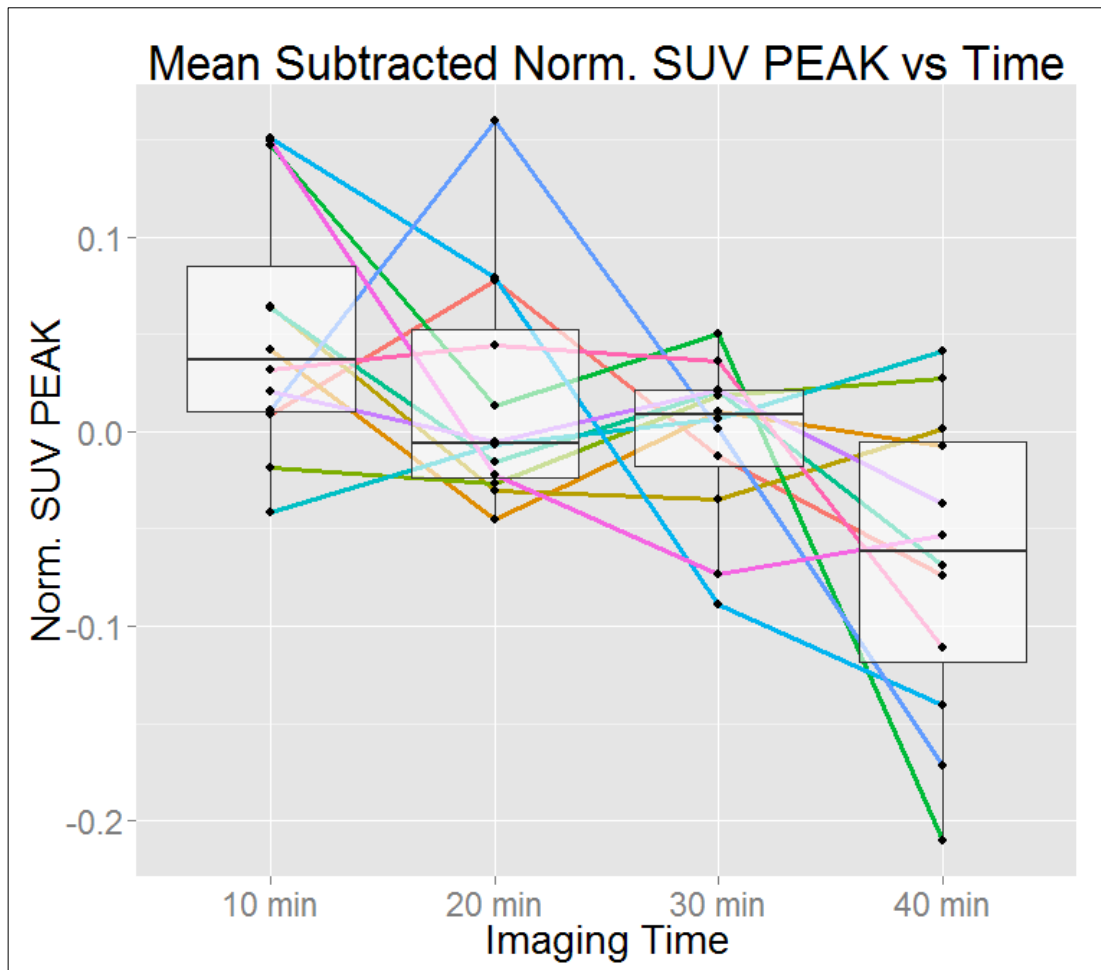
Figure 16, A boxplot of the mean subtracted normalised CMET SUV_PEAK data, overlaid with line plots representing each subject.

Repeated measures ANOVA with Tukey's all-pair comparisons was conducted on the raw data to determine whether there was a significant difference between time points. Statistically significant differences were found between the 20 and 40 minute ($p < 0.01$) and 10 and 40 minute ($p < 0.001$) time points.

Figure 17 and Figure 18 are graphical displays of the FLT data, utilising the same methods depicted in Figure 15 and Figure 16 for the CMET data.
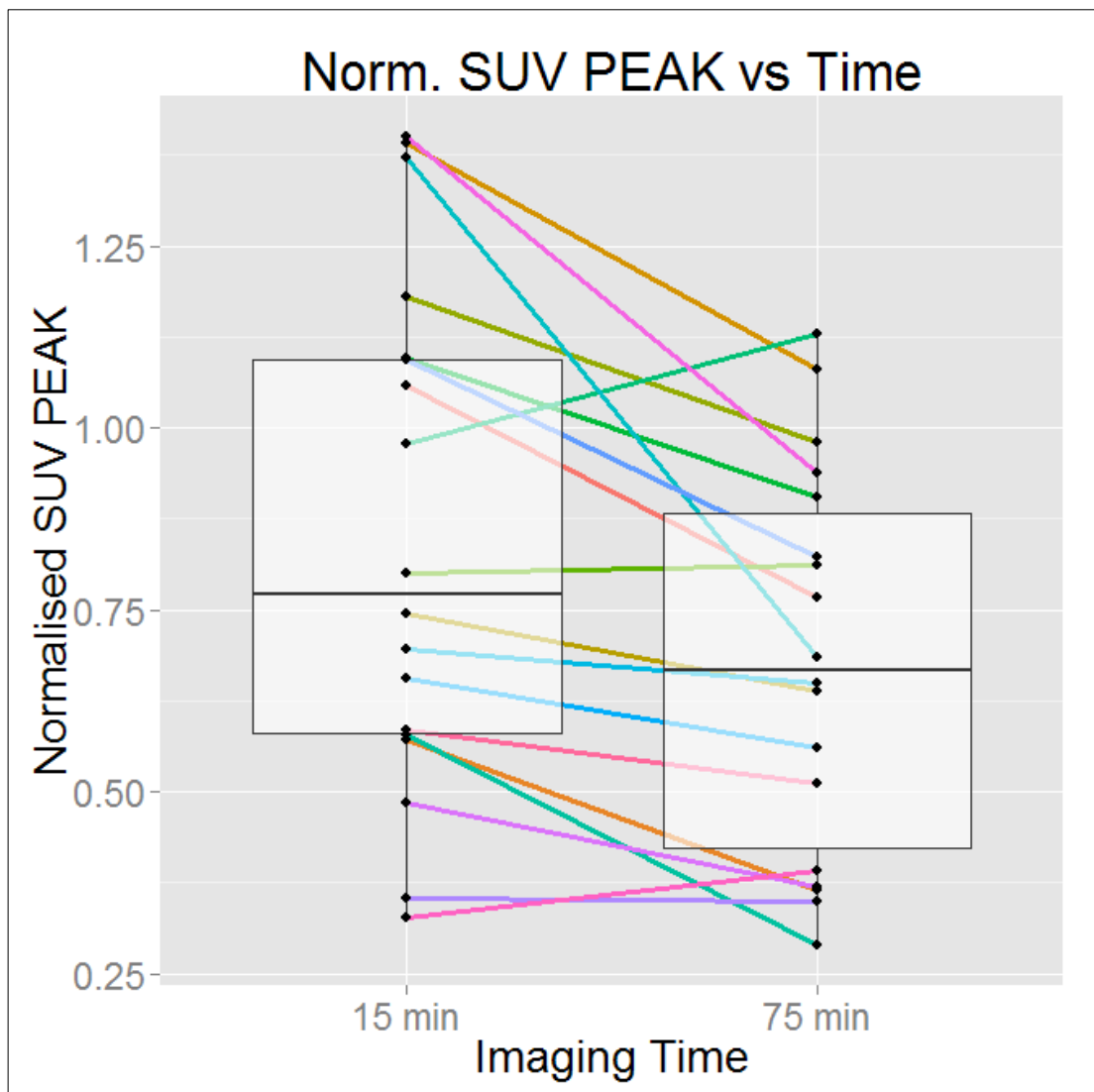
Figure 17, A boxplot of the raw normalised FLT SUV_{PEAK} data, overlaid with line plots representing each subject.

A two-sided paired t-test found that there was a statistically significant difference between the time points in Figure 17 (p<.005).
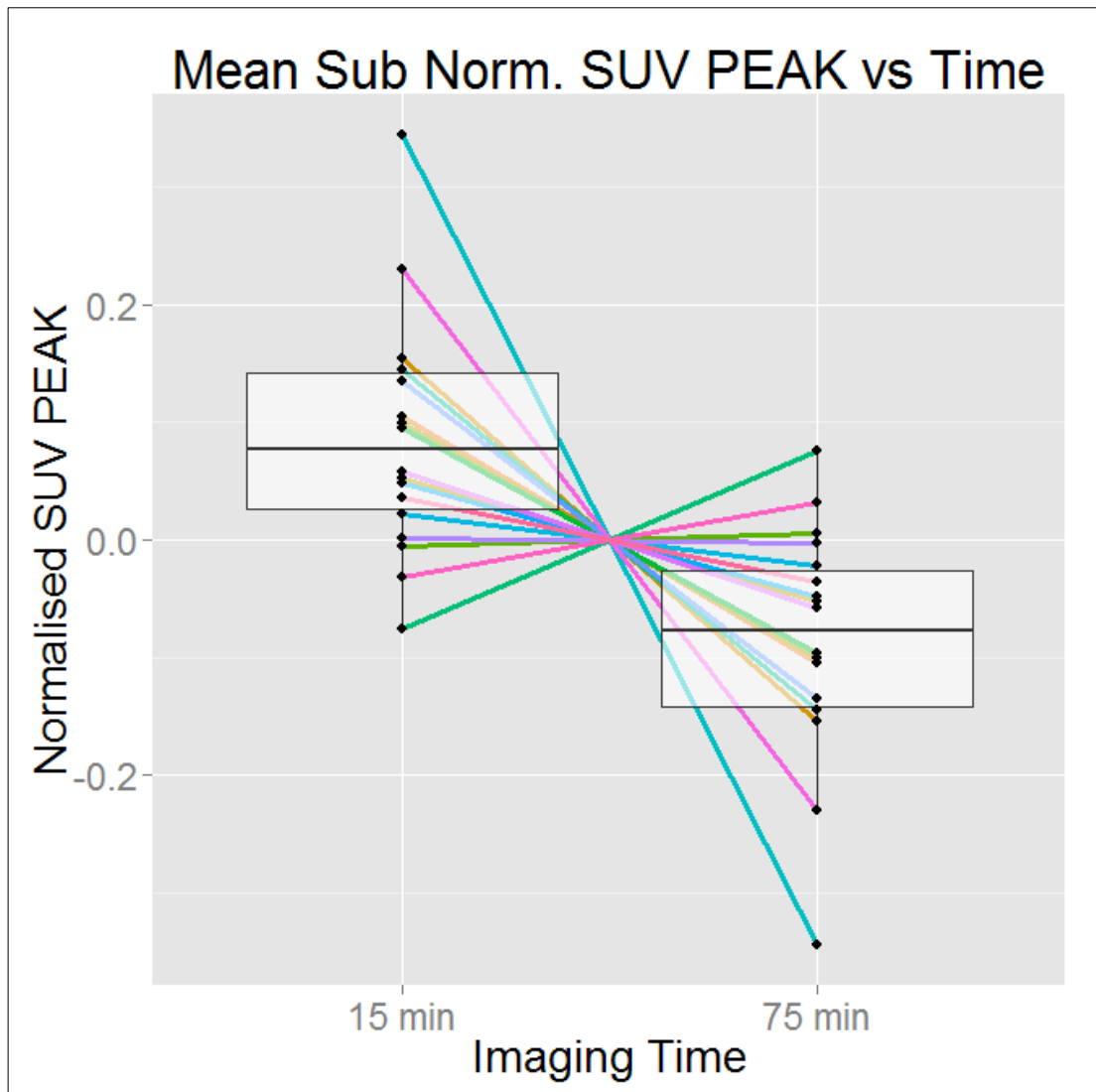
Figure 18, A boxplot of the mean subtracted normalised FLT SUV_{PEAK} data, overlaid with line plots representing each subject.

2.4 Discussion

The tumour-background contrast as defined on CMET-PET was significantly higher at 10 and 20 minutes than at 40 minutes post-injection in this group of post-treatment glioblastoma multiforme patients. Consequently, the recommended post-injection time is less than 40 minutes. Longer post-injection times ranging from 20-60 minutes have been recommended in previous studies (Aki et al. (2012); Herholz et al. (1998)). However, those studies used different methods to quantify normalised peak tumour uptake that are more prone to operator error and lack of reproducibility (see section 2.1). The small sample size (n=12) in this research is of concern, and repeat

studies with larger samples are required to achieve increased certainty in the results. A single attenuation correction CT was acquired for all four CMET-PET imaging time points. Rigid body transformation was employed to minimise movement artefacts between acquisitions, however it is possible that small attenuation correction errors were introduced as a result of imperfect movement compensation during imaging.

The significance in the FLT images between the 15 and 75 minute time points differs to those noted in previous studies (Chen et al. (2005); Jacobs et al. (2005)), which found a slight increase in tumour-background contrast at 5-10 minutes and that uptake remained fairly constant up until 75 minutes post-injection. However, a lack of temporal statistical analysis in the aforementioned studies makes it impossible to quantify the level of agreement between the results. The aforementioned studies also calculated background healthy tissue normalisation by taking the ratio of the tumour SUV ROI to a healthy tissue ROI. Given that very low FLT uptake is seen in healthy brain tissue where there is no BBB disruption, the method used for this study was to subtract the tumour SUV PEAK from the contralateral normalisation volume to avoid large changes in the normalised SUV PEAK resulting from a small change in the background uptake. Further work is required to make a more precise recommendation regarding the ideal post-injection time point for the commencement of glioma imaging with FLT; however, it is recommended based on these results that it should occur at less than 75 minutes.

Counter-intuitively, image co-registration between the T2 subject MRIs and the T1 MNI template was superior to that of the T1 subject MRIs; this was possibly due to extreme pathology having a greater effect on the intra-modality cost function. An affine transformation was used to co-register each subject T2 MRI to the T1 MNI template, due to the fact that a closer registration was achievable with an affine transformation than with rigid body. Complete removal of yaw and roll tilt was essential to the background normalisation process, as calculating the placement of the contralateral SUV PEAK sphere was performed via a reflection about the mid-sagittal plane, which is parallel with the Y-Z plane in MNI space after co-registration.

This method for the determination of a Normalised SUV PEAK region is a computationally efficient, largely automated process that can be applied to a range of isotopes and imaging modalities. The combination of spatial registration and reflection about the mid-sagittal plane for background uptake normalisation circumvents the need for manually marking anatomical VOIs, this in turn requires significant expertise and time, and is prone to reproducibility errors.

There were some limitations to the method used for SUV background normalisation. Any lesions where the SUV PEAK was within 6mm of the mid-sagittal plane could not be included in this work, as the tumour and contralateral regions would be at least partially sampling the same volume. Patients with bilateral lesions could only be included if the region used for background normalisation was healthy tissue. One possible method of circumventing this issue would have been to use a VOI within the cerebellum for background normalisation. Substantial uptake peaks often exist outside the brain for both CMET and FLT, which are obviously not of interest for glioma imaging. Separating these peaks from those within the brain can be extremely difficult and potentially impossible for lesions that are close to the skull.

2.5 Conclusion

CMET and FLT continue to show utility in glioma imaging, both for pre-treatment tumour staging and radiotherapy guidance, as well as in post treatment quantification of treatment efficacy and pseudoprogression. In order for these radionuclides to be used regularly in a clinical setting, information regarding temporal changes in tumour-background contrast will be important for establishment of imaging procedures. A semi-automated method was utilised to determine the tumour-background contrast in a group of post-treatment gliobastoma multiforme subjects. CMET images were acquired at 10, 20, 30 and 40 minutes post-injection, and the contrast was significantly higher at 10 and 20 minutes than at 40 minutes. FLT images were acquired at 15 and 75 minutes post-injection, and the contrast at 15 minutes was significantly higher than at 75 minutes. It is therefore recommended that imaging of glioma patients using CMET and FLT should commence prior to 40 and 75 minutes post-injection respectively.

3 Survival Rate Analysis of Gd-MRI, CMET-PET, and FLT-PET in Glioma Patients

3.1 Introduction and Literature Review

The ability to differentiate between healthy tissue, viable tumour mass, and treatment related tissue effects such as necrosis and oedema is essential to maximise the efficacy of cancer treatment. The extremely invasive nature and radial growth pattern of gliomas contribute to a high percentage of treatment failure and tumour recurrence (Wirth et al. 2011), partially due to the difficulty in correctly identifying and removing viable tumour tissue.

The most commonly used clinical treatment for glioma is surgical debulking (if possible) followed by chemo-radiotherapy (Stupp et al. 2005). This can produce a range of tissue effects, including necrosis and disruption of the blood brain barrier, which can be mistaken for actual tumour progression using Gd-MRI (Brandsma et al. 2008). This phenomenon is known as pseudoprogression, and it is thought to occur in 20-30% of cases (Brandsma and van den Bent 2009). The ability to recognise treatment-related effects and correctly identify the extent of any tumour recurrence is crucial to providing an accurate prognosis. It can also improve patient outcomes by allowing for planning of more appropriate follow-up treatment. Used in conjunction with structural radiologic imaging, functional imaging using CMET-PET and FLT-PET may improve the sensitivity and specificity of post-treatment clinical assessment.

There is evidence to suggest an SUV peak ROI to contralateral background uptake ratio in CMET-PET can be used to evaluate post-treatment high grade brain tumour recurrence and predict survival (Van Laere et al. 2005), and that it is superior to FDG-PET or T1 Gd-MRI for this purpose (Tripathi et al. (2012); Singhal et al. (2012)). CMET PET tumour uptake has also shown utility in predicting survival outcome in low grade glioma (Ribom et al. 2001). An optimal tumour/contralateral uptake ratio of 1.5 has been determined for the differentiation of tumoural and non-tumoural lesions using CMET-PET (Herholz et al. 1998). This threshold has been

suggested as a means of defining viable tumour volume in order to track the success of chemotherapy over time (Herholz et al. 2003).

Studies using multiple FLT-PET images taken during and post-treatment have shown a correlation between within-patient treatment response (a reduction in the tumour SUV_{PEAK} over time) and increased patient survival time (Hoeben et al. 2013). This method of predicting survival time in cancers of the head and neck has produced better results than similar methods using Gd enhanced MRI (Chen et al. (2007); Schwarzenberg et al. (2012)). There have been attempts to use inter-subject differences in tumour uptake as measured by FLT-PET SUV analysis at a single time point to discriminate between treatment related effects and genuine progression, and to predict survival time that have failed to produce statistically significant results (Spence et al. 2009).

Longitudinal survival data is available for a group of glioma patients that have undergone standard clinical treatment and follow-up imaging with FLT-PET, CMET-PET and volumetric Gd-MRI. This provides an opportunity to investigate each modality's utility in survival time prediction based on volumetric thresholding of the tumour affected region.

3.2 Materials and Methods

3.2.1 Subjects and Imaging

The initial patient cohort from which the data was taken is the same as described in section 2.2. CMET-PET images from 23 (mean age 58, age range 36-77, 16 males and seven females), FLT-PET images from 24 (mean age 57, age range 34-77, 17 males and seven females), and T1 weighted Gd-MRI images from 26 (mean age 56, age range 34-77, 19 males and seven females) subjects were included. The 15 minute and 20 minute post-injection scans were used for FLT-PET and CMET-PET respectively. This allowed for the largest amount of data to be included (due to some inconsistencies with scanning times), whilst using delay time points that were found

to produce the highest tumour to background contrast using the normalised SUV PEAK method described in Section 2.

3.2.2 Image Processing

All images were normalised to the 1 mm^3 resolution MNI 152 T1 MRI template using *FSL* (Smith et al. 2004), as outlined in Section 2.2. A modality-dependent thresholding method was then employed in an attempt to define a viable tumour volume.

To establish and demarcate a viable tumour volume in the CMET-PET images, a method that enabled contralateral background normalisation on a voxel by voxel basis across an entire hemisphere was used. Firstly, the image volume was masked using the *FSL* (Smith et al. 2004) MNI space brain mask, to remove any counts detected outside the brain volume. Secondly, the image was divided along the mid-sagittal plane to delineate between the two hemispheres: tumour and background. These first two steps are shown in Figure 19 (Part A). The background volume was then flipped and overlaid onto the tumour volume so that a tumour/contralateral comparison could be made at the voxel level. Figure 19 (Part B) shows the resultant viable tumour volume. Voxels with a tumour/normal ratio of greater than 1.5 were considered viable tumour tissue. This ratio has been found to maximise sensitivity and specificity for defining viable tumour tissue (Herholz et al. 1998). Two subjects whose tumour affected tissue volume crossed the mid-sagittal plane were excluded from the study, as background normalisation using the tumour/background hemisphere technique was not possible.
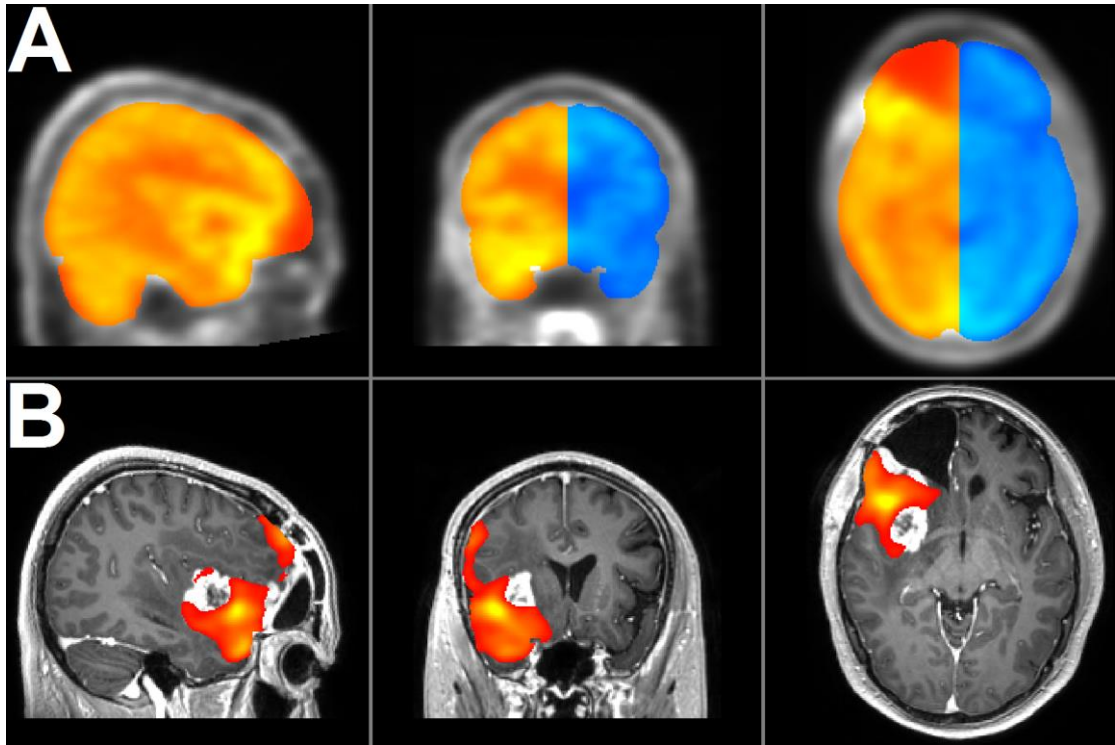
Figure 19, (Part A): Brain masking the PET images and dividing them into L and R hemispheres to allow for calculation of tumour to background uptake, (Part B): The resultant viable tumour mass, as seen on the 20 minute CMET scan.

The method used for defining viable tumour volume using the FLT-PET images was the same as for CMET, with one exception. Rather than the ratio, absolute difference in voxel numbers was used to compare FLT hemispheres. A ratio was not used for FLT as very low background uptake meant that the ratio could be significantly distorted by small variations in background SUV. The method used to find the optimal tumour/normal SUV difference for the FLT-PET images is outlined in Section 3.2.3.

A manual threshold was applied to each of the Gd-MRI images at a level that appeared to best separate areas of enhancement from background tissue. This threshold was not the same for all images as it was established on a case by case basis; the optimal threshold varied with inter-subject differences in signal intensity throughout the brain. The images were still masked with the MNI template to remove uptake that was external to the brain itself. As well as the MNI masking, a VOI mask was employed around the tumour region on the MRI images, to minimise inclusion of Gd enhancement that was not related to BBB disruption in the tumour region.

Figure 20 shows the viable tumour volume that was selected for a subject in the study using this technique.
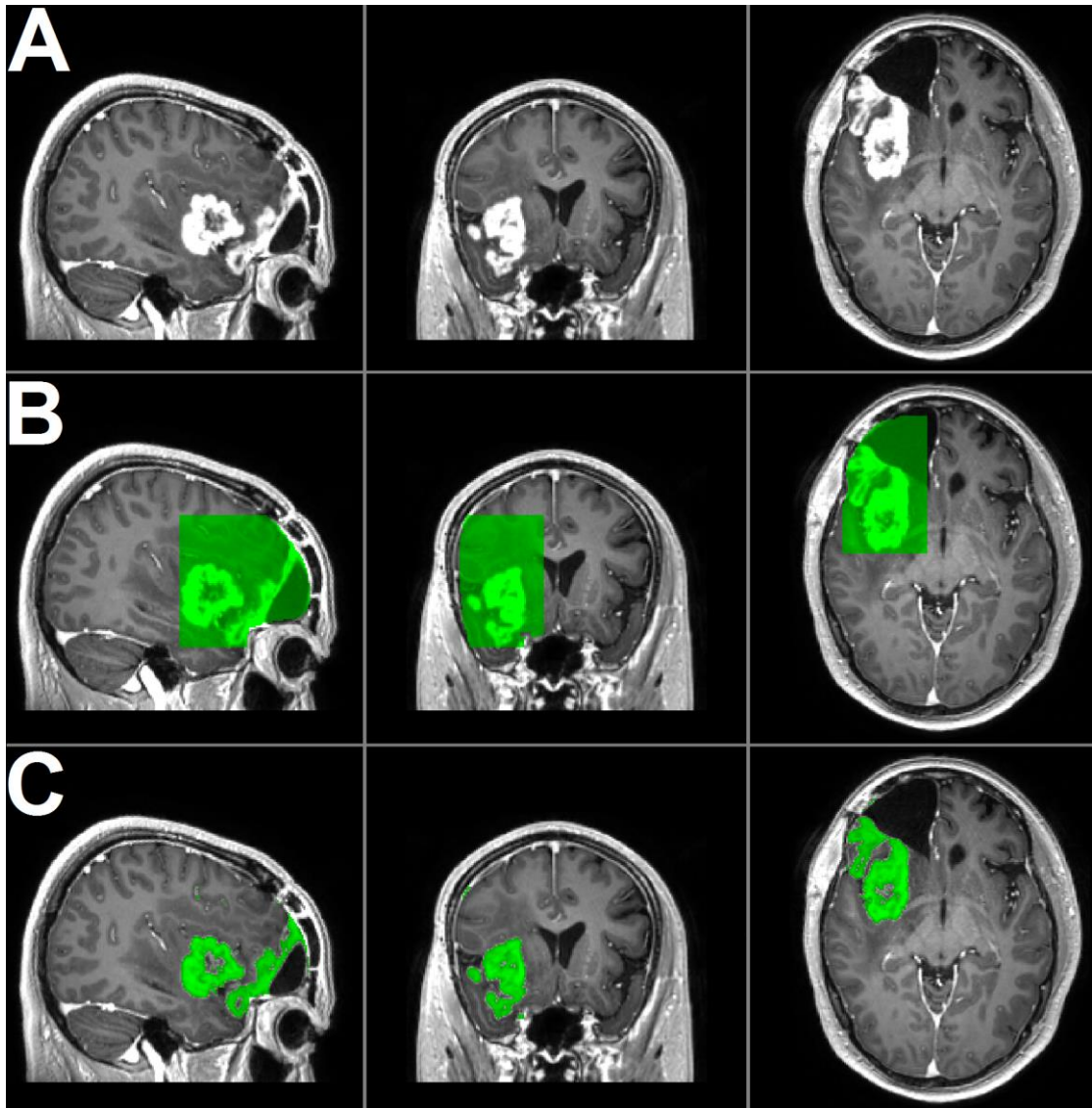
Figure 20, (Part A): A Gd enhanced T1-MRI taken from the study group, (Part B): The same image highlighting the volume used as a VOI mask drawn around the tumour region, (Part C): The green tissue was defined as viable tumour tissue using the manual thresholding technique.

3.2.3 Optimisation of Viable Tumour Volume Identification Threshold in FLT-PET

To determine the optimal tumour/background difference threshold to identify viable tumour volume for the FLT-PET images, receiver operating characteristic (ROC) curve analysis using survival at the median post-surgery survival time was employed.

A series of ROC curves were produced for tumour/background SUV difference thresholds between 0.1 and 0.7 for the FLT-PET images. Each ROC curve tested the effect that variation of the tumour volume cut-off between "small" and "large" had on the correlation between tumour size and survival at the median post-surgery survival time for the group (78 weeks). Censored subjects were included in the calculation of the median; their survival time was calculated as the time between their surgery and the present. They all survived longer than the median time, ensuring their inclusion would not affect the median value regardless of their actual survival time. The area under each ROC curve (AUC) was calculated and used to decide which absolute difference normalisation threshold was superior. Figure 21 in Section 3.3 is a graphical display of the ROC curves for each tumour/background SUV difference threshold. Table 1 in Section 3.3 shows the AUC values calculated for each threshold. For all ROC analyses, a true positive was defined as a subject that had a viable tumour volume larger than the cut-off, and who died earlier than the median survival time for the group.

The immediately aforementioned process was only necessary for FLT-PET. The tumour-background uptake ratio of 1.5 used to define viable tumour mass in CMET-PET was based on another study (Herholz et al. 1998), and the difference between enhancement and background volume in Gd-MRI was already clearly delineated (Figure 20).

3.2.4 Viable Tumour Volume Optimisation for Each Modality

An optimal cut-off volume for each modality to distinguish between subjects with a "large" or "small" viable tumour volume was established. This was achieved by ROC curve analysis, this time involving each modality. As in the previous comparison of ROC curves for the FLT-PET images, each of these were testing the effect that variation of the tumour volume cut-off between "large" and "small" would have on the correlation between tumour size and survival at the median post-surgery survival time for the group. The cut-off point was selected based on the point on the curve that minimised the Euclidean distance to the point at which both sensitivity (Se) and specificity (Sp) = 1. Figure 22 and Figure 23 in Section 3.3 show the

median survival ROC curves for CMET-PET and FLT-PET respectively. Figure 24 in Section 3.3 shows the median survival ROC curve for Gd-MRI; there were two points on the Gd-MRI curve that minimised the distance to the point at which both Se and Sp = 1.

Once the required thresholds were calculated, Kaplan Meier survival plots (Kaplan and Meier 1958) displayed the results graphically, and the Log Rank Test (Peto and Peto 1972) was used to quantify differences in survival times between the groups for each modality. Kaplan Meier survival plots and log rank tests were completed using the *R* packages *GGally* and *SurvDiff* (R Core Team 2015).

3.3   Results

3.3.1   Optimisation of Viable Tumour Volume Identification Threshold in FLT-PET

The ROC curves for all tested thresholds of tumour/background difference for the FLT-PET images during the optimisation process are presented in Figure 21. Table 1 lists the AUC values for each threshold. The tumour/background SUV difference threshold of 0.2 was used for the survival analysis as it had the highest AUC.
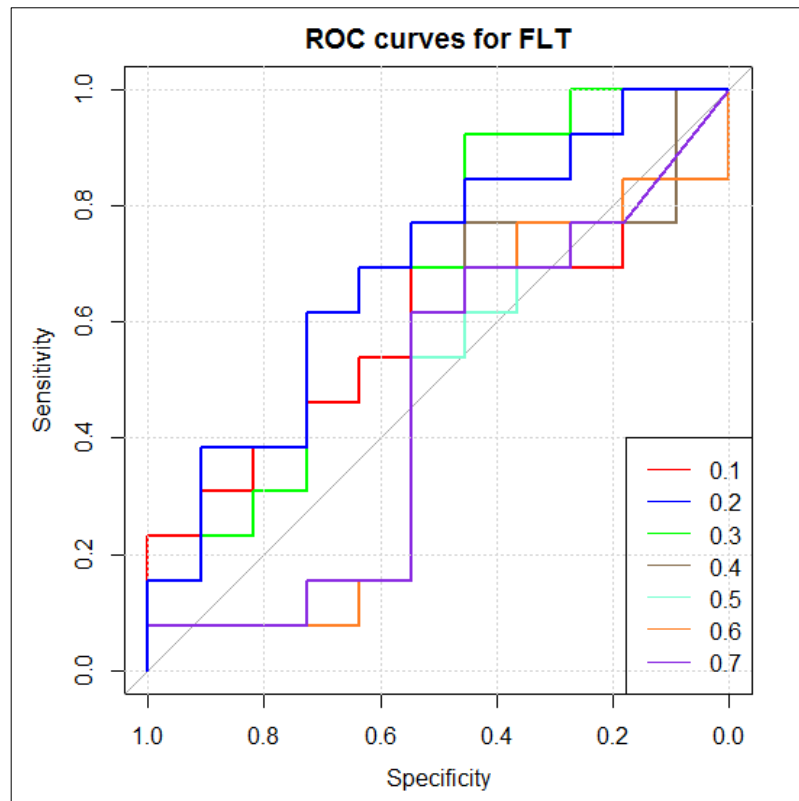
Figure 21, ROC curves for all FLT background normalisation thresholds between 0.1 and 0.7. Median group survival time was used as the status variable.

Threshold	0.1	0.2	0.3	0.4	0.5	0.6	0.7
AUC	0.594	0.693	0.685	0.468	0.441	0.454	0.461

Table 1, The AUC values calculated for each FLT background normalisation threshold ROC curve.

3.3.2 Viable Tumour Volume Optimisation for Each Modality

The ROC curves that illustrate the effect that variation of the tumour volume cut-off between "large" and "small" would have on the correlation between tumour size and survival at the median post-surgery survival time for the group are reflected in Figures 22-24. Each figure is labelled with the chosen cut-off point.
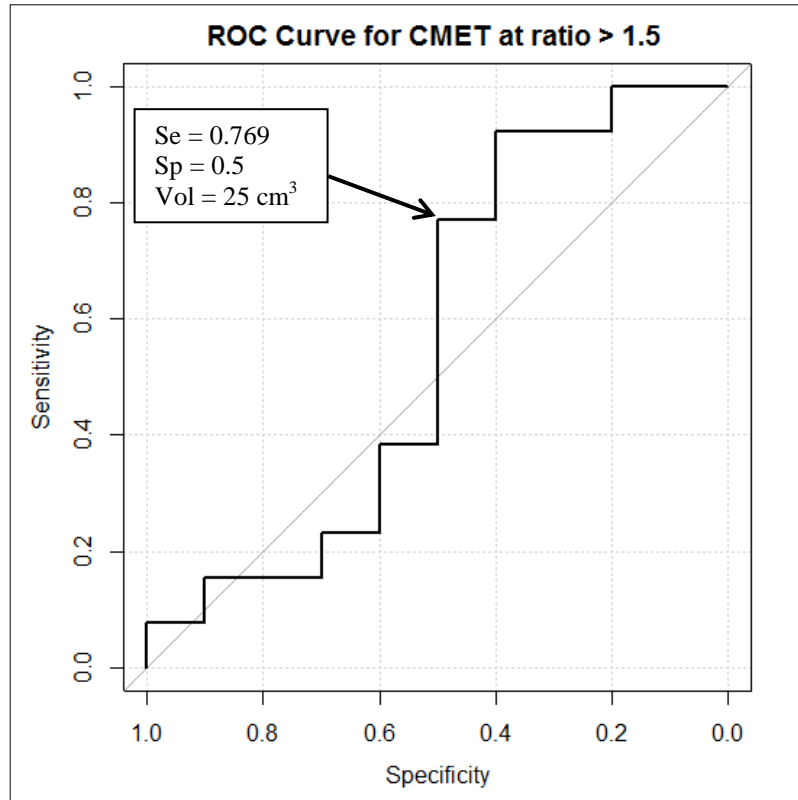
Figure 22, The median survival ROC curve for CMET-PET for tumour-background SUV ratio > 1.5, including the point on the curve that is closest to Sp and Se = 1.
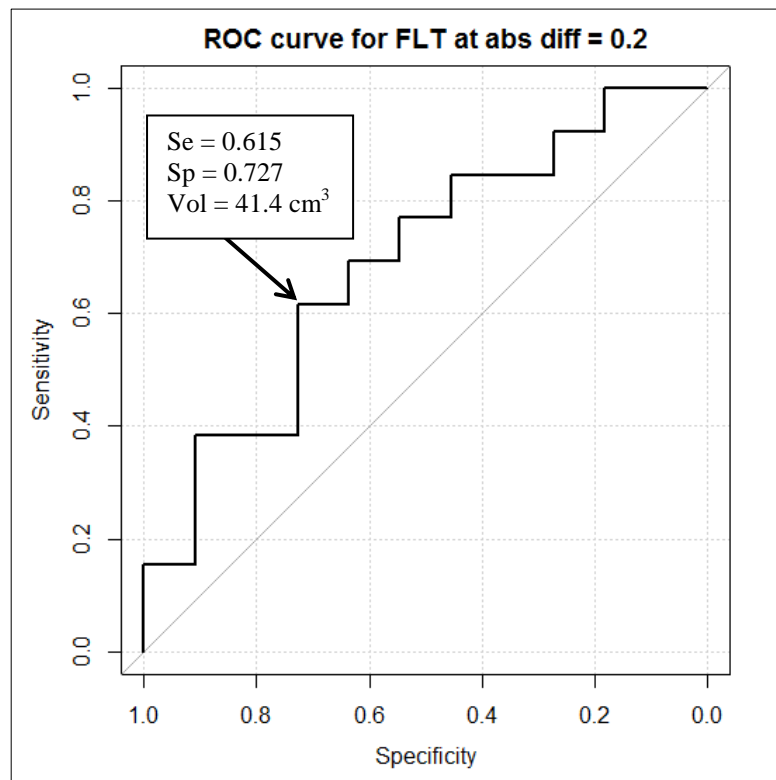
Figure 23, The median survival ROC curve for FLT-PET for tumour-background SUV absolute difference > 0.2, including the point on the curve that is closest to Sp and Se = 1.
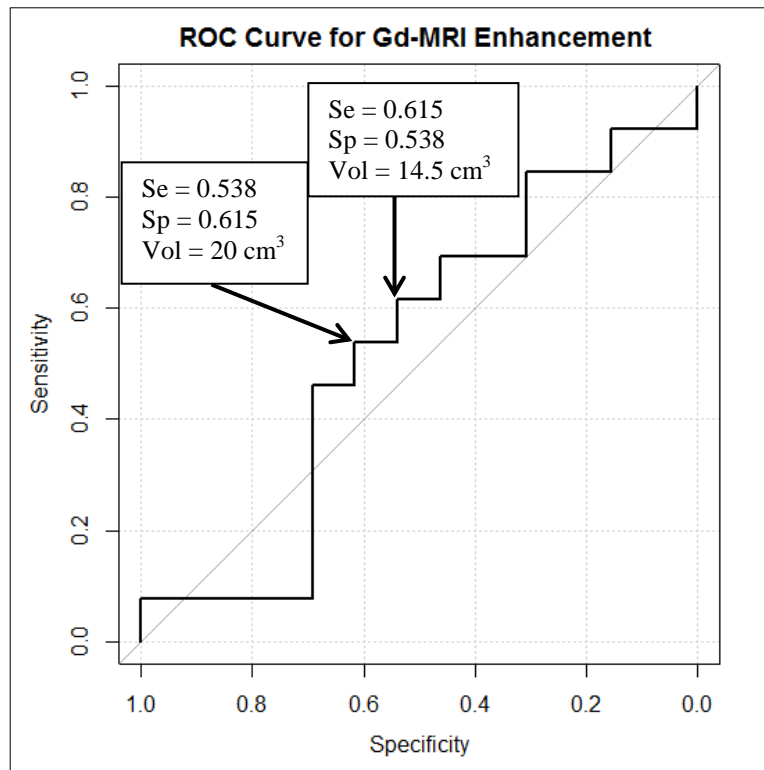
Figure 24, The median survival ROC curve for Gd-MRI enhancement, including the points on the curve that are closest to Sp and Se = 1.

3.3.3 Kaplan Meier Survival Plots and Results of the Log-Rank Test

Figures 25 and 26 present the Kaplan Meier plots for CMET-PET and FLT-PET, respectively. Two plots were produced for Gd-MRI, in accordance with the ROC analysis that showed two points on the curve that were equally well correlated with survival at the median survival time.
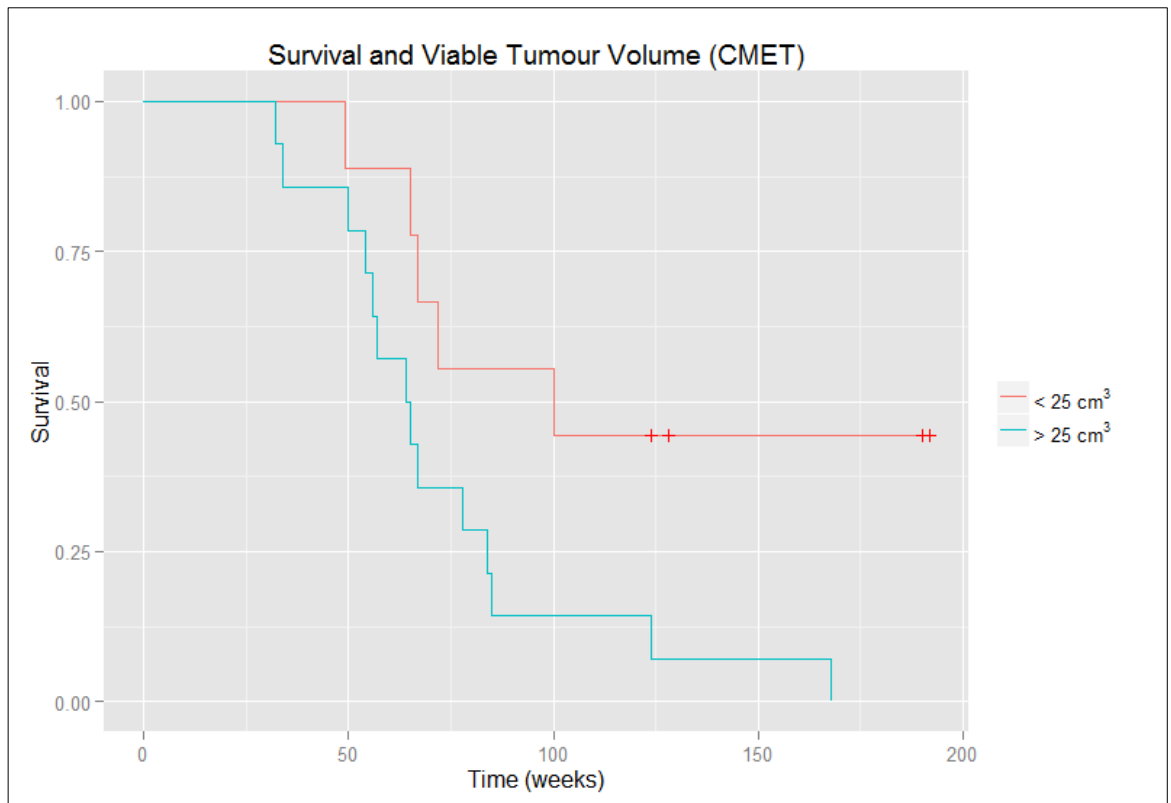
Figure 25, A Kaplan Meier survival plot for CMET-PET viable tumour volume, the delineation between 'small' and 'large' tumour mass was set at 25 cm³.
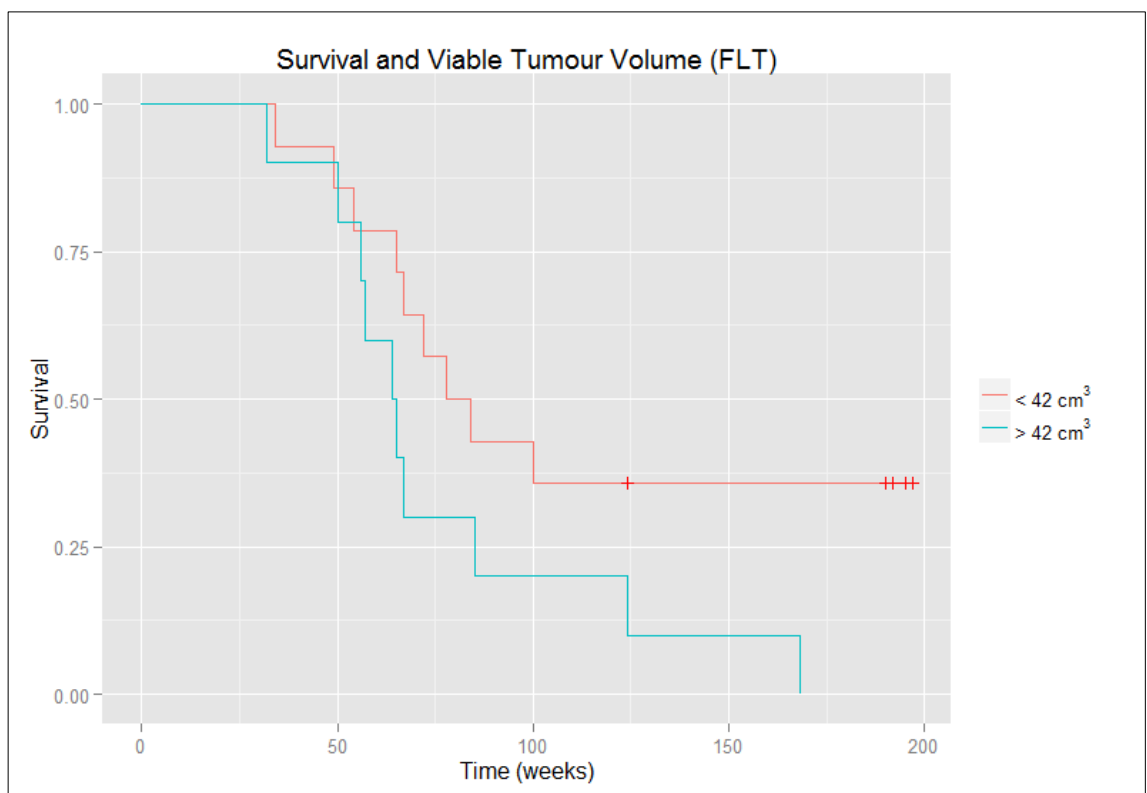
Figure 26, A Kaplan Meier survival plot for FLT-PET viable tumour volume, the delineation between 'small' and 'large' tumour mass was set at 41.4 cm³.
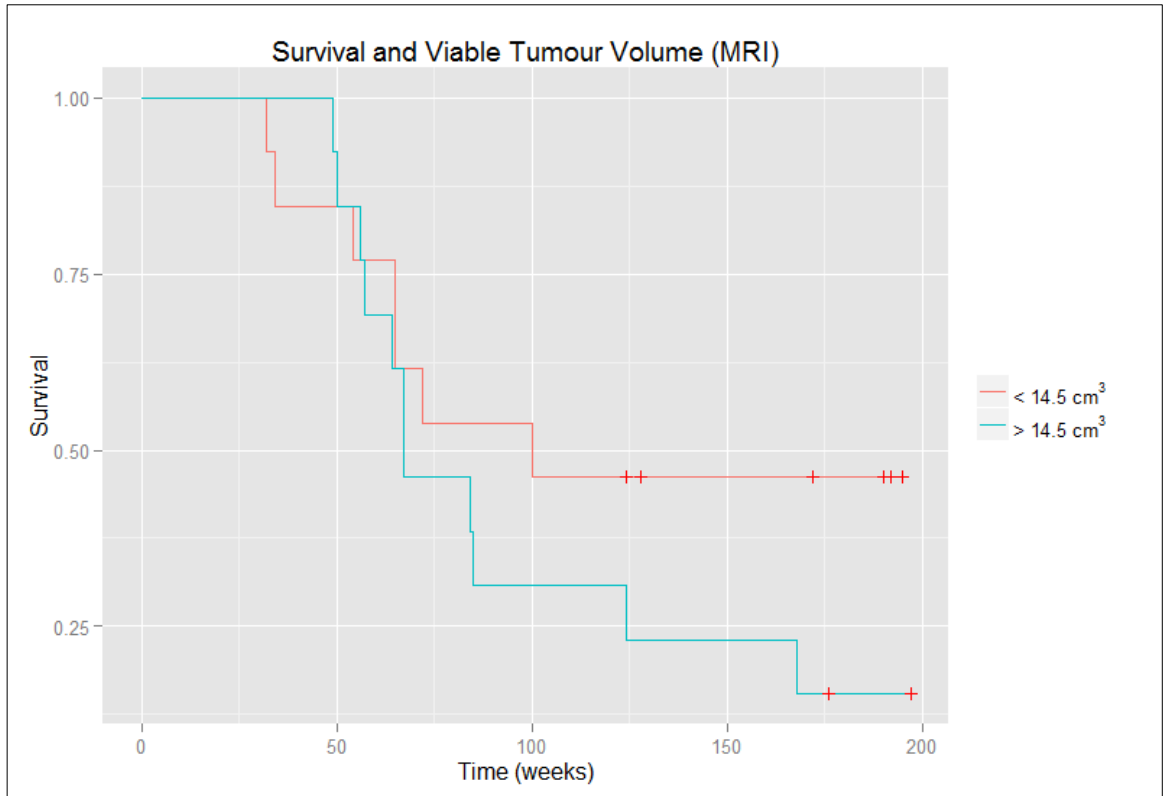
Figure 27, A Kaplan Meier survival plot for Gd-MRI enhancement volume, the delineation between 'small' and 'large' tumour mass was set at 14.5 cm³.
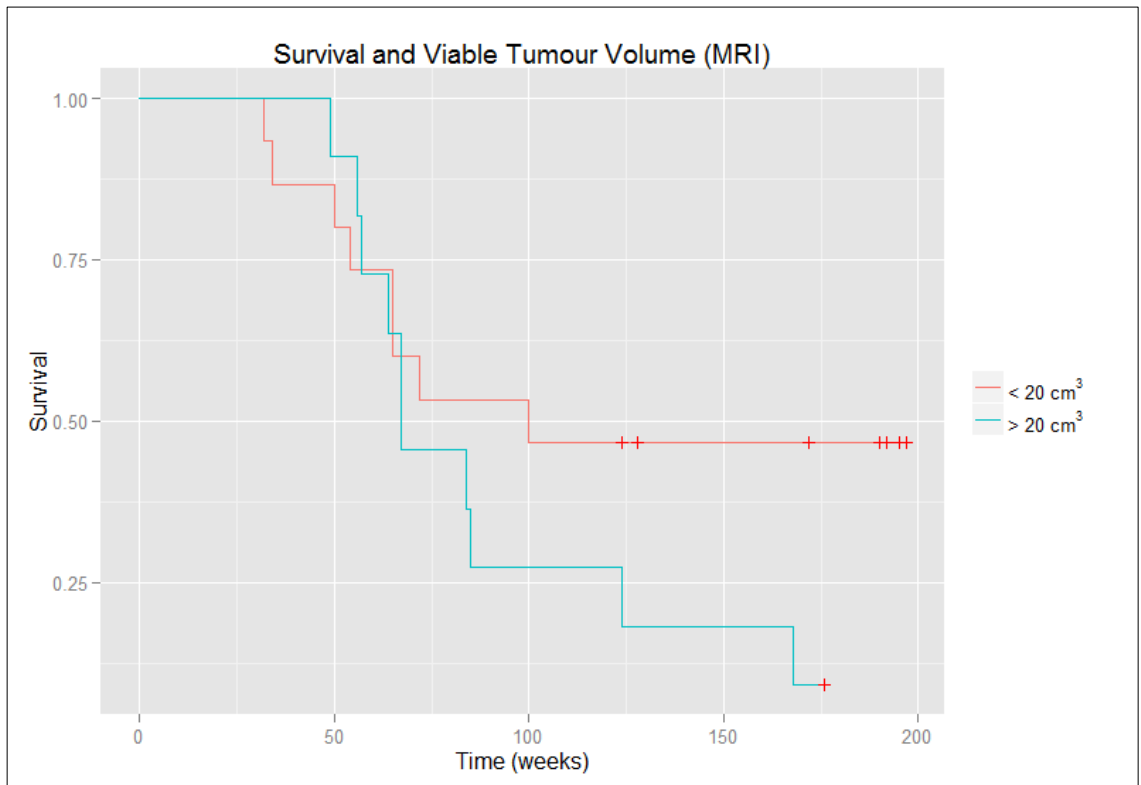
Figure 28, A Kaplan Meier survival plot for Gd-MRI enhancement volume, the delineation between 'small' and 'large' tumour mass was set at 20 cm³.

The Log-Rank test (Peto and Peto 1972) was used to determine statistical significance between the groups for each image type. Only CMET-PET produced a difference that was significant ($p < 0.05$). The results are summarised in Table 2.

Image type	CMET-PET	FLT-PET	Gd-MRI (14.5 cm3)	Gd-MRI (20 cm3)
p-value	0.021	0.066	0.227	0.163

Table 2, A summary of the results of the Log-Rank test performed on the survival data from each KM plot.

3.4 Discussion

Despite its widespread use in initial glioma diagnosis and therapy follow-up work, radiologic (primarily Gd-MR) imaging has been shown to have little utility in the differentiation of post-treatment tumour recurrence from treatment-related trauma and necrosis (Brandsma and van den Bent 2009). In order to improve the diagnostic accuracy of post-treatment glioma imaging, alternative modalities continue to be investigated in clinical research. Previous studies that pursued similar lines of investigative enquiry used longitudinal follow-up imaging as a means to assess treatment response via intra-subject changes in SUV, and used that as the factor which is analysed with regards to survival time (Herholz et al. (2003); Hoeben et al. (2013)). CMET PET has given superior outcomes to both FLT and Gd-MRI in previous studies attempting to predict survival outcomes in glioma (Singhal et al. (2012); Tripathi et al. (2012)). This study found that post-treatment tumour volumes on Gd-MRI and FLT-PET were not predictors of survival, in keeping with previous research. CMET-PET tumour volumes were found to be a statistically significant predictor of survival.

A potential pitfall in the ROC curve method used for threshold optimisation was highlighted during the Gd-MRI data analysis, with two points on the curve having identical distances to the top left hand corner of the plot (Figure 24). Since neither threshold was a significant predictor of survival, the issue was not pursued further. If, however, a decision had to be made regarding choice of threshold in such a scenario, one way of coming to a conclusion may be to change the way in which sensitivity and specificity are weighted. Studies concerned with cervical and breast cancer

diagnosis have found that that patients believe that sensitivity is the most important factor; that is, patients would rather be falsely diagnosed with cancer than falsely given a clean bill of health (Basen-Engquist et al. (2007); Schwartz et al. (2000)).

Achieving a high degree of accuracy when manually thresholding a high contrast tumour volume on Gd-MRI is made difficult by the fact there can be significant concentrations of Gd immediately outside the brain. Masking the image using the MNI brain mask template was performed to overcome this problem, but image co-registration is never perfect; there were occasions where a high contrast ring or crescent was seen at the outer edge of the brain as a result of small errors in the registration. As seen in Figure 20, a manual VOI was used to reduce the number of erroneous voxels included, but this could not always remove all extraneous high contrast voxels. Manual editing was not performed, as this would lead to reliance on the operator to decide where the uptake outside the brain ceased and the uptake inside the brain began; a proposition which is nearly impossible for tumours near the skull. A similar problem was noted for the PET images; a small error in the image alignment may result in a similar false inclusion of high relative uptake at the edge of the image. The fully automated nature of this analysis method is greatly advantageous with regards to its potential clinical applications. It is possible that individual tumour volumes may be identified with greater accuracy if each were manually edited to remove the previously mentioned artefacts. However, this would alter the very nature of the technique itself and greatly diminish its potential clinical utility. Manual modification of the tumour volumes may introduce inter-operator variability and human error into the method, as well as introducing the requirement for tedious and repetitive editing, thus it was not part of the investigation.

There were two subjects whose tumours crossed the mid-sagittal plane forcing their exclusion from the PET analysis due to the nature of the hemisphere based background normalisation; this was not an issue for the MRI contrast enhancement selection method.

3.5 Conclusion

Current radiologic imaging techniques continue to fail to adequately distinguish treatment-related tissue effects from tumour progression in glioma, leading to the requirement for other modalities and analysis methods to provide a solution. A semi-automated method was used to examine the utility of FLT-PET, CMET-PET and Gd-MRI for survival prediction based on viable tumour volume. CMET-PET was the only image type found to be a survival predictor.

4 Diagnostic Performance of Manual Versus Automated Hippocampal Masking in Alzheimer's Disease

4.1 Introduction and Literature Review

Reliance upon assessment of clinical symptoms alone in early AD diagnosis commonly results in diagnostic sensitivities and specificities of around 70%. Symptoms from conditions such as other dementias, depression, normal age-related neurodegeneration, and alcohol/drug use are frequently mistaken for AD in elderly patients (Blennow et al. 2015). It is hoped that the incorporation of imaging and biomarkers into clinical AD diagnosis can increase the rate at which a correct early diagnosis can be made.

There can be significant variation in the acuteness of AD pathology between sufferers; different areas within the cerebrum are also affected with varying severity. The medial temporal lobe is an area which is very severely affected by AD. In particular, the hippocampus stands out as a substructure that is one of the earliest affected brain regions (Nestor et al. 2004). Accurate assessment of hippocampal tissue effects can potentially become a useful biomarker for clinical AD assessment.

Large scale atrophy throughout the cerebral cortex can be clearly seen in vivo using structural MRI, as well as atrophy of some small structures such as the hippocampus (Apostolova et al. 2012). Corresponding reductions in regional glucose metabolism (MRglc) in large cortical volumes have been identified by studies using automated voxel based analysis (VBA) on FDG-PET images; however, these studies almost never find the expected reduction in hippocampal MRglc (Mosconi et al. 2005). This inability to detect reduced hippocampal MRglc is possibly due to the small volume of the hippocampus and the errors inherent in the spatial registration of comparatively low resolution PET images to an anatomical template. Manual ROI sampling, guided by coregistered MRI, has proven more effective at detecting reduced hippocampal MRglc. This method, though effective, has several drawbacks. Marking out manual ROIs of the hippocampus for an individual is laborious, and can only be reliably performed by someone with thorough knowledge of neuroanatomy.

Furthermore, patients are rarely given a volumetric MRI in a clinical setting. An optimised mask created using manually marked hippocampal peripheries on T1 MRIs has been shown to be accurate in defining the hippocampus on spatially normalised FDG-PET images, and for detecting reductions in hippocampal MRglc in patients with Mild Cognitive Impairment (MCI) and Alzheimer's disease (AD) (Mosconi et al. 2005).

Some brain image processing programs such as *FSL* (Smith et al. 2004) feature a routine that can automatically segment cortical and subcortical structures within a volumetric T1 MR image, potentially circumventing the requirement for manual ROI marking in the analysis of brain substructures. The use of a fully automated hippocampal masking algorithm increases the ease with which very large data sets can be analysed, enabling the diagnostic capability of the method to be evaluated with greater statistical power. Furthermore, refinement and improvement of the mask as image technology improves can be conducted much more easily if repeated manual marking is not required.

The study by Mosconi and colleagues (2005) demonstrated the utility of an optimised hippocampal mask, created by expert observers manually marking the hippocampus on 48 MRI studies, in identifying changes in hippocampal MRglc during the onset and development of AD. This Chapter compares the performance of a manually defined hippocampal mask with one that was formulated using an automated algorithm. An automated masking method allows for increased numbers of subjects to be included in the mask itself, and for easier redevelopment and refinement of the mask in the future. The two masks are then compared with regards to their capacity to differentiate between groups of AD, MCI and healthy control (HC) subjects.

4.2 Materials and Methods

4.2.1 Image Cohort

Images for this research were obtained from two different sources. 21 (7 AD, 7 MCI and 7 HC) Volumetric T1 brain MRIs from the CSIRO's Australian Imaging, Biomarkers & Lifestyle Flagship Study of Ageing (AIBL, http://aibl.csiro.au/) (Ellis et al. 2009) were used for the creation of the manual hippocampal mask. AIBL MR images were collected using 1.5 T scanners and acquired in the sagittal plane as 1.2 mm thick contiguous slices. The pixel size and slice thickness was 1.2 mm and the image matrix size was 256 x 240 pixels. These images were used for manual mask generation.

A further 190 (51 AD, 66 MCI and 73 HC) subjects were selected from the Alzheimer's Disease Neuroimaging Initiative online database (ADNI, http://www.adni-info.org/Home.aspx) (Mueller et al. 2005). These subjects had both volumetric T1 MRI and FDG-PET images taken. For inclusion in this analysis, images from the ADNI cohort were only considered if their volumetric T1 MRI and FDG-PET scans were taken no more than three months apart. ADNI MR images were 1.5 T, acquired in the sagittal plane as contiguous slices, pixel size 1.25 x 1.25 mm, slice thickness 1.2 mm, matrix size 192 x 192 pixels. ADNI PET images were acquired in the axial plane, with a dynamic emission scan of six five-minute frames beginning 30 minutes post injection; images were reconstructed into a 128 x 128 matrix with a 2 mm slice thickness and pixel size.

All images were obtained in DICOM format. To enable spatial registration and automated hippocampal marking using *FSL* (Smith et al. 2004), images were converted to *FSL nifti* format using the *FreeSurfer* (Martinos Centre for Biomedical Imaging, http://surfer.nmr.mgh.harvard.edu/) routine *mri_convert*.

4.2.2 Hippocampal Mask Generation

4.2.2.1 Manual Hippocampal Marking

All 21 subjects (7 from each diagnostic category) drawn from the AIBL database comprised the manual masking cohort. *ImageJ* (RSB, National Institute of Mental Health) (Schneider et al. 2012) was used to facilitate the digital marking of the MRIs, which is depicted in Figure 29. The marking was conducted by a neuroradiology registrar at Royal Perth Hospital as follows:

"Coronal MRI T1-MPRAGE 1mm thick slices were obtained for each patient perpendicular to the long axis of the hippocampus, which was used to individually draw regions of interest of both hippocampi. The neuroimaging specialists who performed this were blinded to the clinical status of each patient. Mapping commencing at the pes-hippocampus anteriorly was performed on every second slice over a twenty-slice volume for a total of 10 hippocampal measurements per mesial temporal lobe. The lateral hippocampal border was defined as the temporal horn of the lateral ventricle, the medial border as the ambient cistern, and the inferior border as the white matter of the parahippocampal gyrus." (A. Law, Consultant Nuclear Medicine Physician, personal communication November 24, 2011).
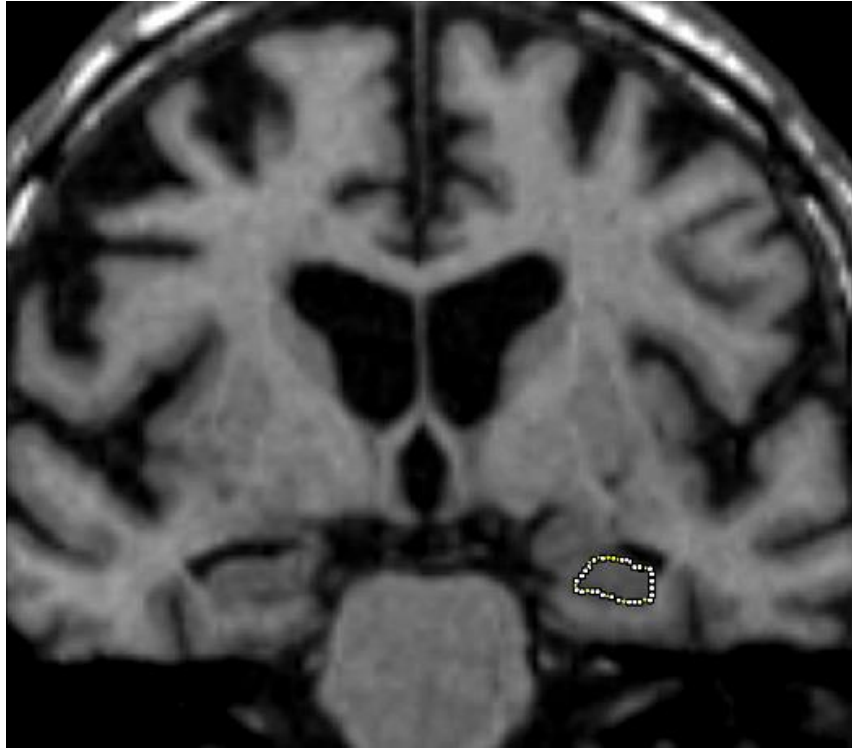
Figure 29, A coronal outline of the hippocampus in the left hemisphere, made using the manual marking technique in ImageJ (RSB, National Institute of Mental Health).

Manual marking was performed on every second coronal slice. However, a contiguous volume is required to delineate the whole hippocampus. In order to construct a contiguous volume from the marked coronal slices, the images were first re-sliced and viewed in the sagittal plane. A single iteration of the binary processing 'dilate' and 'erode' functions built in to *ImageJ* was then used to form a contiguous volume. The dilate function works by assigning a value of 1 to every 0 value voxel that sits adjacent to a '1' voxel. This has the effect of filling in small holes or spaces in a volume as well as expanding its outer perimeter. The erode function performs the opposite operation. The net effect is that small holes or spaces within a volume are filled in with minimal impact on the original outer perimeter. Figure 30 (Part A) shows the marked non-contiguous hippocampal slices and the contiguous volume formed after the implementation of the dilate and erode functions (Part B).
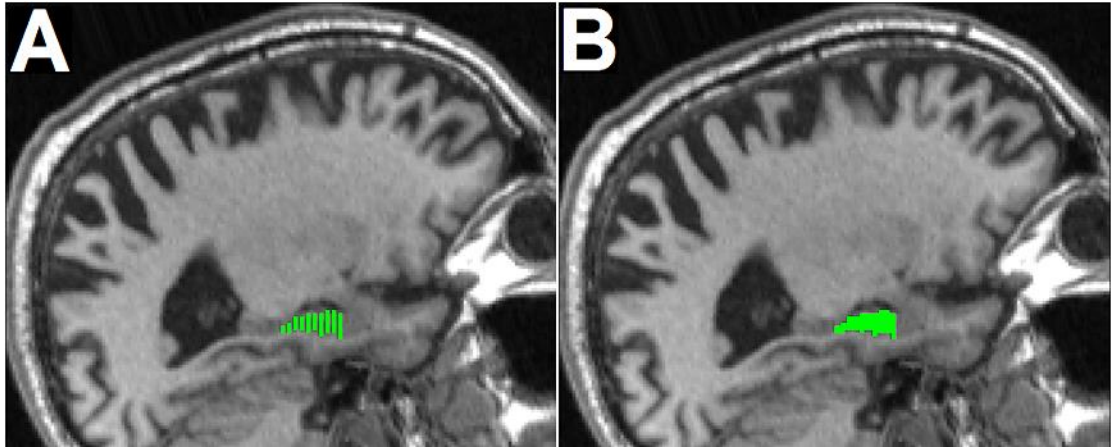
Figure 30, (Part A): Manually marked coronal hippocampal sections, viewed in the sagittal plane, (Part B): The continuous hippocampal volume formed by using the 'dilate' and 'erode' functions in ImageJ.

4.2.2.2   Automated Hippocampal Marking

100 subjects (21 AD, 26 MCI and 43 HC) were randomly selected from the ADNI cohort to form the automated mask. The *FSL* (Smith et al. 2004) subroutine *FIRST* (Patenaude et al. 2011) was used to automatically segment out the hippocampus on all subject MRIs from the ADNI database. The volume used to define the hippocampus on a subject MRI using *FIRST* can be seen in Figure 31. *FIRST* incorporates data obtained from manually labelled image sets to assist in forming an initial estimation of the spatial location of the subcortical structures to be segmented. A deformable virtual surface mesh for each structure was then calculated and optimised to form the substructure boundaries (Patenaude et al. 2011).
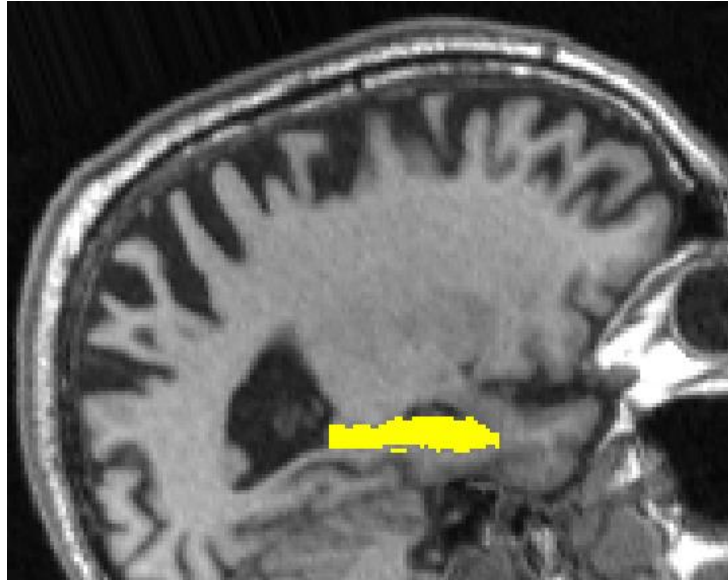
Figure 31, A sagittal view of a subject's hippocampal volume, defined by FIRST.

4.2.2.3 Montreal Neurological Institute Template Coregistration

Nonlinear warping was used to spatially coregister all subject MRIs to the McConnell Brain Imaging Centre (Montreal Neurological Institute (MNI), McGill University Montreal) 152 nonlinear 6th generation T1 2mm resolution brain template via a multi-stage process. The *FSL* (Smith et al. 2004) routine *BET* (Smith 2002) was used to strip the skull from around the brain volume. An approximate template alignment was then achieved using the *FSL* routine *FLIRT* (Jenkinson et al. 2002) to calculate a 12 degree of freedom affine transformation to the MNI brain template. The affine transformation was used to assist in the calculation of nonlinear warps, which were used to give a more precise template registration. The *FSL* routine *FNIRT* (Andersson et al. 2007) was used to calculate the nonlinear subject MRI-MNI template warps. Figure 32 illustrates the MRI spatial registration process.
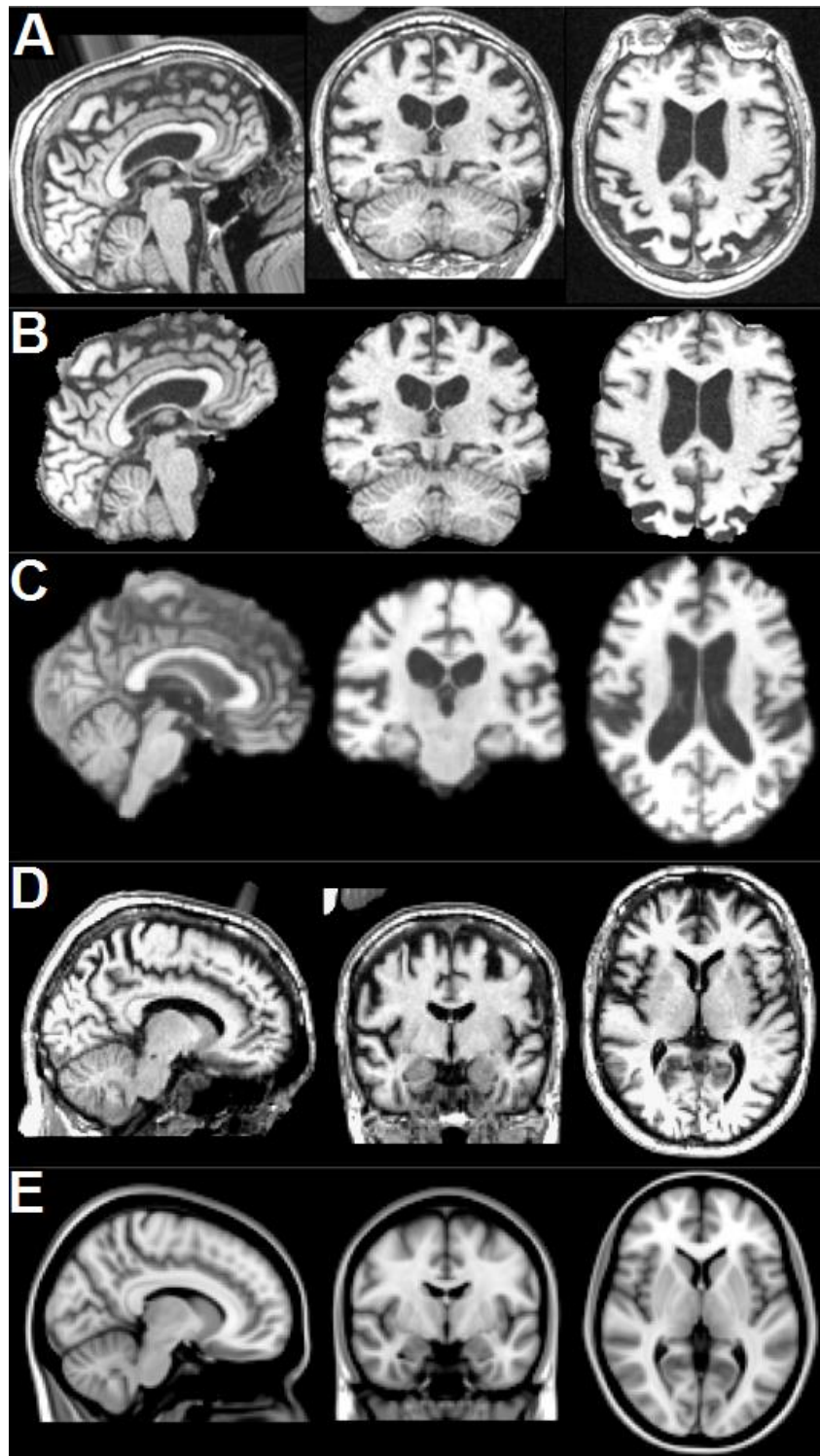
Figure 32, (Part A): A native space subject MRI, (Part B): The MRI after skull extraction using BET, (Part C): The MRI after affine brain template registration using FLIRT, (Part D): The MRI after nonlinear spatial warping to the T1 MNI template using FNIRT, (Part E): The T1 MNI template.

FIRST segmentation (Patenaude et al. 2011) marks a subject's hippocampal volumes in the subject's native image space; this allows for a subject's MRI-MNI warp to be applied to the hippocampal volume to provide an MNI template space

transformation. Figure 33 illustrates the location of a subject's hippocampus after transformation to the MNI template.
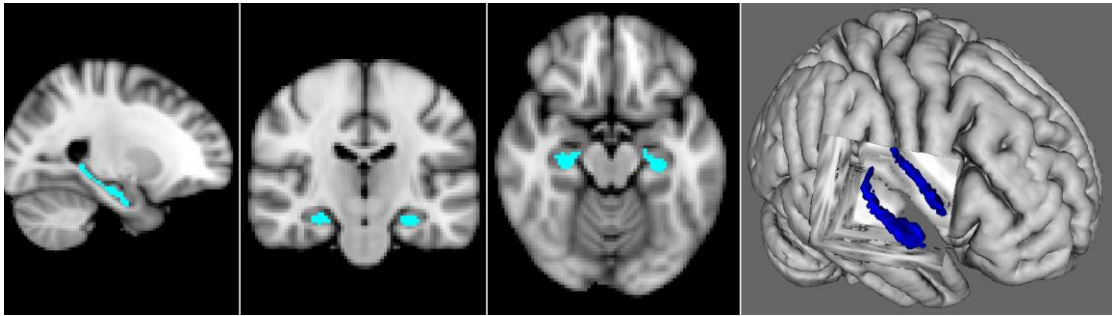
Figure 33, The location of a subject's FSL (Smith et al. 2004) marked hippocampus in MNI space after nonlinear warping to the MNI template.

4.2.2.4 Hippocampal Mask Optimisation

Once the hippocampal volume for each subject had been spatially warped to MNI space, a summation volume across all subjects in a cohort was created that showed the degree of hippocampal overlap at each voxel. The summation volumes for the manual and automated *FSL* (Smith et al. 2004) masks are shown respectively in Figure 34, Parts A and B. The process used to develop and optimise both masks draws upon the work of Mosconi and colleagues (2005).
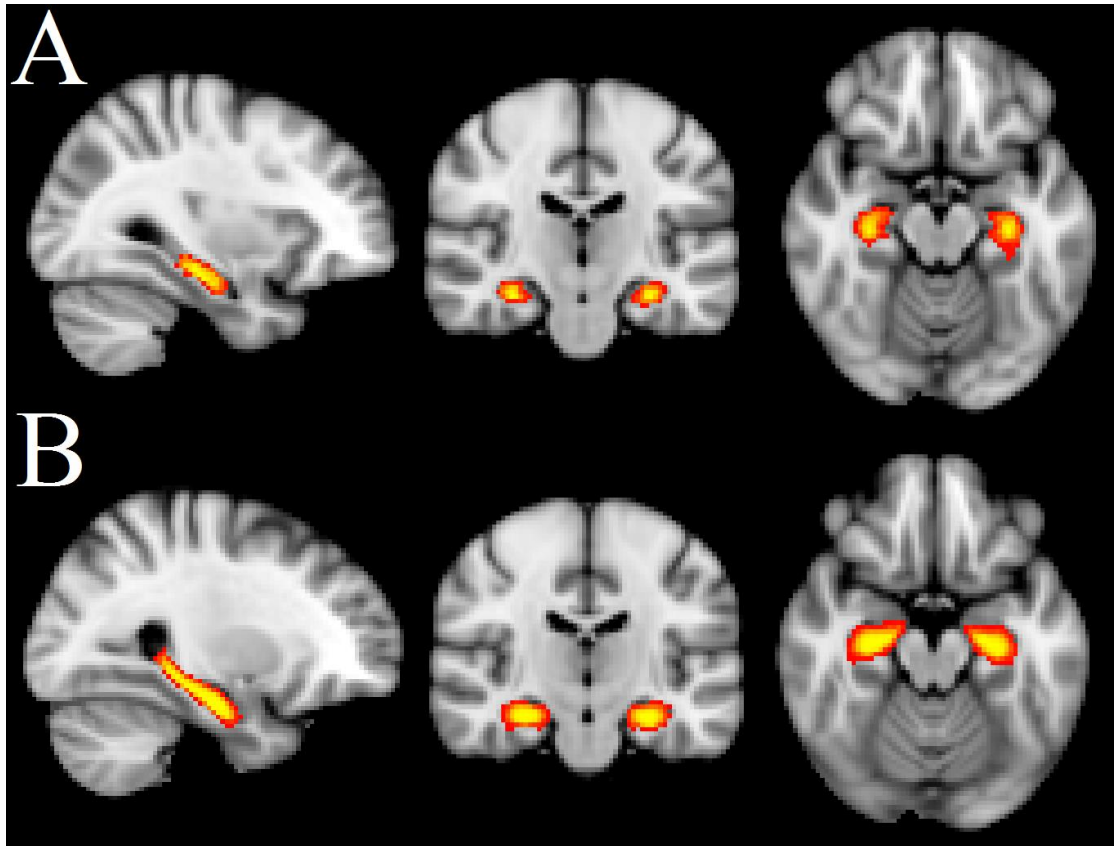
Figure 34, (Part A): The summation volumes displaying the MNI space location of all hippocampal volumes for the manual markings, (Part B): The automated FSL (Smith et al. 2004) markings. The heat map corresponds to the degree of overlap at each voxel.

It was critical to avoid incorrectly sampling non-hippocampal tissue within the mask. In other words, the maximisation of true positives (voxels included in the mask that are within the hippocampus for a given subject) was more important than the minimisation of false negatives (voxels that are not included in the mask but are within the hippocampus for a given subject).

If this was the only consideration to be taken into account, then mask optimisation would be as simple as only sampling those voxels in MNI space that were shared between all subjects' hippocampal volumes. However, as is discussed in Mosconi and colleagues (2005), the inter-subject variability in hippocampal anatomy means that increasing the sample size from which a mask is formulated will likely lead to a decrease in the number of voxels that are shared between all subjects. The use of such a small volume means that when applying the mask to a large set of subjects, the average counts sampled in an individual subject is highly susceptible to the inclusion of only a very small number of non-hippocampal voxels.

Resampling statistics, in particular the bootstrap, can be used to simulate how a mask volume might vary if a very large number of subjects were sampled. The Bias-Corrected and Accelerated Percentile (BCa) method of bootstrapping (Efron and Tibshirani 1993) was used to assess mask volumes by degree of overlap, in order to assess the theoretical stability of the masks' volume if they were drawn from very large sample sizes. The bootstrapping procedure is outlined in Appendix 3. The largest volume stable mask was selected as the optimal mask.

4.2.3 Quantification of Hippocampal MRglc

The FDG-PET images of the 90 ADNI database subjects who were not used for the automatic mask generation (30 HC, 30 MCI and 30 AD) were used to compare the performance of the manual and automatic masks.

The ADNI imaging protocol for FDG-PET brain images is a "dynamic 3D scan consisting of six-5 minute frames" with acquisition commencing 30 minutes post-injection (ADNI 2006, p 11). The normal FDG-PET acquisition protocol at our institution is for a single frame 30 minute acquisition; an equivalent image set was generated from the ADNI PET for each subject as follows.

The *FSL* (Smith et al. 2004) routine *mcflirt* (Jenkinson et al. 2002) was used to perform rigid body intra-subject co-registration of the dynamic image sequence to the first frame of the sequence, removing the effect of any patient movement between the frames. The 6 co-registered images were then averaged to form a single FDG-PET image volume for each subject in the cohort. This average image was used for all further processing.

Intrasubject (MRI – PET) image alignment for the ADNI images was performed via a six degree of freedom transformation (rigid body) using the *FSL* (Smith et al. 2004) routine *FLIRT* (Jenkinson et al. 2002). Once a subject's PET was aligned with their MRI, the nonlinear MRI-MNI warps calculated during the automatic hippocampal mask development were then applied to transform the PET images to the MNI template space. This process is depicted in Figure 35.
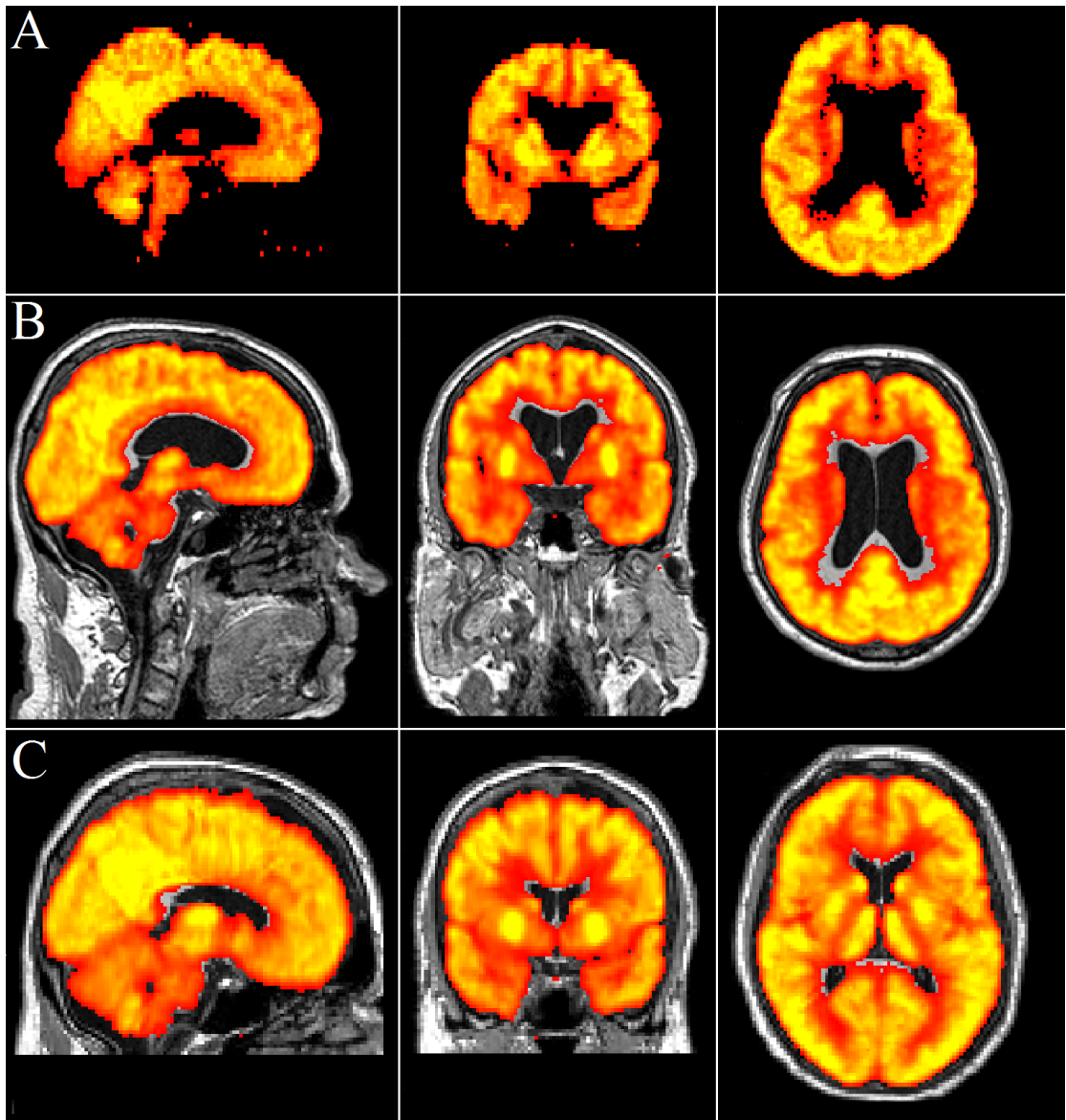
Figure 35, (Part A): A subject FDG-PET volume in its native space, (Part B): The subject PET and MRI volumes after intra-subject MRI co-registration, (Part C): The subject PET and MRI volumes after nonlinear spatial registration with the MNI template.

Differences in inter-subject FDG uptake and inter-scanner sensitivity differences were accounted for by scaling each PET voxel using the average uptake in the pons, as pons metabolism is relatively unaffected in AD (Minoshima et al. 1995). A pons VOI was constructed such that its borders sat within the boundaries of the pons on the 2mm T1 MRI MNI template, to minimise the chances of erroneously including extra-pontine tissue on a PET image due to spatial normalisation errors. Figure 36 depicts this volume, which was defined by using an *ImageJ* macro (included in Appendix 4) to outline a series of transaxial polygonal ROIs that fell within the pons. The volume of the pons VOI was 1.6 cm^3. This volume was used to select the pons

on PET images that had been spatially warped to template space. Pons normalisation was achieved by applying a scaling factor to an image volume so that the average voxel number inside the pons VOI was 10000.
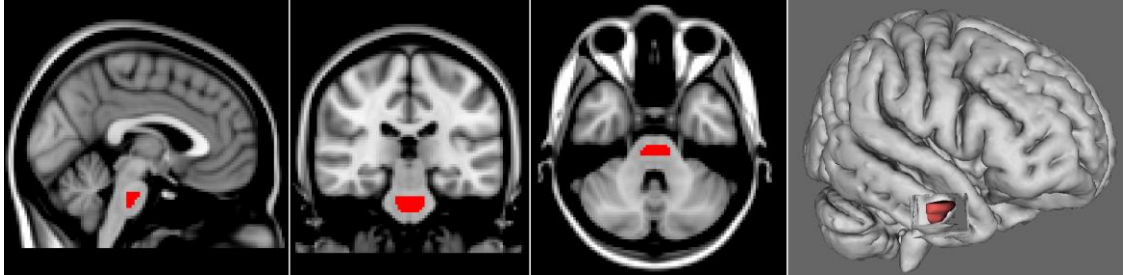
Figure 36, The VOI used to represent the pons for scaling of a subject's FDG-PET images.

After pons normalisation, an ImageJ macro was used to determine the average normalised hippocampal metabolism for each of the remaining 90 subjects from the ADNI database (30 HC, 30 MCI and 30 AD) using both hippocampal masks. This macro is included in Appendix 5.

4.3 Results

4.3.1 Mask Optimisation and Bootstrapping

If the hippocampal marking and spatial normalisation procedures were both perfect, then the degree of overlap at every hippocampal voxel in the summation volumes shown in Figure 34 would be 100%. However, only seven voxels (56 mm^3) from the manually marked data and 27 voxels (216 mm^3) from the *FSL* (Smith et al. 2004) automated data were common to all subjects.

It was found that the smallest (100% overlap voxels only) masks for both the manual and automated masks were unstable; that is, they fell outside the 95% BCa confidence limit (Efron and Tibshirani 1993) (further details regarding the bootstrapping calculations can be found in Appendix 3). Therefore, the automated and manual mask volumes included the voxels that were shared between 99 or more of 100 (99%) subjects in the *FSL* (Smith et al. 2004) cohort, and 20 or more of 21 subjects (95%) in the manually marked cohort as these were the smallest masks that

fell within the 95% BCa confidence limit. The size of these masks were 68 voxels (544 mm^3) and 21 voxels (168 mm^3) for the automated and manual masks respectively.

4.3.2 Quantification of Hippocampal MRglc Using the Masks

A comparison of the averaged pons normalised MRglc within each of the masks, displaying differences between each diagnostic category, is shown in Figure 37.
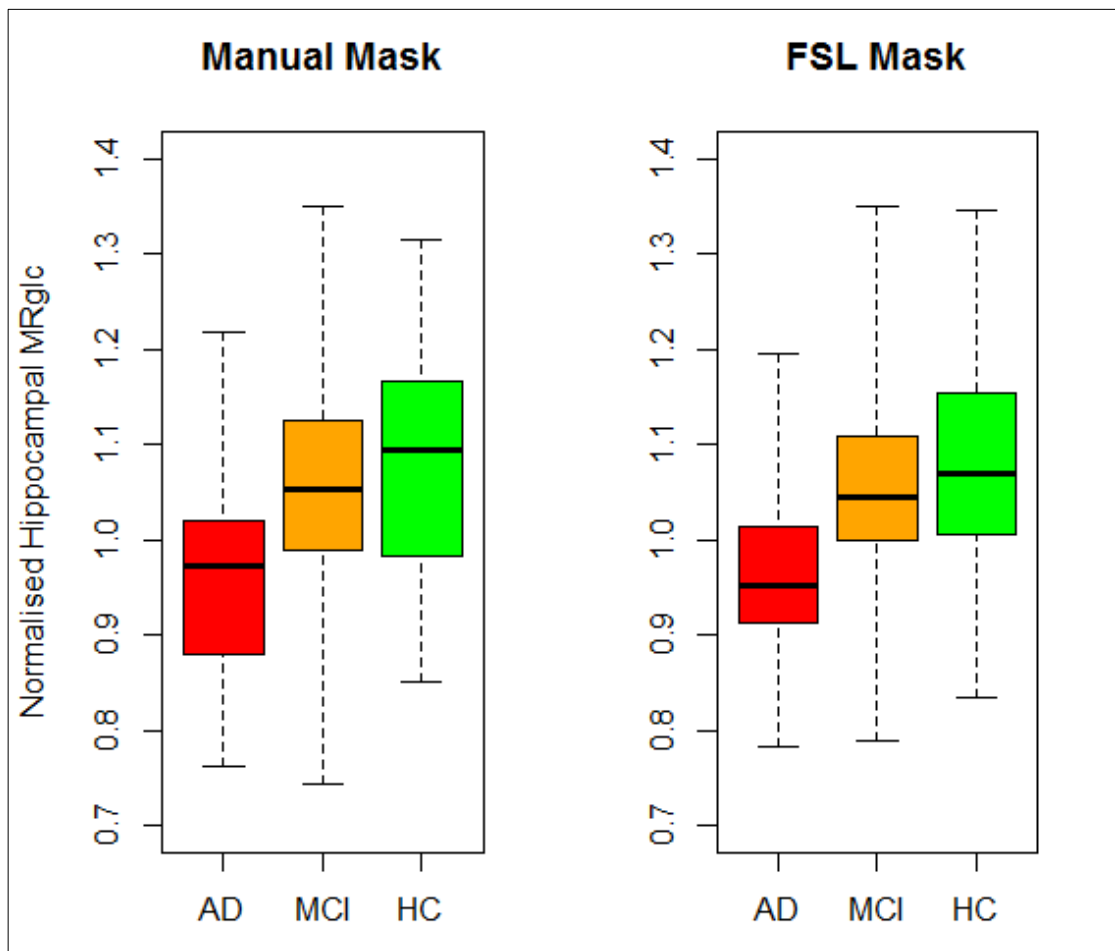
Figure 37, Boxplots showing the group level differences between diagnostic category for both the manually marked and FSL (Smith et al. 2004) hippocampus masks.

	p-values	
Groups	Manual Mask	FSL Mask
AD-MCI	< .005	< .005
AD-HC	< .0005	< .0005
MCI-HC	>.05	>.05

Table 3, The significance (Tukey's HSD) of differences in normalised hippocampal MRglc between AD, MCI and HC groups for both manual and FSL (Smith et al. 2004) masks.

Group level differences in the pons normalised masks counts were investigated using Tukey's HSD Test, which were calculated using the statistics package *R*. No significant difference between the MCI and HC groups were found for either mask ($p > 0.05$). However, differences between the AD-HC and AD-MCI groups for both masks were significant at the 0.0005 and 0.005 levels respectively. Figure 38 illustrates the correlation in MRglc measured using the two different masks for each individual. A high degree of correlation was found ($r = 0.96$, $p < 0.0001$ using Pearson's product moment correlation in R). These results show that the performance of the masks is equal at both the individual and group level.
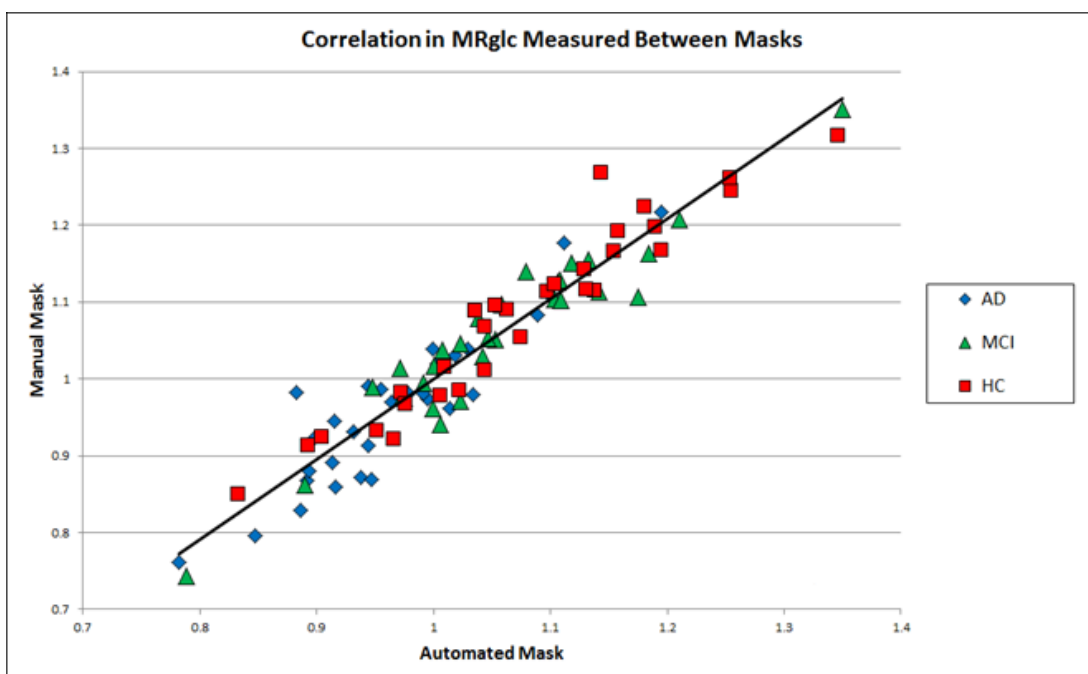
Figure 38, A graphical representation of the degree of correlation between MRglc levels measured in each individual between the automated and manual hippocampus masks.

4.4 Discussion

Quantification of neurodegeneration due to AD without the use of imaging involves significant confounding factors, which include the potential influence of other conditions and difficulties in establishing a baseline for expected cognitive performance. Brain imaging allows for better understanding of patterns of degeneration that are AD-specific, some of which become evident before the onset of clinical symptoms. FDG-PET is a widely available imaging modality that has demonstrated utility in research settings in identifying patterns of neurodegeneration that can be specifically attributed to AD (McKhann et al. 2011).

A study by Mosconi and colleagues (2005) that used a manually defined mask of the anterior portion of the hippocampus known as the head or "pes" (see Figure 10), found significant MRglc differences between groups of AD and HC brains, as well as HC and MCI brains, but not between MCI and AD. The results from that study are different to this study with regards to the relative MRglc seen in the MCI group. This research found there to be no significant difference in MRglc between the MCI and HC groups, and a significant difference between the AD and MCI groups.

There can be differences in the manner in which MCI is defined between studies. For a subject to be diagnosed with MCI in the Mosconi and colleagues (2005) study, they needed to have a Mini Mental State Examination (MMSE) score of > 24, and a Global Deterioration Scale (GDS) (Reisberg et al. 1982) score of 3. Likewise, to be considered MCI by ADNI, subjects needed an MMSE score of > 24. However, they also needed to have a memory complaint, and objective memory loss measured by education adjusted scores on the Wechsler Memory Scale Logical Memory II (Wechsler 1987), as well as a Clinical Dementia Rating (CDR) (Morris 1993) of 0.5 (ADNI 2008). To be diagnosed as MCI by the Australian Imaging, Biomarkers and Lifestyle (AIBL) study, a participant must have reported memory difficulties (either directly or through an informant). If the subject had already been clinically diagnosed as MCI before entering the AIBL study, they were required to demonstrate a score that was 1.5 or more standard deviations below the age-adjusted mean on at least one neuropsychological task to be considered MCI by AIBL. Monthly clinical review

panel meetings were held, during which study participants who entered the study as HC participants could be re-diagnosed as MCI. In order for this to happen, they had to score at least 1.5 standard deviations below the age-adjusted mean in two or more cognitive tests (Ellis et al. 2009). The fact that different studies take varying approaches to the diagnosis of MCI is indicative of the level of uncertainty surrounding the condition itself. The difference in diagnostic criteria identified between the Mosconi and colleagues (2005) study and the ADNI study probably had an effect on the overall distribution of MCI MRglc rates measured in this research.

The process of manual hippocampal marking can be extremely resource intensive and time consuming, and requires expert observers. Establishing a large manually marked cohort of brain images would be very difficult for this reason, and the manual marking protocol used in this research was adjusted to try and save time for the neuroradiology registrar performing the marking. Only every second coronal slice was marked starting at the anterior hippocampal boundary, this method was considered sufficient due to the regular shape of the hippocampus along the anterior-posterior direction (Figure 11). Only ten slices were marked in total, which meant that the anterior 20 mm portion of each hippocampus was included in the manual mask. This marking length is in line with previous studies employing manual hippocampal segmentation and spatial warping, which found that superior diagnostic accuracy was achieved for the larger anterior portion of the hippocampus, and that use of the smaller tail section led to increased registration errors (De Santi et al. 2001). As can be seen in Figure 34, this made the manually marked mask significantly smaller than the *FSL* (Smith et al. 2004) mask, however it does not appear to have had a large effect on the overall significance values noted in Table 3 and on the MRglc values recorded for each individual in the study (Figure 38).

Spatial warping of brain images to the MNI template was occasionally problematic, particularly for the AD brains. Two of the hallmarks of AD progression are greatly enlarged ventricles and significant cortical atrophy. These two factors make close registration to a template such as the MNI 152 template (which is based on healthy young adult brains) significantly more difficult and time consuming, and resulted in the exclusion of a large number of brain images that were downloaded from the ADNI database due to the inability to produce a good spatial warp. Elderly brain

templates are now available to improve the spatial normalisation of heavily atrophied brains to a standard space (Evans et al. 2012) The use of such a template may improve spatial normalisation results in any future research in this area.

4.5 Conclusion

Both the automated and manual processes of hippocampal masking were capable of detecting differences between groups of AD and MCI, and AD and HC brains. They were not able to detect differences between groups of MCI and HC brains. The automated system of hippocampal marking using *FSL* (Smith et al. 2004) is far less time consuming and can employ batch processing to include very large numbers of subjects, as well as increasing the ease with which the mask can be modified and updated as imaging technology improves. Furthermore, the automated marking method circumvents the need for the anatomical expertise required for manual marking. It appears that there is a difference in pons normalised hippocampal MRglc between populations of AD and either MCI or HC brains. However, there is large variation between individuals of the same diagnostic category. This variation may limit the usefulness of the technique as means of AD diagnosis; nonetheless, it may find future utility as part of a battery of tests for AD diagnosis and evaluation.

5 Clinical Utility of Hippocampal Masking in the Diagnosis of Alzheimer's Disease and Mild Cognitive Impairment

5.1 Introduction and Literature Review

Biomarkers that reliably detect the presence of AD pathology and can differentiate between HC, MCI, and AD could be used to complement or even supersede clinical cognitive assessment, and potentially lead to earlier and more accurate diagnostic outcomes. This Chapter examines the clinical utility of the hippocampal mask developed in the previous Chapter in the differential diagnosis of AD and MCI.

5.1.1 Diagnostic Threshold Selection for Diseases with Three States

For diseases in which there exist only two states (i.e. no precursor/transitional phase), a diagnostic test need only discriminate between healthy and diseased individuals. The Receiver Operating Characteristic (ROC) was developed as a means to facilitate the selection of a cut-off threshold to delineate between healthy and diseased individuals based on the result of a screening test or diagnostic assessment. The threshold can be shifted to reflect differences in the relative importance of sensitivity and specificity.

A popular method for selecting a diagnostic threshold to discriminate between binary disease states is the Youden Index (Youden 1950). The formula to calculate the Youden Index 'J' at a particular cut-off point 't' is

$$J(t) = Se(t) + Sp(t) - 1 \qquad (3)$$
(Youden 1950)

Where 'Se' is sensitivity and 'Sp' is specificity. The maximum achievable Youden Index result is 1, which is attained if a cut-off point yields both perfect sensitivity

and specificity. The minimum is zero, which is the result of a diagnostic test that fares no better than random chance.

For diseases such as AD that have an intermediate stage exhibiting some or all of the disease symptoms with reduced severity, a single ROC curve is not appropriate. Several different approaches have been taken to address the issue of classification in the scenario in which there are more than two groups. Diri and Albayrak's (2008) research used a number of different group classification methods on a thyroid dysfunction data set. The data included subjects exhibiting hypo, normal, and hyperthyroid function. They extended the ROC curve to cater for the three group case by using 'cobweb' plots that served as a means to visualise the errors across the diagnostic categories. Another study aimed to use two novel methods (closest to perfection and max volume) (Attwood et al. 2014) for threshold selection in the three class setting, and found that they were statistically indistinguishable from a three group generalised Youden Index model (Nakas et al. 2010).

The Three Group Youden Index proposed by Luo and Xiong (2013) can be used to find multiple optimal cut-off thresholds to delineate between healthy, transitional, and diseased individuals (Luo and Xiong 2013). Under the assumption of a normal distribution within each diagnostic category for subject test results, the three group method aims to define two thresholds: t_-, and t_+. The three resultant groups (D^-, D^0, and D^+) then describe the subjects that are diagnosed as healthy, intermediate, and diseased respectively.

Three different variables are then be used to quantify the suitability of the thresholds with regards to each of the three disease states. $Sp(t_-)$ is the proportion of diseased individuals whose measurement was below t_-. $Se(t_+)$ is the proportion of healthy individuals whose measurement was above t_+, and $Sm(t_-,t_+)$ is the proportion of transitional subjects that fell between the thresholds t_- and t_+.

The optimal Youden Index thresholds are found by maximising the three group Youden Index, $J_{(t_-,t_+)}$, which is defined as

$$J_{(t-,t+)} = \frac{1}{2}[Sp(t_-) + Sm(t_-, t_+) + Se(t_+) - 1] \tag{4}$$
(Luo and Xiong 2013)

The three group Youden Index is again expressed so that its value can only range from 0 to 1. If a test perfectly separates the three diagnostic categories, then the three group Youden Index is 1; whereas a three group Youden Index of 0 indicates that the test is no better than random chance at separating the groups. In the case of two of the three diagnostic groups demonstrating very little separation, the dimensions of the problem can be reduced to allow for a more simplistic ROC curve-style assessment of a single threshold.

The Youden Index gives equal weighting to both sensitivity and specificity. However, the two parameters may be weighted differently depending on the purpose of testing. For example, a test that is used to screen for a deadly infectious disease may apply a greater weighting to sensitivity than specificity, as the unnecessary quarantining of a healthy patient may be preferable to the release of an infected patient. However, if a screening test is used for a condition in which the follow-up diagnostic testing or treatment is very expensive or carries health risks, specificity may be weighted more heavily than sensitivity in order to avoid the expense or health risks incurred by unnecessarily performing further testing or treatment on healthy patients (Carneiro et al. 2011).

5.1.2   Chapter Summary

The utility of the hippocampal mask was investigated in two different scenarios. The first was when a suitable volumetric MRI was available to guide the MNI template registration of each PET image. An initial analysis of the three group data set that was based on MNI template spatial warping driven by a coregistered volumetric T1 MRI (Section 4.2) was performed using the three group Youden Index proposed by Luo and Xiong (2013). The second scenario accounts for the commonly encountered clinical setting, in which a volumetric MRI is not taken alongside a brain PET. An analysis of hippocampal MRglc was performed for ADNI PET images that were spatially warped to an MNI space PET template without the use of MRI guidance, in order to assess the potential utility of the method in the MRI-less case. Upon review

of the quantification variables, further analysis was conducted on two group data sets (AD vs Non AD), which was formed by combining the MCI and HC groups.

5.2   Materials and Methods

Patient data consisted of volumetric T1 MRI and FDG-PET brain images from the Alzheimer's Disease Neuroimaging Initiative (ADNI) database. Data from 190 subjects were used, including 51 AD, 66 MCI, and 73 HC subjects. Images were spatially normalised to the *FSL* (Smith et al. 2004) Montreal Neurological Institute (MNI) T1 MRI template through a two-stage process (approximate linear alignment followed by precise non-linear warping) that was driven by template registration with the subject MRI. A randomly selected cohort of 100 subjects (21 AD, 36 MCI and 43 HC) was used to develop an optimised hippocampal mask in MNI space, based on subject hippocampal volumes defined on the subject MRIs using the *FSL* (Smith et al. 2004) routine *FIRST* (Patenaude et al. 2011). Patient imaging details, the method used to construct the optimised hippocampal mask, and details of the MRI driven spatial normalisation procedures are in Section 4.2. The optimised hippocampal mask was used to sample the pons normalised hippocampal MRglc on PET images of the 100 subject mask development cohort and to calculate cut-off thresholds to best delineate between the diagnostic categories using the Three Group Youden Index (Luo and Xiong 2013). The ensuing MRglc cut-off thresholds were then applied to the remaining 90 subjects, a test cohort consisting of 30 AD, 30 MCI, and 30 HC subjects.

The mask development cohort data was then re-structured into two groups, AD and Non-AD, by combining the HC and MCI data. Receiver Operator Characteristic (ROC) curve analysis was utilized to calculate a threshold to delineate between the two newly formed diagnostic classes. The threshold was then applied to the 90 subject test cohort.

Volumetric MRI is often unavailable in a clinical setting. This scenario was simulated through the use of a separate spatial normalisation procedure, in which the PET images for each patient were spatially normalised to an MNI space H_2O^{15} PET

template from the software package Statistical Parametric Mapping (SPM) (Friston 2007). Subject PET images were spatially normalised to the PET template using a similar two-step process to that used for the MRI driven spatial normalisation. Firstly, a 12 degree of freedom affine transformation was calculated using the *FSL* routine *flirt* (Jenkinson et al. 2002) to calculate an approximate alignment with the template. Secondly, precise template registration was achieved via calculation of nonlinear warps using the *FSL* routine *fnirt* (Andersson et al. 2007). The process of PET driven template registration is illustrated in Figure 39.
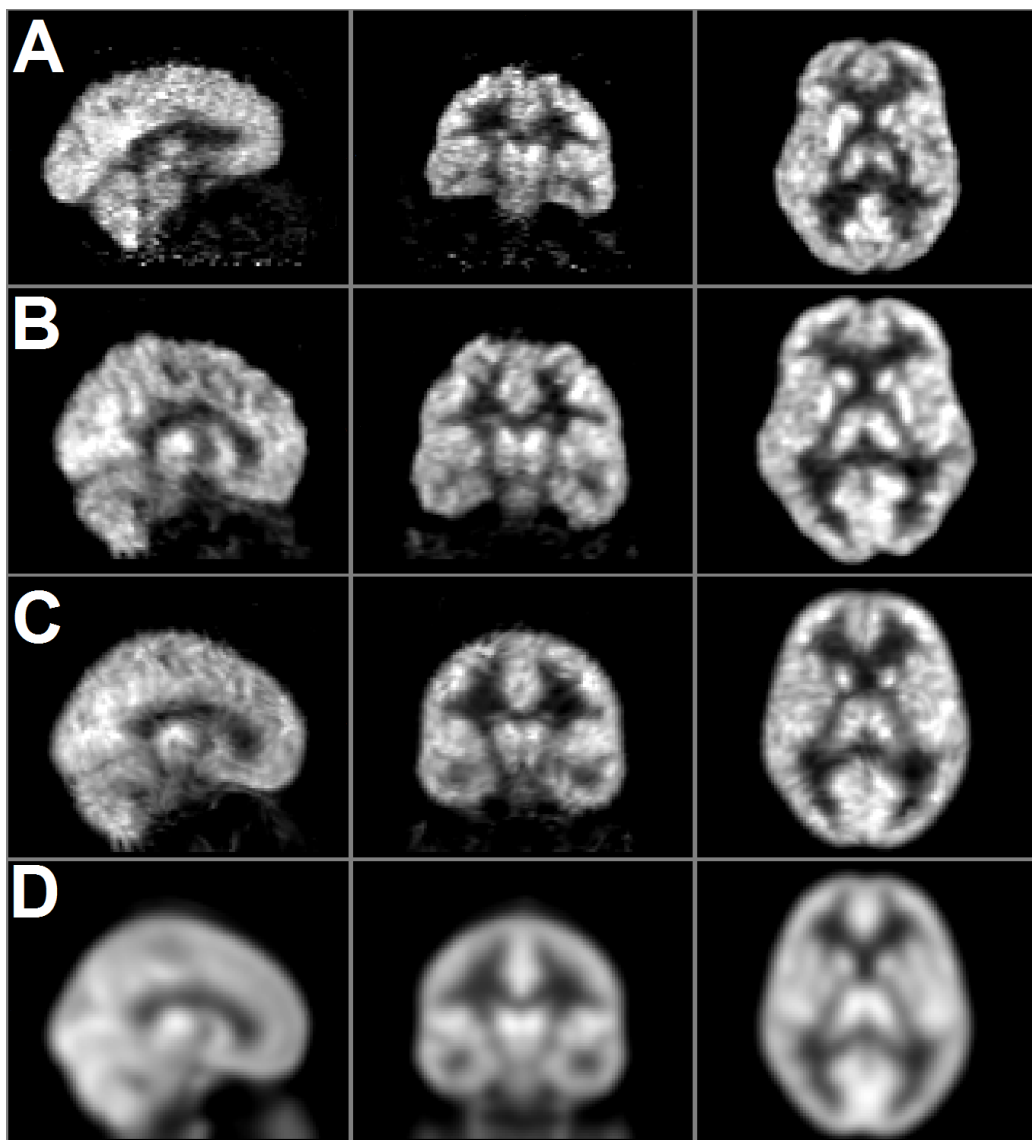
Figure 39, (Part A): A native space ADNI PET image, (Part B): The PET image after the application of a 12 DOF affine transform, (Part C): The PET image after the application of a series of nonlinear warps to co-regiester it with (Part D): The SPM (Friston 2007) PET template.

The Statistics software program *R* (R Core Team 2015) was used for the statistical calculations. The package *DiagTest3Grp* (Luo and Xiong 2012) was used to compute the Three Group Youden Indices, and *pROC* (Robin et al. 2011) and *Optimal Cutpoints* (Lopez-Raton et al. 2014) were used and perform ROC analysis.

5.3   Results

5.3.1   MRI Driven Template Registration Data Set

Figure 40 shows the distribution of pons normalised hippocampal MRglc in the 100 subject mask development cohort, as measured by the optimised hippocampal mask. An outlier (greater than three times the inter-quartile range from the edge of the box) is present in the AD group. Inspection of the subject images revealed that a severe level of hippocampal atrophy resulted in the mask sampling the ventricle rather than the brain tissue. This is further explained in Figure 49, Section 5.4. All further analysis of the 100 subject mask development group excluded the outlier, the box and whisker plot of the data set with the outlier removed can be seen in Figure 41.
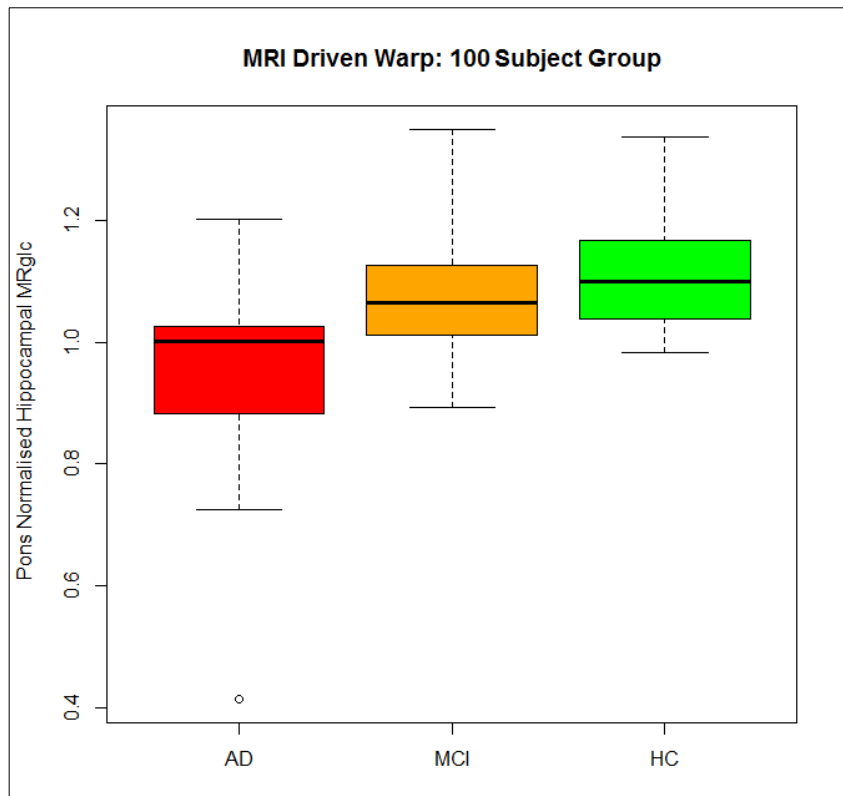
Figure 40, A box and whisker plot displaying the pons normalised hippocampal MRglc for the 100 subject mask development cohort.
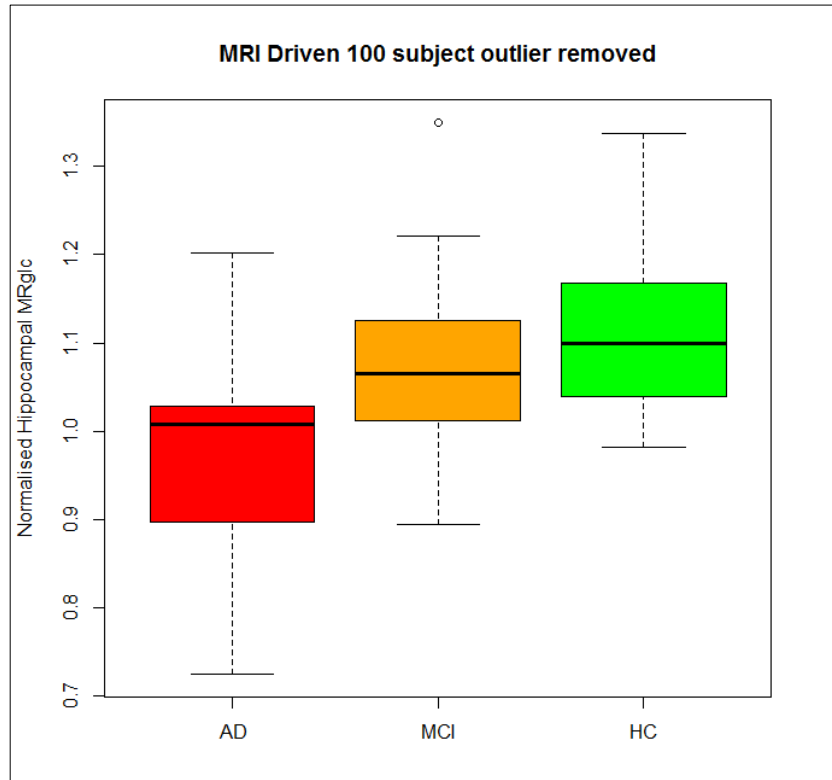
Figure 41, A box and whisker plot displaying the pons normalised hippocampal MRglc for the mask development cohort after the removal of the outlier from the AD group.

Figure 42 is a scatter plot and box and whisker plot displaying the spread of the pons normalised hippocampal metabolism data for the three diagnostic categories. The horizontal dashed lines indicate the t_+ and t_- cut-off thresholds that maximised the Three Group Youden Index.
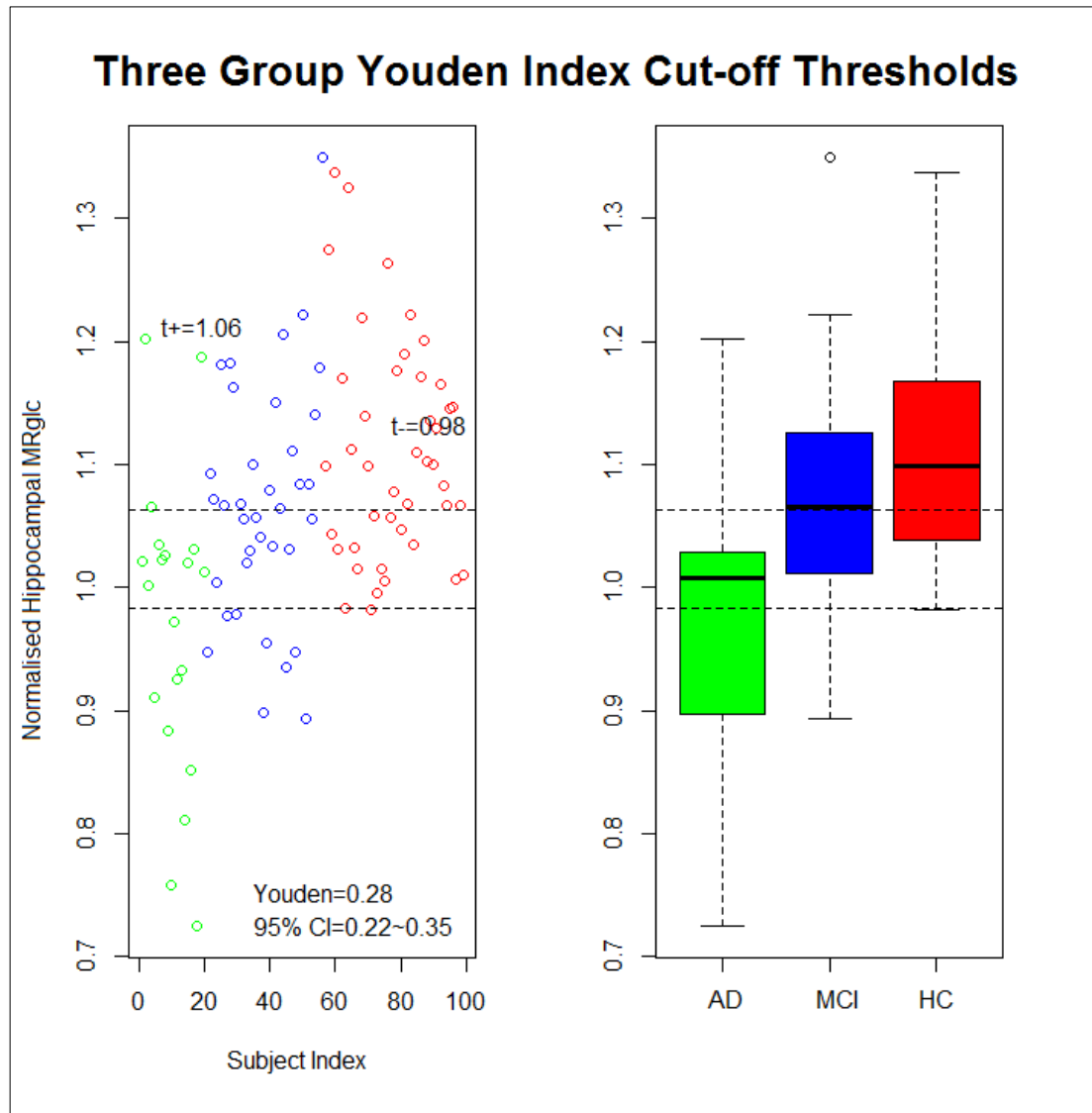
Figure 42, A graphical representation of the three group Youden Index and cut-off threshold selection for the mask development cohort.

The value for each of the group classification probabilities were:

$Sp(t_-)$: 0.56

$Sm(t_-,t_+)$: 0.31

$Se(t_+)$: 0.69

The cut-off thresholds were:

Lower Threshold (t_-): 0.98

Upper Threshold (t_+): 1.06

These classification probability values indicate the rate at which the thresholds are able to correctly classify each diagnostic category. $Sp(t_-)$, $Sm(t_-,t_+)$, and $Se(t_+)$ relate to AD, MCI, and HC respectively. The low value of $Sm(t_-,t_+)$ indicates that the majority of the MCI subjects fell outside of the 'central' region that exists between the thresholds in Figure 42. The lower and upper cut-off thresholds from the Three Group Youden Index analysis (t_+ and t_- in Figure 42) were applied to the 90 subject test group to assess their diagnostic efficacy; the results can be seen in Table 4.

	AD	MCI	HC	Total
Correct	26	11	23	60
Incorrect	4	19	7	30

Table 4, The results of applying the cut-off thresholds from the MRI driven spatial normalisation mask development data set Three Group Youden Index analysis to the 90 subject test data set.

The thresholds correctly categorised AD and HC patients 87% and 77% of the time, respectively. The MCI categorisation had poor efficacy, with only 37% of MCI subjects being correctly diagnosed. Of the subjects that were misdiagnosed, 12 fell above the t_+ cut-off threshold, meaning that more MCI subjects were classified as HC than were classified as MCI.

The Three Group Youden Index method was unable to produce a cut-off threshold that could reliably separate MCI subjects from the other diagnostic classes. Due to this, and the fact that the distribution of MCI subjects is similar in appearance to the HC subject distribution (as can be seen in the location of the inter-quartile boxes in Figure 42), a reduction in dimensionality was performed so that there were only two groups involved: AD and non-AD (including 20 and 79 subjects respectively for the mask development cohort). Analysis of the two group data set included ROC curve computation and the calculation of the Youden Index to determine the best value of normalised hippocampal metabolism to discriminate between the two new groups. The results of these methods can be seen in Figure 43 and Figure 44.

Figure 43 is a boxplot displaying the data set after it had been reduced down to two groups.
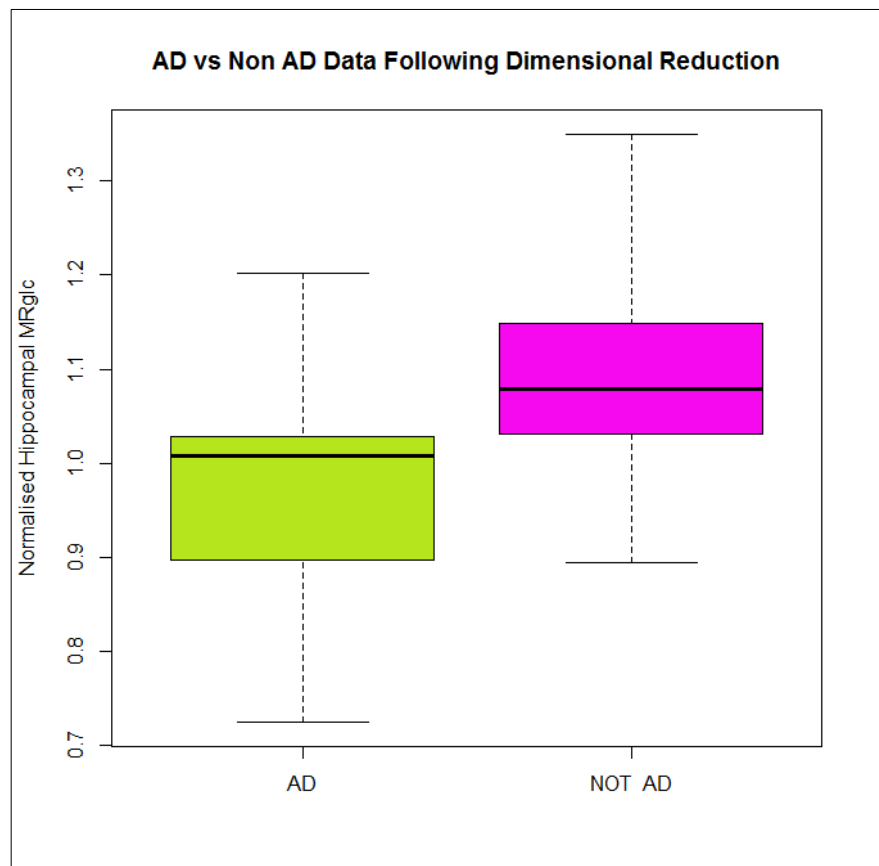
Figure 43, A box and whisker plot illustrating the distribution of the two group pons normalised hippocampal metabolism data for the MRI driven mask development cohort.

Figure 44 shows the ROC curve that was calculated based on the dimension reduced data set. The area under the curve (AUC) was 0.79.
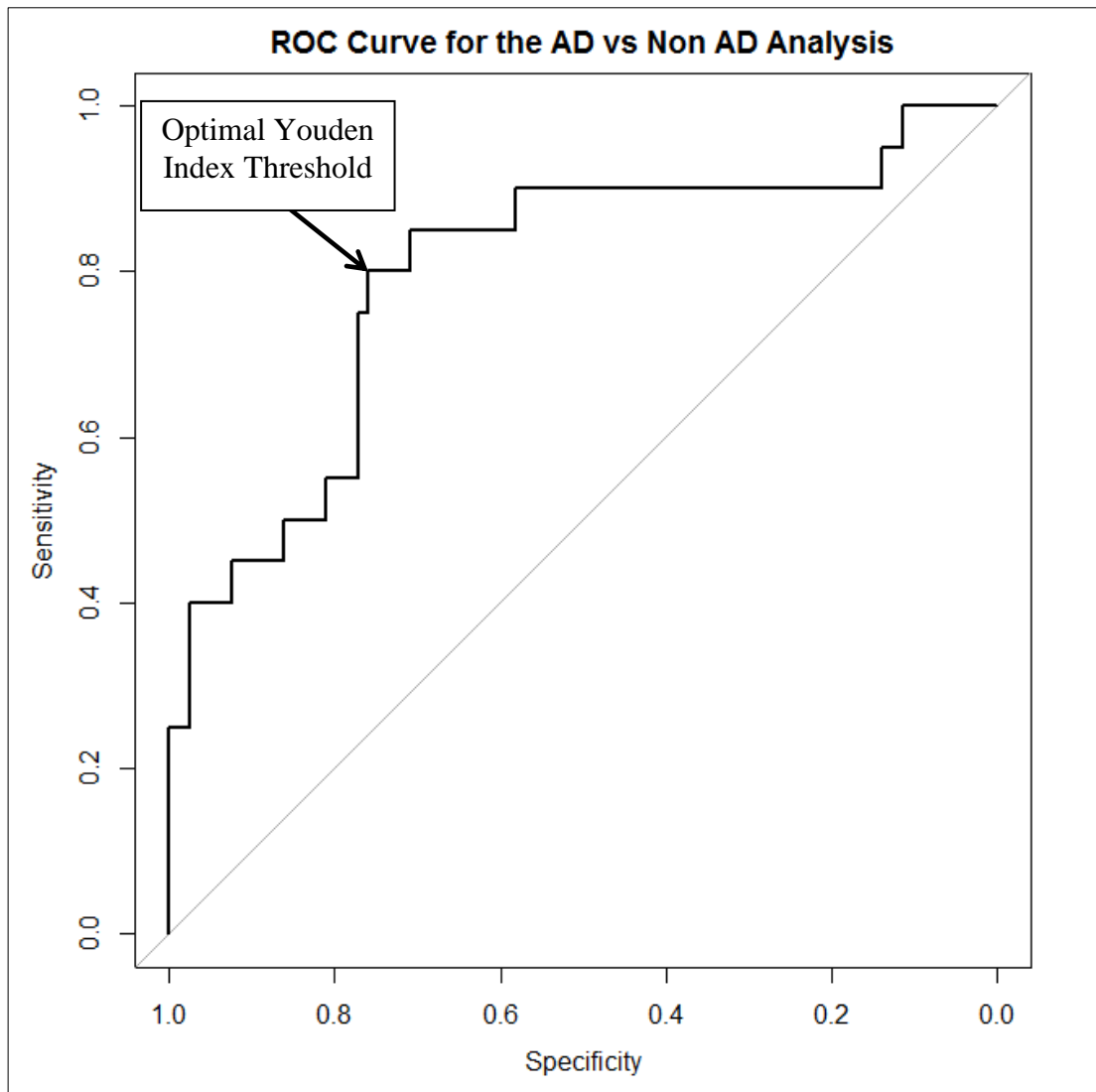
Figure 44, The ROC curve displaying the variation of sensitivity and specificity with cut-off threshold selection for the reduced dimension data set (AD vs non-AD), as well as the point on the curve that optimises the Youden Index for the MRI driven mask development cohort.

The Youden Index optimal cut-off threshold for pons normalised hippocampal metabolism for the two group data set was 1.03. The sensitivity and specificity at this threshold were 0.80 (95% CI 0.56-0.89) and 0.76 (95% CI 0.65-0.81) respectively. The point at which this threshold sits on the ROC curve can be seen in Figure 44.

The cut-off threshold from the mask development cohort was then applied to the 90 subject test cohort after re-structuring into AD and Non AD classes (including 30 and 60 subjects respectively); the results are summarised in Table 5.

True Positive	25
False Negative	5
True Negative	37
False Positive	23
Sensitivity (95% CI)	0.83 (0.65-0.9)
Specificity (95% CI)	0.62 (0.48-0.68)

Table 5, The results of applying the cut-off thresholds from the MRI driven mask development data set ROC curve Youden Index Analysis to the 90 subject test data set, including 95% confidence intervals for sensitivity and specificity.

5.3.2   PET Driven Template Registration Data Set

In order to draw comparisons between the MRI driven spatial warping procedures and its PET only equivalent, the PET driven data were analysed in the same manner as the MRI driven data. Figure 45 is a box and whisker plot displaying the distribution of pons normalised hippocampal metabolism for the mask development cohort (after removal of the outlier seen in Figure 40).
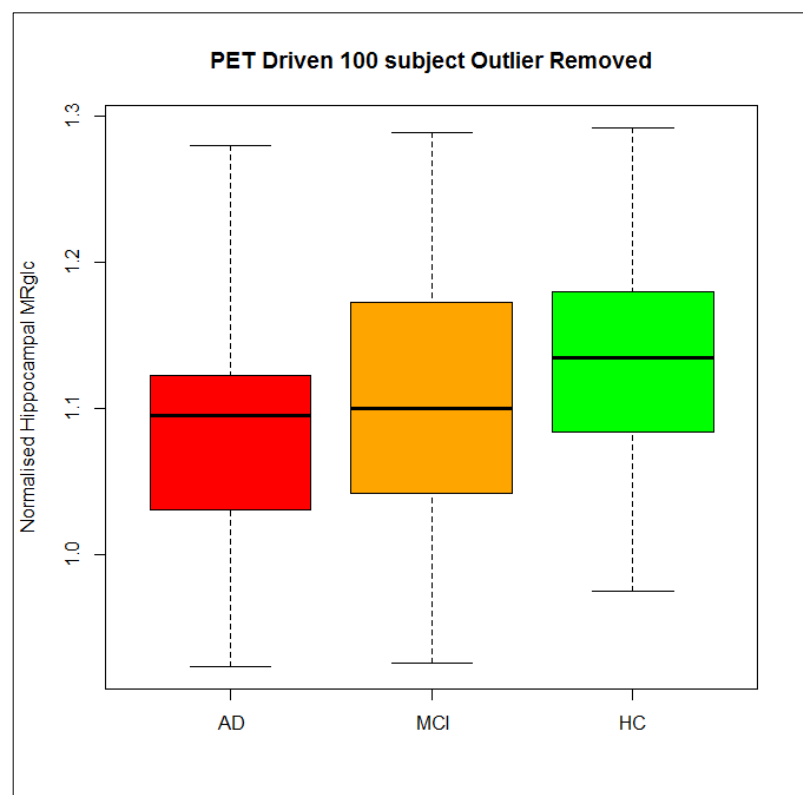
Figure 45, A box and whisker plot displaying the pons normalised hippocampal MRglc for the mask development cohort after the removal of the outlier from the AD group, based on the PET driven spatial warp.

Figure 46 is a scatter plot and box and whisker plot displaying the distribution of the pons normalised hippocampal metabolism data for the three diagnostic categories from the PET driven spatial warp. The horizontal dashed lines indicate the t_+ and t_- cut-off thresholds that maximised the 3 group Youden Index.
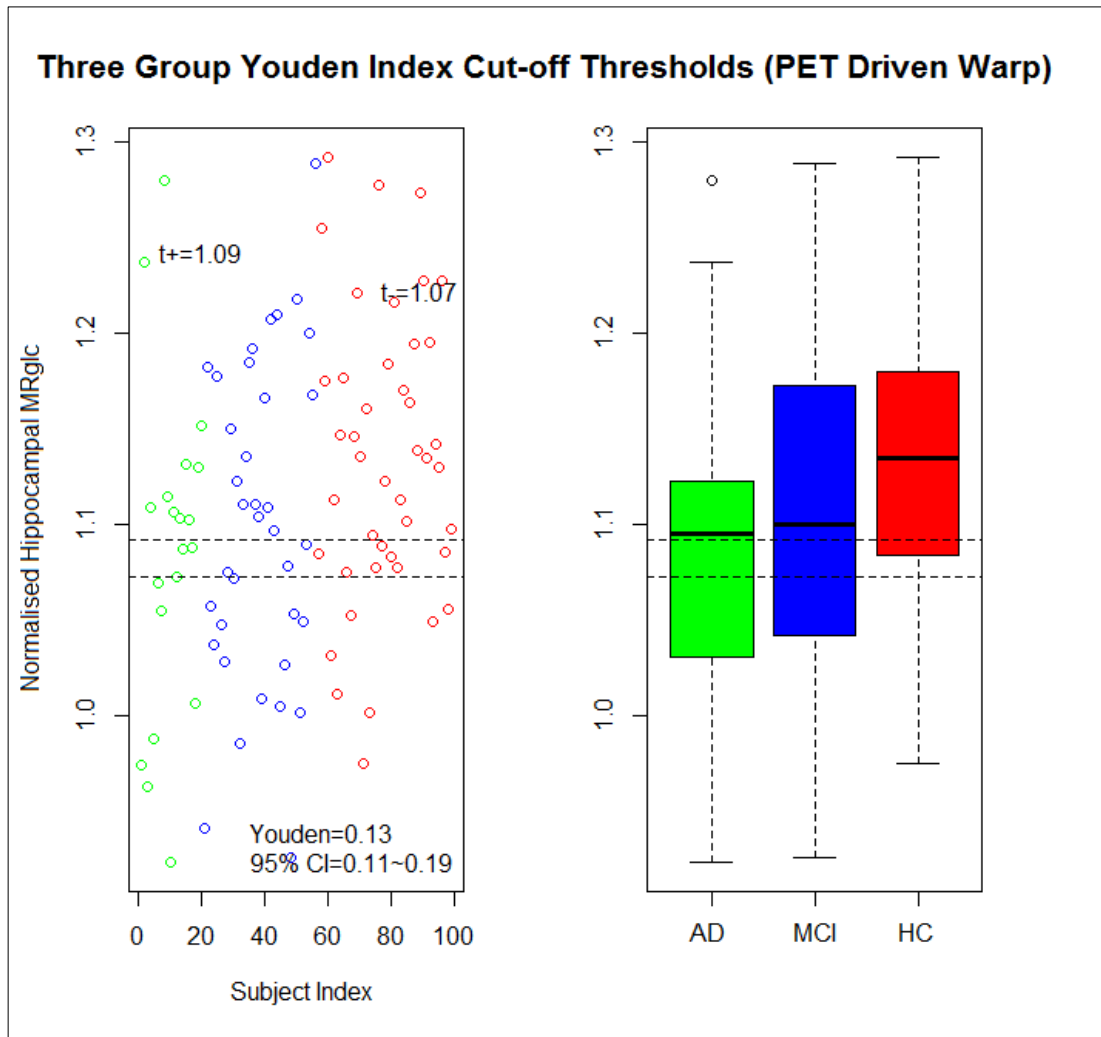
Figure 46, A graphical representation of the three group Youden Index and cut-off threshold selection for the mask development cohort PET driven spatial warp.

The value for each of the group classification probabilities were:

$Sp(t_-)$: 0.46

$Sm(t_-,t_+)$: 0.09

$Se(t_+)$: 0.70

The cut-off thresholds were:

Lower Threshold (t_-): 1.07

Upper Threshold (t_+): 1.09

The optimal Three Group Youden Index thresholds were then applied to the 90 subject test data set, the results of this can be seen in Table 6.

	AD	MCI	HC	Total
Correct	21	1	21	43
Incorrect	9	29	9	47

Table 6, The results of applying the cut-off thresholds from the PET driven 100 subject mask development data set Three Group Youden Index analysis to the 90 subject test data set.

The thresholds correctly categorised AD and HC patients 70% of the time. The MCI categorisation had extremely poor efficacy, with only 3% of MCI subjects being correctly diagnosed. As noted with the MRI driven spatial warp data, a majority of the misdiagnosed MCI subjects were classified as HC; this was the case for 18 of the 29 misclassified subjects.

Figure 47 shows the distribution of the PET driven spatial normalisation data after the reduction in dimensions to AD vs Non AD.
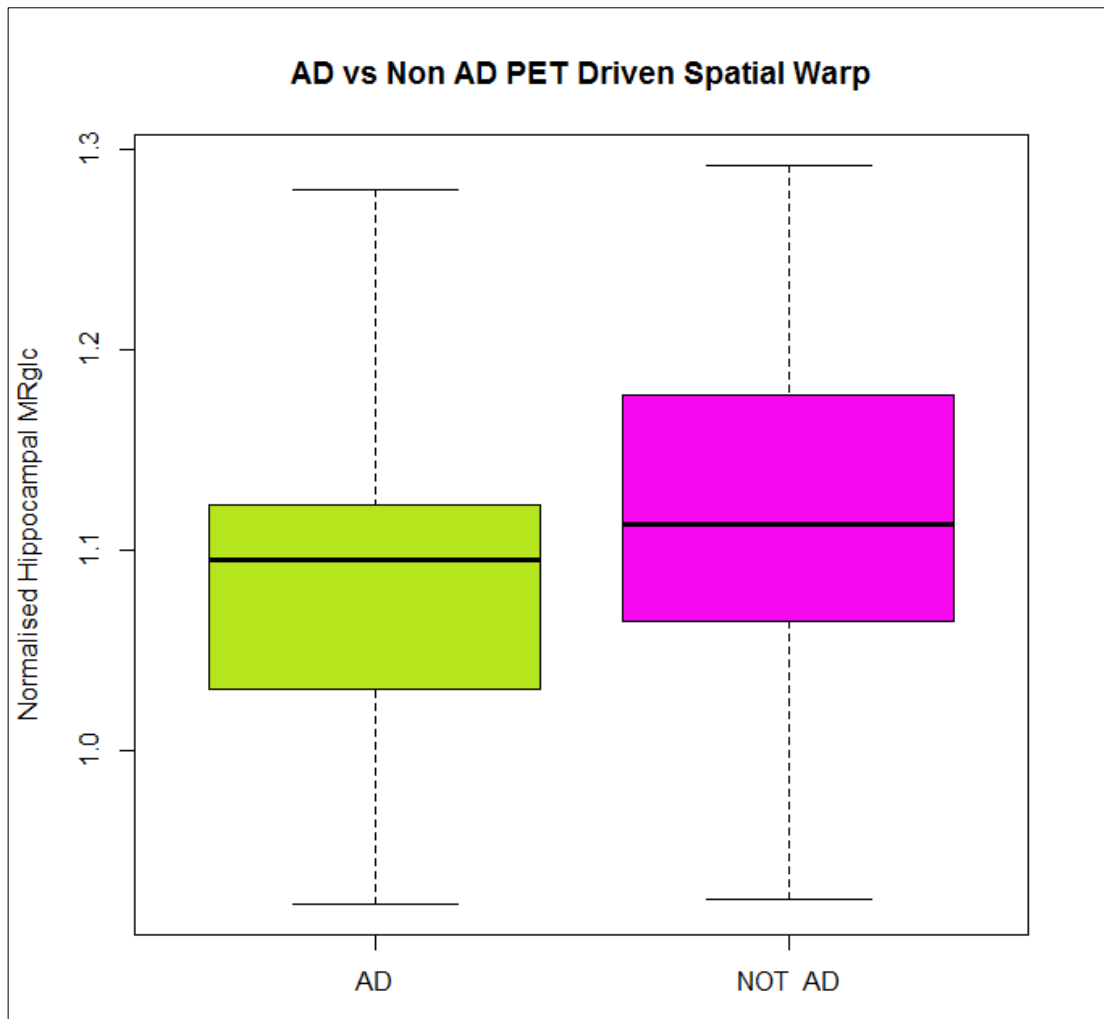
Figure 47, A box and whisker plot illustrating the distribution of the two group pons normalised hippocampal metabolism data for the PET driven mask development cohort.

Figure 48 shows the ROC curve that was calculated, based on the data presented in Figure 47, including the point that corresponds to the optimal Youden Index cut-off threshold. The AUC was 0.62.
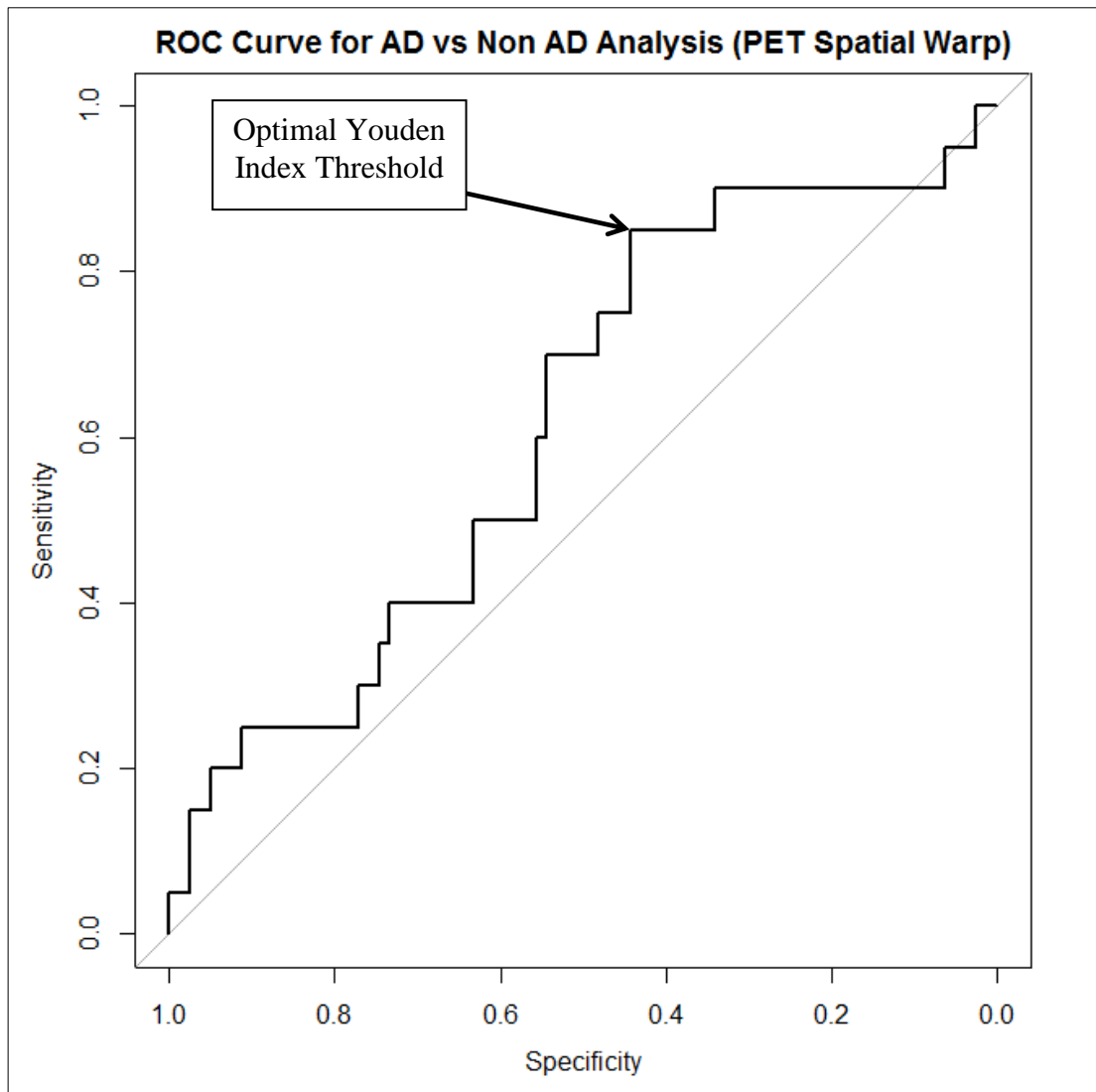
Figure 48, The ROC curve displaying the variation of sensitivity and specificity with cut-off threshold selection for the reduced dimension data set (AD vs non-AD), as well as the point on the curve that optimises the Youden Index for the PET driven 100 subject mask development cohort.

The Youden Index optimal cut-off threshold for the data set was 1.13. The sensitivity and specificity at this threshold were 0.85 (95% CI 0.62-0.93) and 0.44 (95% CI 0.33-0.50) respectively. The point at which this threshold sits on the ROC curve can be seen in Figure 48.

The cut-off threshold from the mask development cohort was then applied to the 90 subject test cohort, the results are summarised in Table 7.

True Positive	25
False Negative	5
True Negative	29
False Positive	31
Sensitivity (95% CI)	0.83 (0.65-0.9)
Specificity (95 % CI)	0.48 (0.35-0.55)

Table 7, The results of applying the cut-off thresholds from the PET driven 100 subject mask development data set ROC curve Youden Index Analysis to the 90 subject test data set, including 95% confidence intervals for sensitivity and specificity.

5.4 Discussion

For a diagnostic test or screening procedure to be used clinically, there must be a point at which an individual is considered to be disease positive/potentially disease positive. For some procedures, such as identifying potential lesions in mammography screening, this is not necessarily achieved through a binary quantification, but rather a conclusion reached by an individual upon inspection of the test results. For the mammography example, this is a radiologist reviewing a mammogram. For the purposes of determining the utility of the pons normalised hippocampal metabolism quantification method in diagnosing MCI and AD, a definitive quantification or cut-off threshold(s) was sought for use in the formation of a diagnosis. The potential utility of the method was also investigated for the case in which no volumetric MRI is available to drive template spatial registration, as is often the case in a clinical setting.

The presence of MCI, considered to be an intermediate "transition" state that can present before a subject progresses to AD (Albert et al. 2011), complicates the formation of a quantitative diagnostic threshold. Figure 40 presents the distribution of pons normalised hippocampal MRglc data for the 100 subject mask development cohort. There is an outlier in the AD group that has an MRglc measurement far below any others in the data set. Upon investigation of that subject's images, it

became apparent that the optimised mask had erroneously sampled the lateral ventricles as well as the hippocampal tissue, a result of spatial registration errors caused by severe atrophy within the patient's medial temporal lobe. This can be seen in Figure 49. No other subject brains were so severely affected by errors in spatial normalisation, so the outlier was removed and further analysis of the mask development cohort was conducted on the remaining subjects.
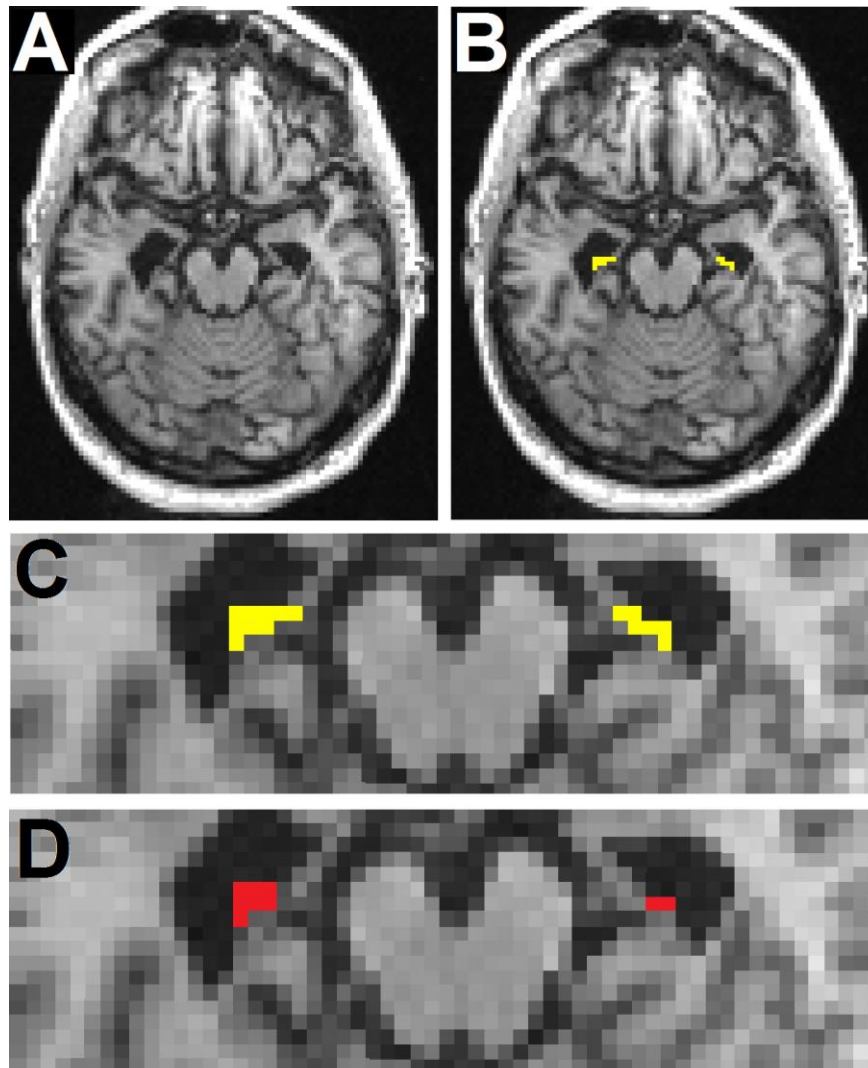
Figure 49, Images of the MNI template spatially normalised subject brain that showed an abnormally low measurement of pons normalised hippocampal MRglc in Figure 40. (Part A): A trans-axial slice through the subject brain at the level of the hippocampus, (Part B): The same slice overlaid with the optimised automated FSL (Smith et al. 2004) hippocampal mask (yellow voxels), (Part C): The masked region at a higher magnification, (Part D): The mask voxels that fell within the lateral ventricles on the subject brain, rather than the hippocampus (red voxels).

5.4.1 MRI Driven Template Registration Data Set

A classic ROC curve cannot be easily used to identify multiple thresholds to delineate between more than two disease states. Although there isn't a widely used ROC curve alternative for the three group case, the Youden Index has been expanded to allow for quantitative threshold calculation in this scenario (Luo and Xiong 2012). Figure 42 shows the results of the Three Group Youden Index calculation, which resulted in the identification of two thresholds (t_- and t_+) that optimised the Youden Index function (Equation 2).

With reference to Figure 42 and the accompanying value for $Sm(t_-,t_+)$ (0.31), it can be seen that it is not possible to reliably delineate between MCI and AD/HC subjects. As a result of this, and the fact that the majority of misdiagnosed MCI cases were classified as HC, the data were re-structured and the MCI and HC subjects were grouped together.

The re-structuring of the data allowed for the creation of a classic ROC curve (Figure 44), from which an optimal cut-off threshold was derived in order to separate the AD and Non AD groups. This threshold was then applied to the 90 subject test data set to evaluate its performance, the results of which are presented in Table 5. While the true positive rate of 83% is encouraging, the rate of false positives (38%) is too high for this method to have much utility on its own as a diagnostic tool.

5.4.2 PET Driven Template Registration Data Set

Figure 46 shows the results of the Three Group Youden Index calculation. The optimal Youden thresholds effectively eliminate the presence of the intermediate (MCI) diagnostic category. The fact that the highest overall Youden index was achieved by minimising the MCI category to a great extent is symptomatic of the lack of separation between the MCI and either the AD or HC groups.

The AUC values for the AD vs non AD ROC curve in Figure 44 is higher than for Figure 48, indicating that the MRI driven warping procedure is superior to its PET

only equivalent for separating the two groups. Both techniques were able to diagnose AD in the 90 subject test cohort with the same sensitivity (83%). The MRI driven spatial normalisation method showed higher specificity (0.62, 95% CI: 0.48-0.68) than the PET driven equivalent (0.48, 95% CI: 0.35-0.55); however, this was not significant at the 95% confidence level.

5.4.3 Summary

In order for the MRI driven spatial registration method to be used clinically, a patient needs to have had a set of structural and functional images of the brain already acquired. The PET only registration method produced an ROC AUC value (0.62) that was inferior to that seen on the MRI driven registration (0.79). Neither of the data analysis methods produced results that warrant the use of the method as a stand-alone screening procedure for AD. However, a process in which these images are fed through an algorithm that quantifies their pons normalised hippocampal metabolism and includes other biomarkers that can be automatically assessed and quantified, may increase the sensitivity and specificity seen from the testing. Examples of other potential biomarkers include hippocampal volume, amygdala metabolism and volume, and ventricle and overall brain volume.

The method is limited in its potential clinical utility in part by the difficulty in accurate nonlinear registration of an atrophied elderly brain to a template based on healthy adult brains (the McConnell Brain Imaging Centre (Montreal Neurological Institute (MNI), McGill University Montreal) 152 nonlinear 6th generation T1 1mm resolution brain template). Only around one in two subjects yielded suitable spatially warped brain volumes for further analysis with minor modification of the warping process; manual adjustment was often required with regards to brain masking and fine tuning of the affine registration. Clinical use of this technique will probably be better served by the use of a more appropriate 'elderly' template, as the degree of spatial normalisation required for the average individual will be lower, likely leading to less discarded data and an improvement in the data that is available.

5.5 Conclusion

To assess the utility of the pons normalised hippocampal metabolism quantification method in a clinical setting, several options for the formation of cut-off thresholds to delineate between the three diagnostic categories were investigated. Two different data sets were analysed; one that used a subject's volumetric MRI to guide spatial registration, and another which relied solely on the use of their FDG-PET image. The Three Group Youden Index was calculated for each approach, and it was found that neither spatial registration method was able to separate the MCI subjects from the other diagnostic classes.

Due to the inability to separate out the MCI subjects from the other diagnostic classes, the data were restructured. The MCI and HC groups were merged into a single 'Non AD' group which was then re-analysed with respect to the AD group. ROC curves were constructed for each method, and the Youden Index was calculated in order to determine an optimal cut-off threshold to separate the two groups. The MRI driven spatial warp was superior to the PET driven method with regards to AUC on the ROC curve and specificity when making a diagnosis using the optimal Youden Index threshold.

In its current form, the method serves as a demonstration of the reduction in hippocampal metabolism between AD sufferers and healthy elderly people. However, the large variation between individuals limits the potential of the method. It may likely find greatest utility as part of a suite of automatically acquired biomarkers that combine to render an overall impression of cerebral health.

6 Conclusions and Future Work

6.1 Summary and Evaluation

Linear and nonlinear spatial registration of brain volumes to a standard template has formed the framework on which this research is developed. All images were spatially transformed to conform to the common space defined by the Montreal Neurological Institute (MNI) using *FSL*. The ability to conduct automated inter-subject comparisons at the voxel level across large groups of subjects is made possible by these pre-processing spatial registration steps to ensure they occupy the same standard space.

A comparison of post-injection imaging times for two different PET radioisotopes (^{11}Carbon-Methionine (CMET) and 3'-deoxy-3'-^{18}Fluorine-Fluorothymidine (FLT)) in a group of post treatment glioma patients was conducted. The PERCIST guidelines (Wahl et al. 2009) were used to define a background healthy tissue normalised SUV_{PEAK} volume. The highest average uptake within a 1cm^3 sphere inside the tumour affected area was found in each PET image. Background uptake was represented by an identical sphere, located in the contralateral hemisphere, which was positioned by reflecting the highest uptake tumour sphere about the mid-sagittal plane. The background normalised SUV_{PEAK} was then defined in the CMET images as the ratio of the tumour/background average uptake spheres. In the FLT images, the difference in SUV between the spheres was used, due to the extremely low uptake of FLT regions in which the blood-brain barrier (BBB) remains intact. Tukey's HSD test was used to compare the four CMET post-injection imaging time points (10, 20, 30, and 40 minutes) at the group level. A downwards trend can be seen in Figure 16 in Section 2.3; the tumour-background contrast at both 10 and 20 minutes was found to be higher than at 40 minutes at the 99% confidence level. A two-sided paired t-test was used to compare the FLT imaging time points (15 and 75 minutes post injection). Tumour-background contrast at 15 minutes was found to be significantly higher than at 75 minutes ($p < 0.005$). These results suggest that earlier imaging using these isotopes for this application (less than 40 and 75 minutes for

CMET and FLT respectively) may be important to maximise tumour-healthy tissue contrast.

The same cohort of post treatment glioma patients was used in another investigation that sought to assess the utility of CMET-PET, FLT-PET and Gd-MRI to predict survival outcomes based on the volume of tissue that demonstrated uptake/enhancement that was significantly elevated above background (considered to be viable tumour volume for the modality). Each PET brain volume was divided along the mid-sagittal plane to create distinct hemispheres for tumour and background healthy tissue. CMET-PET background normalisation was performed for each voxel in the tumour hemisphere by taking the ratio with the contralateral voxel; voxels with a ratio of greater than 1.5 were considered viable tumour volume. The same process was used for background normalisation of the FLT-PET images, except the difference in SUV between tumour and background voxels was used for normalisation. FLT-PET tumour hemisphere voxels with an SUV difference that was greater than 0.2 above background were considered viable tumour volume. A manual thresholding process on the MR images was used to define the tissue volume that showed increased uptake due to Gd-MRI pooling in areas of blood-brain barrier disruption. ROC curve analysis was used to identify the optimal tumour volume threshold above which a subject's survival would be less than the median survival time (78 weeks) of the cohort for each modality. Survival time differences for subjects with volumes below and above the optimal values were examined using a log-rank test. CMET-PET was the only modality to produce a significant difference between the small and large viable tumour volume groups at the 95% confidence level. FLT-PET and Gd-MRI are considered to be primarily agents that highlight the areas in which blood-brain barrier disruption has occurred. The results found in this investigation support this hypothesis, as high uptake/enhancement with these modalities did not have a significant correlation with survival, indicating that they're not necessarily highlighting viable tumour volume. The results also indicate that CMET-PET may be an effective means of highlighting viable tumour volume in post-treatment glioma brains.

The remainder of the work focussed on the validity and clinical utility of hippocampal glucose metabolism in FDG-PET as a diagnostic indicator for AD.

Large scale atrophy within the cerebral cortex, as well as smaller scale atrophy in structures such as the hippocampus, can be seen in AD patients using structural MRI (Apostolova et al. 2012). Research employing automated VBA methods can detect large scale MRglc reductions on FDG-PET images, but almost always fails to find MRglc reductions in the hippocampus (Mosconi et al. 2005). This discrepancy is likely due to the small volume of the hippocampus and the errors inherent in the spatial registration of comparatively low resolution PET images to an anatomical template. An optimised mask created using manually marked hippocampal peripheries on T1 MRIs has been shown to be accurate in defining the hippocampus on spatially normalised FDG-PET images, and for detecting reductions in hippocampal MRglc in patients with MCI and AD (Mosconi et al. 2005). In this research, two optimised hippocampal masks were compared. One was comprised of a small number (n = 21) of subjects whose hippocampi were marked manually on the subject MRIs, the other from 100 subjects that had been processed using an automated subcortical segmentation algorithm. The masks were compared with regards to their ability to find group level differences between the average pons normalised hippocampal metabolism in AD, MCI, and HC brains. It was demonstrated that the masks produced near identical results. Neither mask was able to separate the MCI from HC groups, but both found significant differences between AD and HC ($p < 0.0005$) and AD and MCI ($p < 0.005$) groups using Tukey's HSD test.

The potential clinical utility of hippocampal masking with regards to AD diagnosis was then investigated. The automated mask was chosen for this analysis, as it was considered more defensible from a reproducibility standpoint. The clinical utility of the mask was tested using MRI driven spatial warping of FDG-PET images to MNI space and, since volumetric MRI has frequently not been performed as a routine part of patient workup in a clinical setting, a comparative data set was created where the FDG-PET images were spatially warped directly to an MNI space PET template. An extension of the Youden Index for the three group case was used to assess the utility of a bi-threshold method for diagnosing an individual as either HC, MCI, or AD for the MRI-driven and PET-driven spatial warp data sets. Both spatial warping methods demonstrated an inability to separate MCI subjects from either AD or HC subjects. As a result, the subjects were split into two groups: AD and non-AD, to allow for

ROC curve analysis with a view to constructing a threshold that may find utility as an AD screening method. There were no differences between the methods in sensitivity or specificity with regards to AD diagnosis at the 95% confidence level. This method of automated hippocampal metabolism assessment, used as a screening process for identifying subjects that are at risk of AD, will likely only find utility as part of a suite of tests including other biomarkers such as hippocampal volume, overall brain volume, ventricular enlargement, and the presence of other AD biomarkers such as amyloid β protein plaques.

6.2   Recommendations for Future Research

Accurate identification of cancerous tissue in post-treatment glioma patients is an ongoing imaging problem. Future nuclear medicine imaging work will likely focus on radionuclides that can penetrate an intact BBB; imaging agents that cannot are unable to detect lesions outside the regions of BBB disruption. Furthermore, such agents potentially face difficulties in distinguishing elevated uptake due to tumour tissue to that which is due to diffusion alone. Another PET imaging agent that has shown utility in both pre- (Jansen et al. 2015) and post-treatment (Popperl et al. 2004) glioma imaging, and which will continue to be the focus of future studies is O-(2-18F-fluoroethyl)-L-tyrosine (FET).

The image and survival analysis method used in Chapter 3 has the potential to be used in future longitudinal brain imaging studies. The high degree of automation of the method lends itself to studies involving large numbers of subjects through the use of batch processing. The technique will be utilised in the near future for image analysis in a FET-PET glioma imaging study at Sir Charles Gairdner Hospital, allowing for further refinement of the technique and assessment of its utility.

Detecting differences in hippocampal metabolism between groups of HC, MCI, and AD patients using automated hippocampal masking in FDG-PET may have future utility as a clinical screening method. The potential of the method will be increased by improvements in image resolution, as well as an improved system of spatial registration. The use of an age range appropriate brain template such as the Elderly

Brain Template from the University of California Neuroscience Imaging Centre (San Francisco, CA) (http://sfnic.ucsf.edu/Brain_Template.html) will likely be beneficial for improving the accuracy of spatial registration. Furthermore, research into the combined use of other characteristic AD biomarkers such as increased ventricular volume, decreased cerebral and hippocampal volume, and Amyloid β protein plaque deposition may provide higher accuracy in predicting and diagnosing the disorder.

7   References

ADNI (2006). Alzheimer's Disease Neuroimaging Initiative PET Technical Procedures Manual

ADNI (2008). ALZHEIMER'S DISEASE NEUROIMAGING PROTOCOL

Aki, T., N. Nakayama, S. Yonezawa, S. Takenaka, K. Miwa, Y. Asano, J. Shinoda, H. Yano and T. Iwama (2012). "Evaluation of brain tumors using dynamic 11C-methionine-PET." J Neurooncol **109**(1): 115-122.

Albert, M. S., S. T. DeKosky, D. Dickson, B. Dubois, H. H. Feldman, N. C. Fox, A. Gamst, D. M. Holtzman, W. J. Jagust, R. C. Petersen, P. J. Snyder, M. C. Carrillo, B. Thies and C. H. Phelps (2011). "The diagnosis of mild cognitive impairment due to Alzheimer's disease: recommendations from the National Institute on Aging-Alzheimer's Association workgroups on diagnostic guidelines for Alzheimer's disease." Alzheimers Dement 7(3): 270-279.

Andersson, J. L. R., M. Jenkinson and S. Smith (2007). Non-linear registration aka Spatial normalisation. Oxford, United Kingdom, FMRIB Centre.

Apostolova, L. G., A. E. Green, S. Babakchanian, K. S. Hwang, Y. Y. Chou, A. W. Toga and P. M. Thompson (2012). "Hippocampal atrophy and ventricular enlargement in normal aging, mild cognitive impairment (MCI), and Alzheimer Disease." Alzheimer Dis Assoc Disord **26**(1): 17-27.

Attwood, K., L. Tian and C. Xiong (2014). "Diagnostic thresholds with three ordinal groups." J Biopharm Stat **24**(3): 608-633.

Australian Institute of Health and Welfare (2012). Dementia In Australia. Canberra.

Basen-Engquist, K., R. T. Fouladi, S. B. Cantor, E. Shinn, D. Sui, M. Sharman and M. Follen (2007). "Patient assessment of tests to detect cervical cancer." Int J Technol Assess Health Care **23**(2): 240-247.

Behin, A., K. Hoang-Xuan, A. F. Carpentier and J. Y. Delattre (2003). "Primary brain tumours in adults." Lancet **361**(9354): 323-331.

Bergstrom, M., V. P. Collins, E. Ehrin, K. Ericson, L. Eriksson, T. Greitz, C. Halldin, H. von Holst, B. Langstrom, A. Lilja and et al. (1983). "Discrepancies in brain tumor extent as shown by computed tomography and positron emission tomography using [68Ga]EDTA, [11C]glucose, and [11C]methionine." J Comput Assist Tomogr **7**(6): 1062-1066.

Betz, A. L. and G. W. Goldstein (1978). "Polarity of the blood-brain barrier: neutral amino acid transport into isolated brain capillaries." Science **202**(4364): 225-227.

Blennow, K., B. Dubois, A. M. Fagan, P. Lewczuk, M. J. de Leon and H. Hampel (2015). "Clinical utility of cerebrospinal fluid biomarkers in the diagnosis of early Alzheimer's disease." Alzheimers Dement **11**(1): 58-69.

Bookstein, F. L. (1989). "Principal warps: Thin-plate splines and the decomposition of deformations." IEEE Transactions on pattern analysis and machine intelligence **11**(6): 567-585.

Brandsma, D., L. Stalpers, W. Taal, P. Sminia and M. J. van den Bent (2008). "Clinical features, mechanisms, and management of pseudoprogression in malignant gliomas." Lancet Oncol **9**(5): 453-461.

Brandsma, D. and M. J. van den Bent (2009). "Pseudoprogression and pseudoresponse in the treatment of gliomas." Curr Opin Neurol **22**(6): 633-638.

Campbell, N. A. and J. B. Reece (2002). Biology. San Francisco, CA, Pearson, Benjamin Cummings.

Carneiro, I., N. Howard and EBSCOhost. (2011). Introduction to epidemiology. Understanding public health series. Maidenhead, Berkshire ; New York, Open University Press,**:** electronic text.

Carpenter, M. B. and J. Sutin (1983). Human neuroanatomy. Baltimore, Williams & Wilkins.

Carr, D. H., J. Brown, G. M. Bydder, H. J. Weinmann, U. Speck, D. J. Thomas and I. R. Young (1984). "Intravenous chelated gadolinium as a contrast agent in NMR imaging of cerebral tumours." Lancet **1**(8375): 484-486.

Chen, W., T. Cloughesy, N. Kamdar, N. Satyamurthy, M. Bergsneider, L. Liau, P. Mischel, J. Czernin, M. E. Phelps and D. H. Silverman (2005). "Imaging proliferation in brain tumors with 18F-FLT PET: comparison with 18F-FDG." J Nucl Med **46**(6): 945-952.

Chen, W., S. Delaloye, D. H. Silverman, C. Geist, J. Czernin, J. Sayre, N. Satyamurthy, W. Pope, A. Lai, M. E. Phelps and T. Cloughesy (2007). "Predicting treatment response of malignant gliomas to bevacizumab and irinotecan by imaging proliferation with [18F] fluorothymidine positron emission tomography: a pilot study." J Clin Oncol **25**(30): 4714-4721.

Chien, D. T., S. Bahri, A. K. Szardenings, J. C. Walsh, F. Mu, M. Y. Su, W. R. Shankle, A. Elizarov and H. C. Kolb (2013). "Early clinical PET imaging results with the novel PHF-tau radioligand [F-18]-T807." J Alzheimers Dis **34**(2): 457-468.

Cipolla, M. (2009). The Cerebral Circulation. San Rafael, Biota Publishing.

De Santi, S., M. J. de Leon, H. Rusinek, A. Convit, C. Y. Tarshish, A. Roche, W. H. Tsui, E. Kandil, M. Boppana, K. Daisley, G. J. Wang, D. Schlyer and J. Fowler (2001). "Hippocampal formation glucose metabolism and volume losses in MCI and AD." Neurobiol Aging **22**(4): 529-539.

Deisenhammer, F., F. Sellebjerg, C. E. Teunissen and H. Tumani (2015). Cerebrospinal Fluid in Clinical Neurology Switzerland, Springer.

Delbeke, D., R. E. Coleman, M. J. Guiberteau, M. L. Brown, H. D. Royal, B. A. Siegel, D. W. Townsend, L. L. Berland, J. A. Parker, K. Hubner, M. G. Stabin, G. Zubal, M. Kachelriess, V. Cronin and S. Holbrook (2006). "Procedure guideline for tumor imaging with 18F-FDG PET/CT 1.0." J Nucl Med **47**(5): 885-895.

Deloitte Access Economics (2011). Dementia Across Australia: 2011-2050.

Diri, B. and S. Albayrak (2008). "Visualization and analysis of classifiers performance in multi-class medical data." Expert Systems with Applications **34**(1): 628-634.

Efron, B. and R. Tibshirani (1993). An introduction to the bootstrap. New York, Chapman & Hall.

Ellis, K. A., A. I. Bush, D. Darby, D. De Fazio, J. Foster, P. Hudson, N. T. Lautenschlager, N. Lenzo, R. N. Martins, P. Maruff, C. Masters, A. Milner, K. Pike, C. Rowe, G. Savage, C. Szoeke, K. Taddei, V. Villemagne, M. Woodward, D. Ames and A. R. Group (2009). "The Australian Imaging, Biomarkers and Lifestyle (AIBL) study of aging: methodology and baseline characteristics of 1112 individuals recruited for a longitudinal study of Alzheimer's disease." Int Psychogeriatr **21**(4): 672-687.

Evans, A. C., A. L. Janke, D. L. Collins and S. Baillet (2012). "Brain templates and atlases." Neuroimage **62**(2): 911-922.

Fischl, B., D. H. Salat, E. Busa, M. Albert, M. Dieterich, C. Haselgrove, A. van der Kouwe, R. Killiany, D. Kennedy, S. Klaveness, A. Montillo, N. Makris, B. Rosen and A. M. Dale (2002). "Whole brain segmentation: automated labeling of neuroanatomical structures in the human brain." Neuron **33**(3): 341-355.

Folstein, M. F., S. E. Folstein and P. R. McHugh (1975). ""Mini-mental state". A practical method for grading the cognitive state of patients for the clinician." J Psychiatr Res **12**(3): 189-198.

Fortin, D. (2011). Fischer/F98 Glioma Model: Methodology. Gliomas:Glioblastoma (Part 2) M. A. Hayat, Springer**:** 349-361.

Fox, N. C. and P. A. Freeborough (1997). "Brain atrophy progression measured from registered serial MRI: validation and application to Alzheimer's disease." J Magn Reson Imaging **7**(6): 1069-1075.

Friston, K. J. (2007). Statistical parametric mapping : the analysis of funtional brain images. Amsterdam ; Boston, Elsevier/Academic Press.

Fromm, H. J. and M. Hargrove (2012). Essentials of biochemistry. Berlin ; New York, Springer**:** xviii, 364 p.

Gardner, E. D., D. J. Gray and R. O'Rahilly (1975). Anatomy: a regional study of human structure. Philadelphia, USA, W.B. Saunders.

Gjedde, A. (2001). Physiological imaging of the brain with PET, Academic Press.

Gray, H. and W. H. Lewis (1918). Anatomy of the human body. Philadelphia and New York,, Lea & Febiger.

Gulyas, B. and C. Halldin (2012). "New PET radiopharmaceuticals beyond FDG for brain tumor imaging." Q J Nucl Med Mol Imaging **56**(2): 173-190.

Hayat, M. A. (2011). Gliomas:Glioblastoma (Part 1) Tumors of the central nervous system, Springer.

Herholz, K., S. F. Carter and M. Jones (2007). "Positron emission tomography imaging in dementia." Br J Radiol **80 Spec No 2**: S160-167.

Herholz, K., T. Holzer, B. Bauer, R. Schroder, J. Voges, R. I. Ernestus, G. Mendoza, G. Weber-Luxenburger, J. Lottgen, A. Thiel, K. Wienhard and W. D. Heiss (1998). "11C-methionine PET for differential diagnosis of low-grade gliomas." Neurology **50**(5): 1316-1322.

Herholz, K., L. W. Kracht and W. D. Heiss (2003). "Monitoring the effect of chemotherapy in a mixed glioma by C-11-methionine PET." J Neuroimaging **13**(3): 269-271.

Hoeben, B. A., E. G. Troost, P. N. Span, C. M. van Herpen, J. Bussink, W. J. Oyen and J. H. Kaanders (2013). "18F-FLT PET during radiotherapy or chemoradiotherapy in head and neck squamous cell carcinoma is an early predictor of outcome." J Nucl Med **54**(4): 532-540.

Hyman, B. T., C. H. Phelps, T. G. Beach, E. H. Bigio, N. J. Cairns, M. C. Carrillo, D. W. Dickson, C. Duyckaerts, M. P. Frosch, E. Masliah, S. S. Mirra, P. T. Nelson, J. A. Schneider, D. R. Thal, B. Thies, J. Q. Trojanowski, H. V. Vinters and T. J. Montine (2012). "National Institute on Aging-Alzheimer's Association guidelines for the neuropathologic assessment of Alzheimer's disease." Alzheimers Dement **8**(1): 1-13.

Hyman, B. T., G. W. Van Hoesen, K. Beyreuther and C. L. Masters (1989). "A4 amyloid protein immunoreactivity is present in Alzheimer's disease neurofibrillary tangles." Neurosci Lett **101**(3): 352-355.

Jack, C. R., Jr., R. C. Petersen, Y. C. Xu, S. C. Waring, P. C. O'Brien, E. G. Tangalos, G. E. Smith, R. J. Ivnik and E. Kokmen (1997). "Medial temporal atrophy on MRI in normal aging and very mild Alzheimer's disease." Neurology **49**(3): 786-794.

Jacobs, A. H., A. Thomas, L. W. Kracht, H. Li, C. Dittmar, G. Garlip, N. Galldiks, J. C. Klein, J. Sobesky, R. Hilker, S. Vollmar, K. Herholz, K. Wienhard and W. D. Heiss (2005). "18F-fluoro-L-thymidine and 11C-methylmethionine as markers of increased transport and proliferation in brain tumors." J Nucl Med **46**(12): 1948-1958.

Jansen, N. L., B. Suchorska, V. Wenter, C. Schmid-Tannwald, A. Todica, S. Eigenbrod, M. Niyazi, J. C. Tonn, P. Bartenstein, F. W. Kreth and C. la Fougere (2015). "Prognostic significance of dynamic 18F-FET PET in newly diagnosed astrocytic high-grade glioma." J Nucl Med **56**(1): 9-15.

Jenkinson, M., P. Bannister, M. Brady and S. Smith (2002). "Improved optimization for the robust and accurate linear registration and motion correction of brain images." Neuroimage **17**(2): 825-841.

Kadir, A., O. Almkvist, A. Forsberg, A. Wall, H. Engler, B. Langstrom and A. Nordberg (2012). "Dynamic changes in PET amyloid and FDG imaging at different stages of Alzheimer's disease." Neurobiol Aging **33**(1): 198 e191-114.

Kaplan, E. L. and P. Meier (1958). "Nonparametric estimation from incomplete observations." Journal of the American statistical association **53**(282): 457-481.

Kawai, N., Y. Nishiyama and T. Tamiya (2011). Newly Diagnosed Glioma: Diagnosis Using Positron Emission Tomography with Methionine and Fuorothymidine. Gliomas:Glioblastoma (Part 2) M. A. Hayat, Springer.

Kelloff, G. J., J. M. Hoffman, B. Johnson, H. I. Scher, B. A. Siegel, E. Y. Cheng, B. D. Cheson, J. O'Shaughnessy, K. Z. Guyton, D. A. Mankoff, L. Shankar, S. M. Larson, C. C. Sigman, R. L. Schilsky and D. C. Sullivan (2005). "Progress and promise of FDG-PET imaging for cancer patient management and oncologic drug development." Clin Cancer Res **11**(8): 2785-2808.

Kinahan, P., D. Clunie, R. Boellaard, M. Casey, P. E. Christian, P. E. Cole, S. DeBruin, J. M. Hoffman, S. Kohlmyer, P. Maniawski, D. Nelson, E. S. Perlman, L. X. Shao, J. G. Wolodzko, J. Yap and B. Zimmerman. (2012, 2012/09/28). "Vendor-neutral pseudo-code for SUV calculation." from http://qibawiki.rsna.org/index.php?title=Standardized_Uptake_Value_%28SUV%29.

Kracht, L. W., M. Friese, K. Herholz, R. Schroeder, B. Bauer, A. Jacobs and W. D. Heiss (2003). "Methyl-[11C]- l-methionine uptake as measured by positron emission tomography correlates to microvessel density in patients with glioma." Eur J Nucl Med Mol Imaging **30**(6): 868-873.

Kubota, K., M. Itoh, K. Ozaki, S. Ono, M. Tashiro, K. Yamaguchi, T. Akaizawa, K. Yamada and H. Fukuda (2001). "Advantage of delayed whole-body FDG-PET imaging for tumour detection." Eur J Nucl Med **28**(6): 696-703.

Lee, V. M., B. J. Balin, L. Otvos, Jr. and J. Q. Trojanowski (1991). "A68: a major subunit of paired helical filaments and derivatized forms of normal Tau." Science **251**(4994): 675-678.

Lombardo, S. and U. Maskos (2015). "Role of the nicotinic acetylcholine receptor in Alzheimer's disease pathology and treatment." Neuropharmacology **96**(Pt B): 255-262.

Lopez-Raton, M., M. X. Rodriguez-Alvarez, C. C. Suarez and F. Sampedro, G. (2014). "OptimalCutpoints: An R Package for Selecting Optimal Cutpoints in Diagnostic Tests." Journal of Statistical Software **61**(8): 1-36.

Lu, L. C. and J. Bludau (2011). Alzheimer's disease. Biographies of disease. Santa Barbara, Calif., Greenwood**:** xii, 143 p.

Luo, J. and C. Xiong (2012). "DiagTest3Grp: An R Package for Analyzing Diagnostic Tests with Three Ordinal Groups." J Stat Softw **51**(3): 1-24.

Luo, J. and C. Xiong (2013). "Youden index and Associated Cut-points for Three Ordinal Diagnostic Groups." Commun Stat Simul Comput **42**(6): 1213-1234.

Matthies, A., M. Hickeson, A. Cuchiara and A. Alavi (2002). "Dual time point 18F-FDG PET for the evaluation of pulmonary nodules." J Nucl Med **43**(7): 871-875.

McKhann, G. M., D. S. Knopman, H. Chertkow, B. T. Hyman, C. R. Jack, Jr., C. H. Kawas, W. E. Klunk, W. J. Koroshetz, J. J. Manly, R. Mayeux, R. C. Mohs, J. C. Morris, M. N. Rossor, P. Scheltens, M. C. Carrillo, B. Thies, S. Weintraub and C. H. Phelps (2011). "The diagnosis of dementia due to Alzheimer's disease: recommendations from the National Institute on Aging-Alzheimer's Association workgroups on diagnostic guidelines for Alzheimer's disease." Alzheimers Dement **7**(3): 263-269.

Mesulam, M. M. and M. Asuncion Moran (1987). "Cholinesterases within neurofibrillary tangles related to age and Alzheimer's disease." Ann Neurol **22**(2): 223-228.

Minoshima, S., K. A. Frey, N. L. Foster and D. E. Kuhl (1995). "Preserved pontine glucose metabolism in Alzheimer disease: a reference region for functional brain image (PET) analysis." Journal of computer assisted tomography **19**(4): 541-547.

Minoshima, S., B. Giordani, S. Berent, K. A. Frey, N. L. Foster and D. E. Kuhl (1997). "Metabolic reduction in the posterior cingulate cortex in very early Alzheimer's disease." Ann Neurol **42**(1): 85-94.

Miyagawa, T., T. Oku, H. Uehara, R. Desai, B. Beattie, J. Tjuvajev and R. Blasberg (1998). ""Facilitated" amino acid transport is upregulated in brain tumors." J Cereb Blood Flow Metab **18**(5): 500-509.

Molloy, D. W. and T. I. Standish (1997). "A guide to the standardized Mini-Mental State Examination." Int Psychogeriatr **9 Suppl 1**: 87-94; discussion 143-150.

Morra, J. H., Z. Tu, L. G. Apostolova, A. E. Green, C. Avedissian, S. K. Madsen, N. Parikshak, X. Hua, A. W. Toga, C. R. Jack, Jr., N. Schuff, M. W. Weiner, P. M. Thompson and I. Alzheimer's Disease Neuroimaging (2009). "Automated 3D mapping of hippocampal atrophy and its clinical correlates in 400 subjects with Alzheimer's disease, mild cognitive impairment, and elderly controls." Hum Brain Mapp **30**(9): 2766-2788.

Morris, J. C. (1993). "The Clinical Dementia Rating (CDR): current version and scoring rules." Neurology **43**(11): 2412-2414.

Mosconi, L., W. H. Tsui, S. De Santi, J. Li, H. Rusinek, A. Convit, Y. Li, M. Boppana and M. J. de Leon (2005). "Reduced hippocampal metabolism in MCI and AD: automated FDG-PET image analysis." Neurology **64**(11): 1860-1867.

Mueller, S. G., M. W. Weiner, L. J. Thal, R. C. Petersen, C. R. Jack, W. Jagust, J. Q. Trojanowski, A. W. Toga and L. Beckett (2005). "Ways toward an early diagnosis in Alzheimer's disease: the Alzheimer's Disease Neuroimaging Initiative (ADNI)." Alzheimers Dement **1**(1): 55-66.

Munch-Petersen, B., L. Cloos, H. K. Jensen and G. Tyrsted (1995). "Human thymidine kinase 1. Regulation in normal and malignant cells." Adv Enzyme Regul **35**: 69-89.

Muzi, M., A. M. Spence, F. O'Sullivan, D. A. Mankoff, J. M. Wells, J. R. Grierson, J. M. Link and K. A. Krohn (2006). "Kinetic analysis of 3'-deoxy-3'-18F-fluorothymidine in patients with gliomas." J Nucl Med **47**(10): 1612-1621.

Nakas, C. T., T. A. Alonzo and C. T. Yiannoutsos (2010). "Accuracy and cut-off point selection in three-class classification problems using a generalization of the Youden index." Stat Med **29**(28): 2946-2955.

Nestor, P. J., P. Scheltens and J. R. Hodges (2004). "Advances in the early detection of Alzheimer's disease." Nat Med **10 Suppl**: S34-41.

Okubo, S., H. N. Zhen, N. Kawai, Y. Nishiyama, R. Haba and T. Tamiya (2010). "Correlation of L-methyl-11C-methionine (MET) uptake with L-type amino acid transporter 1 in human gliomas." J Neurooncol **99**(2): 217-225.

Olazaran, J., B. Reisberg, L. Clare, I. Cruz, J. Pena-Casanova, T. Del Ser, B. Woods, C. Beck, S. Auer, C. Lai, A. Spector, S. Fazio, J. Bond, M. Kivipelto, H. Brodaty, J. M. Rojo, H. Collins, L. Teri, M. Mittelman, M. Orrell, H. H. Feldman and R. Muniz (2010). "Nonpharmacological therapies in Alzheimer's disease: a systematic review of efficacy." Dement Geriatr Cogn Disord **30**(2): 161-178.

Oldendorf, W. H. (1971). "Brain uptake of radiolabeled amino acids, amines, and hexoses after arterial injection." Am J Physiol **221**(6): 1629-1639.

Padma, M. V., S. Said, M. Jacobs, D. R. Hwang, K. Dunigan, M. Satter, B. Christian, J. Ruppert, T. Bernstein, G. Kraus and J. C. Mantil (2003). "Prediction of pathology and survival by FDG PET in gliomas." J Neurooncol **64**(3): 227-237.

Patenaude, B., S. M. Smith, D. N. Kennedy and M. Jenkinson (2011). "A Bayesian model of shape and appearance for subcortical brain segmentation." Neuroimage **56**(3): 907-922.

Pelizzari, C. A., G. T. Chen, D. R. Spelbring, R. R. Weichselbaum and C. T. Chen (1989). "Accurate three-dimensional registration of CT, PET, and/or MR images of the brain." J Comput Assist Tomogr **13**(1): 20-26.

Perl, D. P. (2010). "Neuropathology of Alzheimer's disease." Mt Sinai J Med **77**(1): 32-42.

Perry, G., R. Friedman, G. Shaw and V. Chau (1987). "Ubiquitin is detected in neurofibrillary tangles and senile plaque neurites of Alzheimer disease brains." Proc Natl Acad Sci U S A **84**(9): 3033-3036.

Peto, R. and J. Peto (1972). "Asymptotically efficient rank invariant test procedures." Journal of the Royal Statistical Society. Series A (General): 185-207.

Popperl, G., C. Gotz, W. Rachinger, F. J. Gildehaus, J. C. Tonn and K. Tatsch (2004). "Value of O-(2-[18F]fluoroethyl)- L-tyrosine PET for the diagnosis of recurrent glioma." Eur J Nucl Med Mol Imaging **31**(11): 1464-1470.

R Core Team (2015). R: A Language and Environment for Statistical Computing. Vienna, Austria, R Foundation for Statistical Computing.

Rasey, J. S., J. R. Grierson, L. W. Wiens, P. D. Kolb and J. L. Schwartz (2002). "Validation of FLT uptake as a measure of thymidine kinase-1 activity in A549 carcinoma cells." J Nucl Med **43**(9): 1210-1217.

Reisberg, B., S. H. Ferris, M. J. de Leon and T. Crook (1982). "The Global Deterioration Scale for assessment of primary degenerative dementia." Am J Psychiatry **139**(9): 1136-1139.

Ribom, D., A. Eriksson, M. Hartman, H. Engler, A. Nilsson, B. Langstrom, H. Bolander, M. Bergstrom and A. Smits (2001). "Positron emission tomography (11)C-methionine and survival in patients with low-grade gliomas." Cancer **92**(6): 1541-1549.

Ricci, P. E., J. P. Karis, J. E. Heiserman, E. K. Fram, A. N. Bice and B. P. Drayer (1998). "Differentiating recurrent tumor from radiation necrosis: time for re-evaluation of positron emission tomography?" AJNR Am J Neuroradiol **19**(3): 407-413.

Ridha, B. H., J. Barnes, J. W. Bartlett, A. Godbolt, T. Pepple, M. N. Rossor and N. C. Fox (2006). "Tracking atrophy progression in familial Alzheimer's disease: a serial MRI study." Lancet Neurol **5**(10): 828-834.

Ringman, J. M., W. Pope and N. Salamon (2010). "Insensitivity of visual assessment of hippocampal atrophy in familial Alzheimer's disease." J Neurol **257**(5): 839-842.

Robin, X., N. Turck, A. Hainard, N. Tiberti, F. Lisacek, J. C. Sanchez and M. Muller (2011). "pROC: an open-source package for R and S+ to analyze and compare ROC curves." BMC Bioinformatics **12**: 77.

Roche, A., G. Malandain, X. Pennec and N. Ayache (1998). The correlation ratio as a new similarity measure for multimodal image registration. Medical Image Computing and Computer-Assisted Intervention—MICCAI'98, Springer**:** 1115-1124.

Salander, P., A. T. Bergenheim, K. Hamberg and R. Henriksson (1999). "Pathways from symptoms to medical care: a descriptive study of symptom development and obstacles to early diagnosis in brain tumour patients." Fam Pract **16**(2): 143-148.

Salomone, S., F. Caraci, G. M. Leggio, J. Fedotova and F. Drago (2012). "New pharmacological strategies for treatment of Alzheimer's disease: focus on disease modifying drugs." Br J Clin Pharmacol **73**(4): 504-517.

Saunders, N. R., C. J. Ek, M. D. Habgood and K. M. Dziegielewska (2008). "Barriers in the brain: a renaissance?" Trends Neurosci **31**(6): 279-286.

Schneider, C. A., W. S. Rasband and K. W. Eliceiri (2012). "NIH Image to ImageJ: 25 years of image analysis." Nat Methods **9**(7): 671-675.

Schott, J. M., S. L. Price, C. Frost, J. L. Whitwell, M. N. Rossor and N. C. Fox (2005). "Measuring atrophy in Alzheimer disease: a serial MRI study over 6 and 12 months." Neurology **65**(1): 119-124.

Schwartz, L. M., S. Woloshin, H. C. Sox, B. Fischhoff and H. G. Welch (2000). "US women's attitudes to false-positive mammography results and detection of ductal carcinoma in situ: cross-sectional survey." West J Med **173**(5): 307-312.

Schwarzenberg, J., J. Czernin, T. F. Cloughesy, B. M. Ellingson, W. B. Pope, C. Geist, M. Dahlbom, D. H. Silverman, N. Satyamurthy, M. E. Phelps and W. Chen (2012). "3'-deoxy-3'-18F-fluorothymidine PET and MRI for early survival predictions in patients with recurrent malignant glioma treated with bevacizumab." J Nucl Med **53**(1): 29-36.

Shelton, T. (2012). Alzheimer's Disease. New Delhi, Research World.

Siegel, G. J. and B. W. Agranoff (1999). Basic neurochemistry: molecular, cellular, and medical aspects, Lippincott Williams & Wilkins.

Silverman, D. H. and G. W. Small (2002). "Prompt identification of Alzheimer's disease with brain PET imaging of a woman with multiple previous diagnoses of other neuropsychiatric conditions." Am J Psychiatry **159**(9): 1482-1488.

Singhal, T., T. K. Narayanan, M. P. Jacobs, C. Bal and J. C. Mantil (2012). "11C-methionine PET for grading and prognostication in gliomas: a comparison study with 18F-FDG PET and contrast enhancement on MRI." J Nucl Med **53**(11): 1709-1715.

Smith, S. M. (2002). "Fast robust automated brain extraction." Hum Brain Mapp **17**(3): 143-155.

Smith, S. M., M. Jenkinson, M. W. Woolrich, C. F. Beckmann, T. E. Behrens, H. Johansen-Berg, P. R. Bannister, M. De Luca, I. Drobnjak, D. E. Flitney, R. K. Niazy, J. Saunders, J. Vickers, Y. Zhang, N. De Stefano, J. M. Brady and P. M. Matthews (2004). "Advances in functional and structural MR image analysis and implementation as FSL." Neuroimage **23 Suppl 1**: S208-219.

Spence, A. M., M. Muzi, J. M. Link, F. O'Sullivan, J. F. Eary, J. M. Hoffman, L. K. Shankar and K. A. Krohn (2009). "NCI-sponsored trial for the evaluation of safety and preliminary efficacy of 3'-deoxy-3'-[18F]fluorothymidine (FLT) as a marker of proliferation in patients with recurrent gliomas: preliminary efficacy studies." Mol Imaging Biol **11**(5): 343-355.

Sperling, R. A., P. S. Aisen, L. A. Beckett, D. A. Bennett, S. Craft, A. M. Fagan, T. Iwatsubo, C. R. Jack, Jr., J. Kaye, T. J. Montine, D. C. Park, E. M. Reiman, C. C. Rowe, E. Siemers, Y. Stern, K. Yaffe, M. C. Carrillo, B. Thies, M. Morrison-Bogorad, M. V. Wagster and C. H. Phelps (2011). "Toward defining the preclinical stages of Alzheimer's disease: recommendations from the National Institute on

Aging-Alzheimer's Association workgroups on diagnostic guidelines for Alzheimer's disease." <u>Alzheimers Dement</u> **7**(3): 280-292.

Stupp, R., W. P. Mason, M. J. van den Bent, M. Weller, B. Fisher, M. J. Taphoorn, K. Belanger, A. A. Brandes, C. Marosi, U. Bogdahn, J. Curschmann, R. C. Janzer, S. K. Ludwin, T. Gorlia, A. Allgeier, D. Lacombe, J. G. Cairncross, E. Eisenhauer, R. O. Mirimanoff, R. European Organisation for, T. Treatment of Cancer Brain, G. Radiotherapy and G. National Cancer Institute of Canada Clinical Trials (2005). "Radiotherapy plus concomitant and adjuvant temozolomide for glioblastoma." <u>N Engl J Med</u> **352**(10): 987-996.

The National Institute on Aging (1997). "Consensus recommendations for the postmortem diagnosis of Alzheimer's disease. The National Institute on Aging, and Reagan Institute Working Group on Diagnostic Criteria for the Neuropathological Assessment of Alzheimer's Disease." <u>Neurobiol Aging</u> **18**(4 Suppl): S1-2.

Thompson, P. and A. W. Toga (1996). <u>Visualization and mapping of anatomic abnormalities using a probabilistic brain atlas based on random fluid transformations</u>. Visualization in Biomedical Computing, Springer.

Tripathi, M., R. Sharma, R. Varshney, A. Jaimini, J. Jain, M. M. Souza, J. Bal, S. Pandey, N. Kumar, A. K. Mishra and A. Mondal (2012). "Comparison of F-18 FDG and C-11 methionine PET/CT for the evaluation of recurrent primary brain tumors." <u>Clin Nucl Med</u> **37**(2): 158-163.

Van Laere, K., S. Ceyssens, F. Van Calenbergh, T. de Groot, J. Menten, P. Flamen, G. Bormans and L. Mortelmans (2005). "Direct comparison of 18F-FDG and 11C-methionine PET in suspected recurrence of glioma: sensitivity, inter-observer variability and prognostic value." <u>Eur J Nucl Med Mol Imaging</u> **32**(1): 39-51.

Vander Borght, T., S. Asenbaum, P. Bartenstein, C. Halldin, Ö. Kapuco, K. Van Laere, A. Varrone and K. Tatsch (2010). Brain Tumour Imaging: European Association of Nuclear Medicine Procedure Guidelines. <u>Brain cancer</u>
M. A. Hayat, Springer.

Vanderhoek, M., S. B. Perlman and R. Jeraj (2012). "Impact of the definition of peak standardized uptake value on quantification of treatment response." <u>J Nucl Med</u> **53**(1): 4-11.

Varrone, A., S. Asenbaum, T. Vander Borght, J. Booij, F. Nobili, K. Nagren, J. Darcourt, O. L. Kapucu, K. Tatsch, P. Bartenstein, K. Van Laere and C. European Association of Nuclear Medicine Neuroimaging (2009). "EANM procedure guidelines for PET brain imaging using [18F]FDG, version 2." <u>Eur J Nucl Med Mol Imaging</u> **36**(12): 2103-2110.

Villain, N., B. Desgranges, F. Viader, V. de la Sayette, F. Mezenge, B. Landeau, J. C. Baron, F. Eustache and G. Chetelat (2008). "Relationships between hippocampal

atrophy, white matter disruption, and gray matter hypometabolism in Alzheimer's disease." J Neurosci **28**(24): 6174-6181.

Viola, P. and W. M. Wells Iii (1997). "Alignment by Maximization of Mutual Information." International Journal of Computer Vision **24**(2): 137-154.

Vlassenko, A. G., T. L. Benzinger and J. C. Morris (2012). "PET amyloid-beta imaging in preclinical Alzheimer's disease." Biochim Biophys Acta **1822**(3): 370-379.

Wahl, R. L., H. Jacene, Y. Kasamon and M. A. Lodge (2009). "From RECIST to PERCIST: Evolving Considerations for PET response criteria in solid tumors." J Nucl Med **50 Suppl 1**: 122S-150S.

Warburg, O. (1956). "On the origin of cancer cells." Science **123**(3191): 309-314.

Waxman, S. G. (2013). Clinical Neuroanatomy, Lange Medical Books/McGraw-Hill, Medical Pub. Division.

Wechsler, D. (1987). WMS-R: Wechsler Memory Scale-Revised : Manual, Harcourt Brace Jovanovich.

Wirth, T., H. Samaranayake and S. Ylä-Herttuala (2011). Glioblastoma Multiforme: Use of Adenoviral Vectors. Tumors of the Central Nervous System Volume 2 Gliomas: Glioblastoma (Part 2). M. A. Hayat, Springer. **2:** 13.

Wisniewski, K., G. A. Jervis, R. C. Moretz and H. M. Wisniewski (1979). "Alzheimer neurofibrillary tangles in diseases other than senile and presenile dementia." Ann Neurol **5**(3): 288-294.

Youden, W. J. (1950). "Index for rating diagnostic tests." Cancer **3**(1): 32-35.

Zheng, W. and A. Chodobski (2005). The Blood-Cerebrospinal Fluid Barrier. Boca Raton, FL, Taylor & Francis Group.

8 Appendices

8.1 Appendix 1: SUV Conversion Factor Script

This Matlab script was written by Mr Ricki Nezich, Medical Physicist, Medical Technology and Physics Sir Charles Gairdner Hospital, Nedlands WA.

```
% suvFactorTable looks at all of the folders beneath the 'baseFolder'
% containing PET Dicom series, and creates an Excel file with a table of
% SUV conversion factors for each series. The Excel file is saved in the
% 'baseFolder'.

function suvFactorTable(baseFolder)
  % Preallocate Excel output cell array.
  PRE_CELL_ROWS = 1000;
  outputXls = cell(PRE_CELL_ROWS, 2);
  outIndx = 0;

  % Get all folders below 'baseFolder'.
  disp('Collecting folders...');
  baseFolder = strrep(baseFolder, '\', '/');
  fList = FileList(baseFolder);
  fList.collectSubFolders();
  folders = fList.getFileNames();

  % Process each folder.
  for i = 1:length(folders)
    % Get a vector of files contained in the folder.
    folderName = strrep(folders{i}, '\', '/');
    FileStruct = dir(folderName);

    % Calculate the SUV conversion factor from the first valid Dicom
    % image in the series.
    for j = 1:length(FileStruct)
      fileName = FileStruct(j).name;
      if length(fileName) >= 2 && strcmp(fileName(1:2), 'IM')
        try
          suvFactor = getSuvFactor(fullfile(folderName, fileName));
        catch exception
          disp(exception.message);
          continue;
        end
        if suvFactor == 0
          break;
        end

        outIndx = outIndx + 1;

        % Get the patient ID
        patID = sscanf(folderName, strcat(baseFolder, '/%6c/%*s'));
        fprintf('%s\nSUV factor: %f\n\n', fullfile(folderName, fileName), suvFactor);

        % Write the information to the output cell array.
        outputXls{outIndx, 1} = patID;
```

```matlab
            [~, seriesName, ~] = fileparts(folderName);
            outputXls{outIndx, 2} = seriesName;
            outputXls{outIndx, 3} = suvFactor;
            break;
          end
        end
    end

    % Write data to Excel file.
    xlswrite(fullfile(baseFolder, 'SuvFactors'), outputXls(1:outIndx, :));
end

% Get the names of files in and below a given folder.
classdef FileList < handle
  properties (SetAccess = private, GetAccess = public)
    dirName
    % fileNames is a cell vector holding file names.
    fileNames
    nFiles = 0
  end
  properties (Constant, GetAccess = private)
    % Pre-allocated fileNames length.
    FILENAMES_LENGTH = 100
  end
  methods (Access = public)
    % Constructor method.
    function fList = FileList(dirName)
      if dirName(end) == '\' % Handle the case for a root directory.
        dirName = dirName(1:end-1);
      end
      fList.dirName = dirName;
      fList.clear();
    end

    % Clear the fileNames collected.
    function clear(fList)
      fList.nFiles = 0;
      fList.fileNames = cell(fList.FILENAMES_LENGTH, 1);
    end

    % Collect file names found in the dirName.
    function collectDirFiles(fList)
      fList.clear();
      dirStruct = dir(fList.dirName);
      for i = 1:numel(dirStruct);
        fileName = dirStruct(i).name;
        if dirStruct(i).isdir || fileName(1) == '.'
          continue;
        else
          % Add file to the guiList.
          fullName = strcat(fList.dirName, '\', fileName);
          fList.addFile(fullName);
        end
      end
    end

    % Return the collected file names.
    function files = getFileNames(fList)
      if fList.nFiles > 0
        files = fList.fileNames(1:fList.nFiles);
      else
        files = {};
      end
    end

    % Collect file names found in and below the dirName folder.
    function collectSubFiles(fList)
      fList.clear();
      fList.addFilesRecursively(fList.dirName);
    end

    % Collect folders found in and below the dirName folder.
    function collectSubFolders(fList)
      fList.clear();
      fList.addFoldersRecursively(fList.dirName);
    end
```

116

```matlab
      end

      methods (Access = private)
         % Add a file to fileNames.
         function addFile(fList, fullName)
            fList.nFiles = fList.nFiles + 1;
            if fList.nFiles > length(fList.fileNames)
               fList.fileNames = cat(1, fList.fileNames, cell(fList.FILENAMES_LENGTH, 1));
            end
            fList.fileNames{fList.nFiles} = fullName;
         end

         % Go through nested folders recursively and store the file names.
         function addFilesRecursively(fList, subDirName)
            dirStruct = dir(subDirName);
            for i = 1:numel(dirStruct)
               shortName = dirStruct(i).name;
               fullName = strcat(subDirName, '\', shortName);
               % If a directory is encountered, then act recursively.
               if dirStruct(i).isdir
                  if strcmp(shortName, '.') || strcmp(shortName, '..')
                     continue;
                  end
                  fList.addFilesRecursively(fullName);
               % If a file is encountered, then add it to fileNames.
               else
                  if shortName(1) == '.'
                     continue;
                  end
                  fList.addFile(fullName);
               end
            end
         end

         % Go through nested folders recursively and store their names.
         function addFoldersRecursively(fList, subDirName)
            dirStruct = dir(subDirName);
            for i = 1:numel(dirStruct)
               shortName = dirStruct(i).name;
               fullName = strcat(subDirName, '\', shortName);
               % If a directory is encountered, then act recursively.
               if dirStruct(i).isdir
                  if strcmp(shortName, '.') || strcmp(shortName, '..')
                     continue;
                  end
                  fList.addFile(fullName);
                  fList.addFoldersRecursively(fullName);
               % If a file is encountered, then add it to fileNames.
               else
                  continue;
               end
            end
         end
      end
   end

% Calculate the SUV factor for a PET image series, represented by the Dicom
% slice 'dcmFileName'.

function suvFactor = getSuvFactor(dcmFileName)
   % Get Dicom header structure.
   try
      dcmInfo = dicominfo(dcmFileName);
   catch %#ok<CTCH>
      suvFactor = 0;
      return;
   end

   if ~strcmp(dcmInfo.Modality, 'PT')
      suvFactor = 0;
      return;
   end

   if ~strcmp(dcmInfo.DecayCorrection, 'START')
      error('Image is not decay corrected to START');
   end
```

```
    % Get relevant header fields.
    halfLifeSecs = dcmInfo.RadiopharmaceuticalInformationSequence.Item_1.RadionuclideHalfLife;
    injectionTimeStr = dcmInfo.RadiopharmaceuticalInformationSequence.Item_1.RadiopharmaceuticalStartTime;
    scanStartTimeStr = dcmInfo.SeriesTime;
    injectedDoseBq = dcmInfo.RadiopharmaceuticalInformationSequence.Item_1.RadionuclideTotalDose;
    patientWeight = dcmInfo.PatientWeight;

    % Get time between injection and scan start.
    injectionTimeVec = datevec(datenum(injectionTimeStr, 'HHMMSS'));
    scanStartTimeVec = datevec(datenum(scanStartTimeStr, 'HHMMSS'));
    preScanTimeSecs = (scanStartTimeVec - injectionTimeVec) * [0; 0; 0; 3600; 60; 1];

    % Calculate SUV.
    preScanDecayFactor = exp(log(2) / halfLifeSecs * preScanTimeSecs);
    suvFactor = preScanDecayFactor * patientWeight / injectedDoseBq * 1000;
end
```

8.2 Appendix 2: SUV PEAK Location Script

```
# Python script for sweeping through an assigned volume and finding the highest average voxel number is a cubic mm sphere
from nifti import *
from numpy import *
#import pdb
#pdb.set_trace()
#import subprocess
#import os
#from decimal import *
study_participant = "GL33MO"
CMET_10 = NiftiImage('D:/VM_shared/numpy/GL33MO_CMET_PET_10_SUV_2_MNI_T2_mutualinfo.nii.gz')
CMET_20 = NiftiImage('D:/VM_shared/numpy/GL33MO_CMET_PET_20_SUV_2_MNI_T2_mutualinfo.nii.gz')
CMET_30 = NiftiImage('D:/VM_shared/numpy/GL33MO_CMET_PET_30_SUV_2_MNI_T2_mutualinfo.nii.gz')
CMET_40 = NiftiImage('D:/VM_shared/numpy/GL33MO_CMET_PET_40_SUV_2_MNI_T2_mutualinfo.nii.gz')

FLT_15 = NiftiImage('D:/VM_shared/numpy/GL33MO_FLT_PET_15_SUV_2_MNI_T2_mutualinfo.nii.gz')
FLT_75 = NiftiImage('D:/VM_shared/numpy/GL33MO_FLT_PET_75_SUV_2_MNI_T2_mutualinfo.nii.gz')

corner_mask = NiftiImage('D:/VM_shared/numpy/bottom_corner_mask.nii.gz')

cmet_images = [CMET_10, CMET_20, CMET_30, CMET_40]
flt_images = [FLT_15, FLT_75]


# bottom_corner.txt is the location of each voxel in a
# MNI 152 1mm template sized image that would constitute
# a 6mm sphere sitting in the "origin" corner

# read the input file into a list of lines of text
input_coords = open("D:/VM_shared/numpy/bottom_corner.txt", "r").readlines()
# now walk through that list, splitting each line in to 3 coordinates
# and converting each to an integer

sphere = [ [int(values[0]), int(values[1]), int(values[2])] for values in [aline.split() for aline in input_coords] ]
# sphere is now a list, each element of which is the (x,y,z) coo-rdinate of a voxel in the sphere.

#output = open("D:/VM_shared/numpy/bottom_corner.txt", "w")
#for x in range(0,20):
        #for y in range (0,20):
        #        for z in range (0,20):
        #                if corner_mask.data[z,y,x] == 1:
                                #print(z,y,x)
        #                        output.write("%s %s %s\n" % (z,y,x))
                                #print(corner_mask.data[z,y,x])

                                # instead of reading the 1cm sphere values in from a text file
                                # try running the previous bit of code and saving each datapoint as a variable or
something, then recalling for each iteration.


dict = {}
#-----------------------------------------------------CMET-----------------------------------------------------
for cmet_image in cmet_images:
        # specify a search volume for this individual
        cmet_x_min = 90; cmet_x_max = 131
        cmet_y_min = 124; cmet_y_max = 191
        cmet_z_min = 64; cmet_z_max = 145
        SUV_PEAK_list = list()
        SUV_PEAK_list_with_coords = list()

# move the sphere from bottom_corner.txt around all locations inside the search volume to get the average uptake at all points
        for x in range (cmet_x_min,cmet_x_max):
                for y in range (cmet_y_min,cmet_y_max):
                        for z in range (cmet_z_min,cmet_z_max):
                                voxel_count=0
                                for voxel in sphere:
                                        voxel_count=voxel_count+1
                                        x_coord = voxel[0] + z
                                        y_coord = voxel[1] + y
                                        z_coord = voxel[2] + x
                                        dict["current_voxel_number" + str(voxel_count)] =
cmet_image.data[x_coord, y_coord, z_coord]
```

```
                                                voxel_sum = dict["current_voxel_number" + str(voxel_count-0)] +
dict["current_voxel_number" + str(voxel_count-1)]
                                        for i in range(2,925):
                                                voxel_sum = dict["current_voxel_number" + str(voxel_count-i)] +
voxel_sum

                                        #print (str(voxel_count-924))
                                #print(voxel_sum)
                                SUV_PEAK = voxel_sum / 925

                                #print (x+6, y+6, z+6, SUV_PEAK)
                                SUV_PEAK_list.append(SUV_PEAK)
                                SUV_PEAK_list_with_coords.append(x+6)
                                SUV_PEAK_list_with_coords.append(y+6)
                                SUV_PEAK_list_with_coords.append(z+6)
                                SUV_PEAK_list_with_coords.append(SUV_PEAK)

        #find out what SUV_PEAK is, print out the value and the location of the sphere centre

        SUV_PEAK_value = max(SUV_PEAK_list)
        SUV_PEAK_big_list_location = SUV_PEAK_list_with_coords.index(SUV_PEAK_value)

        x_coordinate_list_location = SUV_PEAK_big_list_location-3
        x_coordinate_value = SUV_PEAK_list_with_coords[x_coordinate_list_location]

        y_coordinate_list_location = SUV_PEAK_big_list_location-2
        y_coordinate_value = SUV_PEAK_list_with_coords[y_coordinate_list_location]

        z_coordinate_list_location = SUV_PEAK_big_list_location-1
        z_coordinate_value = SUV_PEAK_list_with_coords[z_coordinate_list_location]

        #CMET_ = pet_image.filename[26:31]
        #time = pet_image.filename[35:37]

        CMET_ = cmet_image.filename[26:31]
        cmet_time = cmet_image.filename[35:37]


        print(study_participant, "%s%s " %(CMET_,cmet_time), 'SUV Peak Data' )
        print("coordinates: ", x_coordinate_value, y_coordinate_value, z_coordinate_value, " SUV_PEAK: ",
SUV_PEAK_value)
        print(' ')


        # write out text files of both lists

        with open("D:/VM_shared/numpy/%s_%s%s_SUV_PEAK_values_only.txt"
%(study_participant,CMET_,cmet_time), "w") as file:
                        for item in SUV_PEAK_list:
                                        print>>file, item

        with open("D:/VM_shared/numpy/%s_%s%s_SUV_PEAK_values_with_coords.txt"
%(study_participant,CMET_,cmet_time), "w") as file2:
                        for item2 in SUV_PEAK_list_with_coords:
                                        print>>file2, item2


#---------------------------------------------FLT-------------------------------------------------------------
for flt_image in flt_images:

        flt_x_min = 90; flt_x_max = 131
        flt_y_min = 124; flt_y_max = 191
        flt_z_min = 64; flt_z_max = 145
        SUV_PEAK_list = list()
        SUV_PEAK_list_with_coords = list()


        for x in range (flt_x_min,flt_x_max):
                for y in range (flt_y_min,flt_y_max):
                        for z in range (flt_z_min,flt_z_max):
                                voxel_count=0
                                for voxel in sphere:
                                        voxel_count=voxel_count+1
                                        x_coord = voxel[0] + z
                                        y_coord = voxel[1] + y
                                        z_coord = voxel[2] + x
```

```
                                                    dict["current_voxel_number" + str(voxel_count)] =
flt_image.data[x_coord, y_coord, z_coord]

                                voxel_sum = dict["current_voxel_number" + str(voxel_count-0)] +
dict["current_voxel_number" + str(voxel_count-1)]
                                for i in range(2,925):
                                        voxel_sum = dict["current_voxel_number" + str(voxel_count-i)] +
voxel_sum

                                        #print (str(voxel_count-924))
                                #print(voxel_sum)
                                SUV_PEAK = voxel_sum / 925

                                #print (x+6, y+6, z+6, SUV_PEAK)
                                SUV_PEAK_list.append(SUV_PEAK)
                                SUV_PEAK_list_with_coords.append(x+6)
                                SUV_PEAK_list_with_coords.append(y+6)
                                SUV_PEAK_list_with_coords.append(z+6)
                                SUV_PEAK_list_with_coords.append(SUV_PEAK)

                #find out what SUV_PEAK is, print out the value and the location of the sphere centre

                SUV_PEAK_value = max(SUV_PEAK_list)
                SUV_PEAK_big_list_location = SUV_PEAK_list_with_coords.index(SUV_PEAK_value)

                x_coordinate_list_location = SUV_PEAK_big_list_location-3
                x_coordinate_value = SUV_PEAK_list_with_coords[x_coordinate_list_location]

                y_coordinate_list_location = SUV_PEAK_big_list_location-2
                y_coordinate_value = SUV_PEAK_list_with_coords[y_coordinate_list_location]

                z_coordinate_list_location = SUV_PEAK_big_list_location-1
                z_coordinate_value = SUV_PEAK_list_with_coords[z_coordinate_list_location]

                #CMET_ = pet_image.filename[26:31]
                #time = pet_image.filename[35:37]

                FLT_ = flt_image.filename[26:30]
                flt_time = flt_image.filename[34:36]


                print(study_participant, "%s%s " %(FLT_,flt_time), 'SUV Peak Data' )
                print("coordinates: ", x_coordinate_value, y_coordinate_value, z_coordinate_value, " SUV_PEAK: ",
SUV_PEAK_value)
                print(' ')


                # write out text files of both lists

                with open("D:/VM_shared/numpy/%s_%s%s_SUV_PEAK_values_only.txt" %(study_participant,FLT_,flt_time),
"w") as file:
                                for item in SUV_PEAK_list:
                                                print>>file, item

                with open("D:/VM_shared/numpy/%s_%s%s_SUV_PEAK_values_with_coords.txt"
%(study_participant,FLT_,flt_time), "w") as file2:
                                for item2 in SUV_PEAK_list_with_coords:
                                                print>>file2, item2


# writing out nifti images showing the search area

for x in range (0,182):
                for y in range (0,218):
                                for z in range (0,182):

                                                CMET_10.data[z, y, x]=0

for x in range (cmet_x_min,cmet_x_max):
                for y in range (cmet_y_min,cmet_y_max):
                                for z in range (cmet_z_min,cmet_z_max):

                                                CMET_10.data[z, y, x]=1



CMET_ = CMET_10.filename[26:31]
```

```python
CMET_10.save('D:/VM_shared/numpy/%s_%sPERCIST_search_area.nii.gz' %(study_participant,CMET_))


for x in range (0,182):
        for y in range (0,218):
                for z in range (0,182):

                        FLT_15.data[z, y, x]=0

for x in range (flt_x_min,flt_x_max):
        for y in range (flt_y_min,flt_y_max):
                for z in range (flt_z_min,flt_z_max):

                        FLT_15.data[z, y, x]=1



FLT_ = FLT_15.filename[26:30]


FLT_15.save('D:/VM_shared/numpy/%s_%sPERCIST_search_area.nii.gz' %(study_participant,FLT_))


#output.write("%s %s %s\n" % (z,y,x))

#all_SUV_PEAK_values_with_coords = open("D:/VM_shared/numpy/CMET_10_SUV_PEAK_values_with_coords.txt", "w")
#all_SUV_PEAK_values_with_coords.write(SUV_PEAK_list_with_coords)




        #output = open("D:/VM_shared/numpy/corner_output.txt", "w")




        #subprocess.call(["fslview /usr/local/fsl/data/standard/MNI152_T1_2mm.nii.gz"])


#       flirt_command = 'flirt -in /usr/local/fsl/data/standard/MNI152_T1_2mm.nii.gz -out flirted_%s.nii.gz -ref
/usr/local/fsl/data/standard/MNI152_T1_1mm.nii.gz -dof 6 -v' % count
        #print(flirt_command)
#os.system()


        #flirt_command_2 = 'flirt -in /usr/local/fsl/data/standard/MNI152_T1_2mm.nii.gz -out flirted_%s.nii.gz -ref
/usr/local/fsl/data/standard/MNI152_T1_1mm.nii.gz -dof 6 -v -omat flirted_%s.mat' % (count, count2)
        #print(flirt_command_2)

        #os.system(flirt_command_2)
        #os.system("sh bash_script") # to run a bash script called bash_script
```

8.3 Appendix 3: Bootstrap Resampling Script

The bias corrected percentile method of bootstrap resampling used in this body of work was based on the description in (Efron and Tibshirani 1993).

The "Resampling stats in Excel" add in (http://www.resample.com/download-excel/) was used to create 1000 columns of numbers that represent bootstrap iterations of the data. This array was saved as a text file and then called into Matlab, where the following script was used to break it up into 1000 separate files:

```
for i = 1:1000
        filename = num2str(i)
        A = untitled(i,1:40)
        dlmwrite(['/mnt/hgfs/VM_shared/'filename'.txt'],A,'delimiter','','newline','pc')
end
```

These text files are then called by a perl script, which creates a mask based on each of the iterations by taking individual subject's hippocampal regions and summing them using the FSL routine *fslmaths*.

```perl
#!/usr/bin/perl -w
use strict;  # keep these magical incantations
$|++;                  # they make Perl work better ...

use File::Copy;


# get a list of text files in the iterations directory
my $iterationlisting = `ls iterations/*.txt`;

#print "Iteration listing:\n$iterationlisting";


my @iterationlist = split/\n/,$iterationlisting;

my $iterationNo = 1;
my $outputDir = "permutations";
my $maskDir = "FSL_masks";

foreach my $iterationFileName (@iterationlist) {
        print "Permutation $iterationNo\n";

        my $fh;
        open $fh, $iterationFileName or die "cannot open $iterationFileName\n";
        my $maskNumbers = <$fh>;
        chomp($maskNumbers);

        my @maskList = split(" ",$maskNumbers);

        my $iterationFileName = $outputDir."/p".$iterationNo.".nii.gz";
        my $maskFileName = $maskDir."/".$maskList[0].".nii.gz";

        copy($maskFileName, $iterationFileName) or die "Could not copy $maskFileName\n";

        my $nMasks = @maskList;
        for (my $i=1;$i < $nMasks; $i++) {
                my $maskFileName = "FSL_masks/".$maskList[$i];
#                print "*** $iterationFileName -add $maskFileName $iterationFileName \n";
```

```
                    `fslmaths $iterationFileName -add $maskFileName $iterationFileName`;

        }


            $iterationNo++;
}
```

Jackknife iteration masks and differing percentage overlap masks were made using bash scripts, the below example is a script used to make jackknife mask iterations:

```bash
#!/bin/bash

cd  /mnt/hgfs/VM_shared/GB/jackknife_iterations_new


for i in 1 2 3 4 5 6 7 8 9 10 11 12 13 14 15 16 17 18 19 20 21 22 23 24 25 26 27 28 29 30 31 32 33 34 35 36 37 38 39 40 41 42
43 44 45 46 47 48 49 50 51 52 53 54 55 56 57 58 59 60 61 62 63 64 65 66 67 68 69 70 71 72 73 74 75 76 77 78 79 80 81 82 83
84 85 86 87 88 89 90 91 92 93 94 95 96 97 98 99 100
do

        mkdir $i'_percent_mask'
        echo '*********************************************************************'
        echo '************************'$i' percent *****************************'
        echo '*********************************************************************'

    for j in 1 2 3 4 5 6 7 8 9 10 11 12 13 14 15 16 17 18 19 20 21 22 23 24 25 26 27 28 29 30 31 32 33 34 35 36 37 38 39 40
41 42 43 44 45 46 47 48 49 50 51 52 53 54 55 56 57 58 59 60 61 62 63 64 65 66 67 68 69 70 71 72 73 74 75 76 77 78 79 80 81
82 83 84 85 86 87 88 89 90 91 92 93 94 95 96 97 98 99 100
        do


            fslmaths '/mnt/hgfs/VM_shared/GB/percentage_masks/binary/'$i'_percent_mask.nii.gz' -sub
'/mnt/hgfs/VM_shared/GB/FSL_masks/'$j'.nii.gz'
'/mnt/hgfs/VM_shared/GB/jackknife_iterations_new/'$i'_percent_mask/'$i'_percent_jackknife_'$j'.nii.gz'
        fslmaths '/mnt/hgfs/VM_shared/GB/jackknife_iterations_new/'$i'_percent_mask/'$i'_percent_jackknife_'$j'.nii.gz' -
bin '/mnt/hgfs/VM_shared/GB/jackknife_iterations_new/'$i'_percent_mask/'$i'_percent_jackknife_'$j'_bin.nii.gz'
            fslstats
'/mnt/hgfs/VM_shared/GB/jackknife_iterations_new/'$i'_percent_mask/'$i'_percent_jackknife_'$j'_bin.nii.gz' -V | tee -a
'/mnt/hgfs/VM_shared/GB/jackknife_iterations_new/'$i'_percent_mask/jackknife_summary.txt'
    done
done
```

Finally, an excel spreadsheet is used to perform the actual BCa calculations. A new tab is created for each variation in overlap, and a result is shown that determines whether or not the mask is within the 95% BCa confidence limit and therefore considred "stable". The macro used to call in each iteration's data to the sheet is below:

```
Function bootstrap_percentile_calculator()

' open .txt file with all of the ACTUAL (from the initial data, not from a bootstrap interation)
' values for the voxels contained in each mask

Workbooks.OpenText Filename:="G:\bootstrap_new\percentage_masks\actual_percentage_mask_overlap_values.txt", _
Origin:=xlMSDOS, StartRow:=1, DataType:=xlDelimited, TextQualifier:= _
xlDoubleQuote, ConsecutiveDelimiter:=True, Tab:=True, Semicolon:=False, _
Comma:=False, Space:=False, Other:=False, FieldInfo:=Array(Array(1, 1), _
```

```
                Array(2, 1)), TrailingMinusNumbers:=True

        Dim i As Double
        For i = 5 To 10 Step 2.5
        ' NOTE: THIS USUALLY FAILS AT VERY LOW OR VERY HIGH PERCENTAGE VALUES, DUE TO THE ACTUAL
        NUMBER OF
        ' VOXELS IN THE PERCENTAGE OVERLAP MASK FALLING OUTSIDE OF THE BOOTSTRAP CONFIDENCE
        INTERVAL
        ' copy a tab for the new data to be pasted into
            Windows("BCA_method.xls").Activate
            Sheets("dummy_worksheet").Select
            Sheets("dummy_worksheet").Copy Before:=Sheets(1)
            Sheets("dummy_worksheet (2)").Select
            Sheets("dummy_worksheet (2)").Name = "" & i & "_percent_mask"
            Columns("C:C").Select
            Selection.ClearContents
            Columns("H:H").Select
            Selection.ClearContents

        ' open .txt file with the bootstrap mask data inside for this mask
            Workbooks.OpenText Filename:="G:\bootstrap_new\stats\" & i & "_percent_mask.txt", _
            Origin:=xlMSDOS, StartRow:=1, DataType:=xlDelimited, TextQualifier:= _
            xlDoubleQuote, ConsecutiveDelimiter:=True, Tab:=False, Semicolon:=False, _
            Comma:=False, Space:=True, Other:=False, FieldInfo:=Array(Array(1, 1), _
            Array(2, 1)), TrailingMinusNumbers:=True

        ' copy bootstrap iteration mask volume values from .txt file into calc worksheet

            Windows("" & i & "_percent_mask.txt").Activate
            Range("A1:A1000").Select
            Selection.Copy
            Windows("BCA_method.xls").Activate
            Sheets("" & i & "_percent_mask").Select
            Range("C3:C1002").Select
            ActiveSheet.Paste
            Range("H1:H1000").Select
            ActiveSheet.Paste
        ' sort the values in column H from lowest to highest (this is how it picks the .025 and .975 percentile points)
            Selection.Sort Key1:=Range("H1000"), Order1:=xlAscending, Header:=xlGuess _
            , OrderCustom:=1, MatchCase:=False, Orientation:=xlTopToBottom, _
            DataOption1:=xlSortNormal

            Windows("" & i & "_percent_mask.txt").Activate
            ActiveWindow.Close

        ' take actual number of voxels from the appropriate mask from the .txt file and paste into calc worksheet
            Windows("actual_percentage_mask_overlap_values.txt").Activate
            For Each c In Worksheets("actual_percentage_mask_overlap_").Range("A1:A101")
                If c.Value = i Then
                    c.Select
                    ActiveCell.Offset(0, 1).Select
                    Selection.Copy
                    Windows("BCA_method.xls").Activate
                    Sheets("" & i & "_percent_mask").Select
                    Range("C2").Select
                    ActiveSheet.Paste
                End If
            Next c

        ' open .txt file with the jackknife iteration data inside for this mask for calc of theta(.)
            Workbooks.OpenText Filename:="G:\bootstrap_new\jackknife_iterations\" & i & "_percent_mask.txt", _
            Origin:=xlMSDOS, StartRow:=1, DataType:=xlDelimited, TextQualifier:= _
            xlDoubleQuote, ConsecutiveDelimiter:=True, Tab:=False, Semicolon:=False, _
            Comma:=False, Space:=True, Other:=False, FieldInfo:=Array(Array(1, 1), _
            Array(2, 1)), TrailingMinusNumbers:=True

        ' copy jackknife iteration data into worksheet for calculation of theta(.)

            Windows("" & i & "_percent_mask.txt").Activate
            Range("A1:A40").Select
            Selection.Copy
            Windows("BCA_method.xls").Activate
            Sheets("" & i & "_percent_mask").Select
            Range("Q2:Q41").Select
            ActiveSheet.Paste
```

```vb
    Range("Q2:Q41").HorizontalAlignment = xlCenter
    Windows("" & i & "_percent_mask.txt").Activate
    ActiveWindow.Close

' copy values from the H column to the cells that show the percentile ends

    Windows("BCA_method.xls").Activate
    Sheets("" & i & "_percent_mask").Select
    Dim low As Integer
    Dim high As Integer
    low = Cells(34, "L").Value
    If low >= 1 And low <= 1000 Then
        Range("H" & low & "").Select
        Selection.Copy
        Range("L36").Select
        ActiveSheet.Paste
        Range("L36").HorizontalAlignment = xlCenter

        high = Cells(35, "L").Value
        Range("H" & high & "").Select
        Selection.Copy
        Range("L37").Select
        ActiveSheet.Paste
        Range("L37").HorizontalAlignment = xlCenter

    Else
    End If

    If low = 0 Then
        Range("H1").Select
        Selection.Copy
        Range("L36").Select
        ActiveSheet.Paste
        Range("L36").HorizontalAlignment = xlCenter

        high = Cells(35, "L").Value
        Range("H" & high & "").Select
        Selection.Copy
        Range("L37").Select
        ActiveSheet.Paste
        Range("L37").HorizontalAlignment = xlCenter

    Else
    End If

Next i

Windows("actual_percentage_mask_overlap_values.txt").Activate
ActiveWindow.Close
End Function
```

8.4   Appendix 4: Pons Normalisation Script

```
//  ImageJ Macro for extracting mean values for each slice in the pons rectangular prism in MNI space
// The pons runs from slice 7 to 12, the makePolygon function describes the area in each slice
// creates a text file with a 6 by 2 matrix
// that contains the following
// Slice number (Z coord) :  mean voxel number
// // Slice number (Z coord) :  mean voxel number etc for each of the 6 slices
// this can then be read into matlab to get the mean voxel number for the pons in an image
dir1 =getDirectory("Choose Source Directory for ROI_filled ");
list1 = getFileList(dir1);
for (i=0 ; i<list1.length; i++) {                          // this is to make sure that it only gets the folders that contain the images
files
        //open(dir1+list1[i]);
        //if (endsWith(list1[i],"_func_2_FSL_T1_MNI.nii.gz")) {
        open(dir1+list1[i]+'func_2_MNI.nii.gz');
        gb = getInfo("image.filename");
        gb1 = substring(list1[i],0,4);
        print(list1[i]+"_"+gb);
        // now set rectangles on the correct slices and do the maths to do the scaling
        setSlice(18);
        makeRectangle(40, 49, 11, 6);
        getStatistics(area, mean18, min, max, std, histogram);
        print("mean18" + " " + mean18);
        setSlice(19);
        makeRectangle(40, 49, 11, 6);
        getStatistics(area, mean19, min, max, std, histogram);
        print("mean19" + " " + mean19);
        setSlice(20);
        makeRectangle(40, 49, 11, 6);
        getStatistics(area, mean20, min, max, std, histogram);
        print("mean20" + " " + mean20);
        setSlice(21);
        makeRectangle(40, 49, 11, 6);
        getStatistics(area, mean21, min, max, std, histogram);
        print("mean21" + " " + mean21);
        setSlice(22);
        makeRectangle(40, 49, 11, 6);
        getStatistics(area, mean22, min, max, std, histogram);
        print("mean22" + " " + mean22);
        setSlice(23);
        makeRectangle(40, 49, 11, 6);
        getStatistics(area, mean23, min, max, std, histogram);
        print("mean23" + " " + mean23);
        meansum = mean18 + mean19 + mean20 + mean21 + mean22 + mean23;
        print(meansum);
        mean = meansum / 6;
        print("pons mean =  " + mean);
        calfactor = 10000/mean;
        print("calfactor =  " + calfactor);
        print("scaled pons mean =  " + calfactor*mean);
        print(" ");
        makeRectangle(0, 0, 91, 109);
        run("Multiply...", "value=calfactor stack");
        run("Flip Horizontally", "stack");                    //these two lines get it back in the correct orientation before resaving
        run("Rotate... ", "angle=180 grid=1 interpolation=Bicubic stack");
        run("Analyze 7.5...", "save="+dir1+list1[i]+"func_2_MNIscaled");
//      selectWindow(gb);
        close();
//      gb1 = substring(gb,0,4);
//      selectWindow("Log");
//      saveAs("Text", "D:\\Analyze\\32_bit\\pons\\"+gb1+".txt");
//      selectWindow("Log");
//      run("Close");

        //}else{
        //}
}
```

8.5 Appendix 5: Hippocampal Mask Volume Sampling

```
// ImageJ macro for sampling a masked region in a PET image, return a list of voxel number from within the volume in a text
file.
//PONS NORMALISATION
//
// Imports each warped PET, records the average counts within the pons (approximate area outlined) on the 2mm
// res T1 FSL template, then scales the image so that the average pons counts = 10 000. Saves the scaled image.
// Only works when the directory tree looks like this:
//                                        some dir/
//
//                      AD/                                      HC/
//
//            patient1/          patient2/ etc        patient1/          patient2/ etc
//
//         image_title.nii.gz    image_title.nii.gz    image_title.nii.gz              image_title .nii.gz
//
//AND when the images have been warped to the FSL T1 2mm res template. warping to another template will
//require different slices and areas to be used for the pons and a different rectangle to use to identify the whole slice for
//rescaling.
//EDIT: it also works for the SPM PET template as this is in very good alignment with the FSL T1 2mm MNI template and
//has the same voxel size.
// It also requires all the images of the same modality to have the same name

dir1 =getDirectory("Choose Source Directory for AD images");
list1 = getFileList(dir1);
dir2 =getDirectory("Choose Source Directory for HC images");
list2 = getFileList(dir2);
dir3 =getDirectory("Choose Source Directory for MCI images");
list3 = getFileList(dir3);

//image_title=File.openDialog("pick a warped PET image");
image_title_1="func_2_MNI";                        //image_title_1=substring(image_title,32,51);

for (i=0 ; i<list1.length; i++) {
            open(dir1+list1[i]+image_title_1+".nii.gz");
            setSlice(22);
            makePolygon(40,49,40,52,42,54,49,54,51,52,51,49);
            getStatistics(area, mean22, min, max, std, histogram);
            setSlice(21);
            makePolygon(40,49,40,52,42,54,49,54,51,52,51,49);
            getStatistics(area, mean21, min, max, std, histogram);
            setSlice(20);
            makePolygon(40,49,40,51,42,53,49,53,51,51,51,49);
            getStatistics(area, mean20, min, max, std, histogram);
            setSlice(19);
            makePolygon(40,49,43,52,48,52,51,49);
            getStatistics(area, mean19, min, max, std, histogram);
            setSlice(18);
            makePolygon(41,49,43,52,48,52,50,49);
            getStatistics(area, mean18, min, max, std, histogram);
            setSlice(17);
            makePolygon(41,49,43,51,47,51,49,49);
            getStatistics(area, mean17, min, max, std, histogram);
            meansum = mean22 + mean21 + mean20 + mean19 + mean18 + mean17 ;
            mean = meansum / 6;
            calfactor = 10000/mean;
            makeRectangle(0, 0, 91, 109);
//the next line gets it back in the correct orientation before resaving
            run("Multiply...", "value=calfactor stack");
            run("Flip Vertically", "stack");
            run("Analyze 7.5...", "save="+dir1+list1[i]+image_title_1+"_scaled");
            close();
}

for (i=0 ; i<list2.length; i++) {
            open(dir2+list2[i]+image_title_1+".nii.gz");
            setSlice(22);
            makePolygon(40,49,40,52,42,54,49,54,51,52,51,49);
            getStatistics(area, mean22, min, max, std, histogram);
            setSlice(21);
            makePolygon(40,49,40,52,42,54,49,54,51,52,51,49);
```

```
            getStatistics(area, mean21, min, max, std, histogram);
            setSlice(20);
            makePolygon(40,49,40,51,42,53,49,53,51,51,49);
            getStatistics(area, mean20, min, max, std, histogram);
            setSlice(19);
            makePolygon(40,49,43,52,48,52,51,49);
            getStatistics(area, mean19, min, max, std, histogram);
            setSlice(18);
            makePolygon(41,49,43,52,48,52,50,49);
            getStatistics(area, mean18, min, max, std, histogram);
            setSlice(17);
            makePolygon(41,49,43,51,47,51,49,49);
            getStatistics(area, mean17, min, max, std, histogram);
            meansum = mean22 + mean21 + mean20 + mean19 + mean18 + mean17 ;
            mean = meansum / 6;
            calfactor = 10000/mean;
            makeRectangle(0, 0, 91, 109);
            run("Multiply...", "value=calfactor stack");
//the next line gets the image back in the correct orientation for FSL before resaving
            run("Flip Vertically", "stack");
            run("Analyze 7.5...", "save="+dir2+list2[i]+image_title_1+"_scaled");
            close();
}

for (i=0 ; i<list3.length; i++) {
            open(dir3+list3[i]+image_title_1+".nii.gz");
            setSlice(22);
            makePolygon(40,49,40,52,42,54,49,54,51,52,51,49);
            getStatistics(area, mean22, min, max, std, histogram);
            setSlice(21);
            makePolygon(40,49,40,52,42,54,49,54,51,52,51,49);
            getStatistics(area, mean21, min, max, std, histogram);
            setSlice(20);
            makePolygon(40,49,40,51,42,53,49,53,51,51,51,49);
            getStatistics(area, mean20, min, max, std, histogram);
            setSlice(19);
            makePolygon(40,49,43,52,48,52,51,49);
            getStatistics(area, mean19, min, max, std, histogram);
            setSlice(18);
            makePolygon(41,49,43,52,48,52,50,49);
            getStatistics(area, mean18, min, max, std, histogram);
            setSlice(17);
            makePolygon(41,49,43,51,47,51,49,49);
            getStatistics(area, mean17, min, max, std, histogram);
            meansum = mean22 + mean21 + mean20 + mean19 + mean18 + mean17 ;
            mean = meansum / 6;
            calfactor = 10000/mean;
            makeRectangle(0, 0, 91, 109);
            run("Multiply...", "value=calfactor stack");
//the next line gets the image back in the correct orientation for FSL before resaving
            run("Flip Vertically", "stack");
            run("Analyze 7.5...", "save="+dir3+list3[i]+image_title_1+"_scaled");
            close();
}
//CONVERTING PONS SCALED IMAGES TO NIFTI
//
//FSL only works with nifti but ImageJ only wants to save as analyze...

// convert analyze files to nifti
for (i=0 ; i<list1.length; i++) {
            exec("mri_convert", dir1+list1[i]+image_title_1+"_scaled"+".img", dir1+list1[i]+image_title_1+"_scaled"+".nii.gz"
);
            }
for (i=0 ; i<list2.length; i++) {
            exec("mri_convert", dir2+list2[i]+image_title_1+"_scaled"+".img", dir2+list2[i]+image_title_1+"_scaled"+".nii.gz"
);
            }
for (i=0 ; i<list3.length; i++) {
            exec("mri_convert", dir3+list3[i]+image_title_1+"_scaled"+".img", dir3+list3[i]+image_title_1+"_scaled"+".nii.gz"
);
            }

// delete analyze files
for (i=0 ; i<list1.length; i++) {
            exec("rm", dir1+list1[i]+image_title_1+"_scaled"+".img", dir1+list1[i]+image_title_1+"_scaled"+".hdr" );
            }
```

```
for (i=0 ; i<list2.length; i++) {
        exec("rm", dir2+list2[i]+image_title_1+"_scaled"+".img", dir2+list2[i]+image_title_1+"_scaled"+".hdr" );
        }
for (i=0 ; i<list3.length; i++) {
        exec("rm", dir3+list3[i]+image_title_1+"_scaled"+".img", dir3+list3[i]+image_title_1+"_scaled"+".hdr" );
        }

//MASKING THE SCALED PET IMAGES

mask_title=File.openDialog("pick the mask image");
Dialog.create("Mask name input");
Dialog.addString("text to add to masked pet image to identify which mask was used:", "");
Dialog.show();
mask_suffix = Dialog.getString();
for (i=0 ; i<list1.length; i++) {
        exec("fslmaths", mask_title, "-mul", dir1+list1[i]+image_title_1+"_scaled"+".nii.gz",
dir1+list1[i]+image_title_1+"_scaled_"+mask_suffix+".nii.gz"  );
        }
for (i=0 ; i<list2.length; i++) {
        exec("fslmaths", mask_title, "-mul", dir2+list2[i]+image_title_1+"_scaled"+".nii.gz",
dir2+list2[i]+image_title_1+"_scaled_"+mask_suffix+".nii.gz" );
        }
for (i=0 ; i<list3.length; i++) {
        exec("fslmaths", mask_title, "-mul", dir3+list3[i]+image_title_1+"_scaled"+".nii.gz",
dir3+list3[i]+image_title_1+"_scaled_"+mask_suffix+".nii.gz" );
        }

selectWindow("Log");
run("Close");

//EXTRACT AND RECORD HIPPOCAMPAL VOXELS FROM  THE MASKED SCALED PET IMAGES

dir4 =getDirectory("Choose output directory for voxel count .txt files");
File.makeDirectory(dir4+"AD");
dir5=dir4+"AD/";
File.makeDirectory(dir4+"HC");
dir6=dir4+"HC/";
File.makeDirectory(dir4+"MCI");
dir7=dir4+"MCI/";
for (i=0; i<list1.length; i++) {
        open(dir1+list1[i]+image_title_1+"_scaled_"+mask_suffix+".nii.gz");
        gb = list1[i];
        w = getWidth();
        h = getHeight();
        s = nSlices();
        for (z=1; z<=s; z++){
                setSlice(z);
                for (x=0; x<=w; x++) {
                        for (y=0; y<h; y++) {
                                v = getPixel(x, y);
                                if (v > 0){
                                print("" +  v);
                                } else{
                                }
                }
                }
        }
        selectWindow("Log");
        gb1 = substring(gb,0,4);
        saveAs("Text", ""+dir5+gb1);
        run("Close");
        close();
}

for (i=0; i<list2.length; i++) {
        open(dir2+list2[i]+image_title_1+"_scaled_"+mask_suffix+".nii.gz");
        gb = list2[i];
        w = getWidth();
        h = getHeight();
        s = nSlices();
        for (z=1; z<=s; z++){
                setSlice(z);
                for (x=0; x<=w; x++) {
                        for (y=0; y<h; y++) {
                                v = getPixel(x, y);
                                if (v > 0){
```

```
                                                        print("" +  v);
                                                        } else{
                                                        }
                                }
                                }
                }
                selectWindow("Log");
                gb1 = substring(gb,0,4);
                saveAs("Text", ""+dir6+gb1);
                run("Close");
                close();
        }

        for (i=0; i<list3.length; i++) {
                open(dir3+list3[i]+image_title_1+"_scaled_"+mask_suffix+".nii.gz");
                gb = list3[i];
                w = getWidth();
                h = getHeight();
                s = nSlices();
                for (z=1; z<=s; z++){
                        setSlice(z);
                        for (x=0; x<=w; x++) {
                                for (y=0; y<h; y++) {
                                        v = getPixel(x, y);
                                        if (v > 0){
                                        print("" +  v);
                                        } else{
                                        }
                                }
                                }
                }
                selectWindow("Log");
                gb1 = substring(gb,0,4);
                saveAs("Text", ""+dir7+gb1);
                run("Close");
                close();
        }
```